Self-Similar Models of Quasar Outflow Shock Structures

Model Analysis with Comparison to Observations of FeLoBAL Quasar SDSS J030000.56+004828

Erik Weiss

A Thesis Submitted to the Faculty of Graduate Studies in Partial Fulfillment of the Requirements for the Degree of Master of Science

Graduate Program in Physics & Astronomy

York University, Toronto, Ontario

September 2023

Abstract

Supersonic winds of outflowing material are observed and/or predicted in a number of astrophysical systems; such winds may drive an expanding shock structure that shocks and pushes the ambient interstellar medium (ISM) outward. This thesis analyses, combines and expands on existing analytic self-similar models of these structures in the context of quasar accretion disk winds; we then search for the bulk acceleration (positive or negative) of low-velocity Ca II in the quasar SDSS J030000.0+004828.0 (J0300) and compare our results to model predictions. We find a strong upper limit on the acceleration magnitude, yielding plausible model constraints, but the observed range of gas velocities implies that the Ca II velocity profile does not coincide with that of the shocked ISM. We conclude with a discussion of recent results regarding J0300's outflow properties and briefly investigate the possibility of pre-existing ISM cloud disruption as an explanation for the observed Ca II velocity profile.

Contents

Abstract ii

Contents iii

List of Tables vi

List of Figures vii

1 Introduction 1

2 Blast Wave Model 4

2.0.1 General Theory and Model Parameters 4

2.0.2 Methods 9

2.1 Global Dynamics 13

2.1.1 Free Expansion ($t \ll t_f$) 13

2.1.2 Self-Similar Outflow Phases at Late Times ($t \gg t_f$) 15

2.1.3 Stability & Evolution of Outflows 28

2.1.4 Energy & Momentum Coupling 47

2.1.5 Remarks 50

2.2 Outflow Structure and Local/Regional Dynamics 51

2.2.1 Shocked Ambient Cooling & Shell Formation 51

2.2.2 Shock Features 55

2.2.3 Regional Gas Observables 59

2.3 Closing Remarks 77

3 Searching for Deceleration: Observations of J0300 78

3.1 Choice of Target 78

3.2 Previous High-Resolution Spectrum (UVES) . . . 79
3.3 New High-Resolution Spectrum (GRACES) . . . 79
3.4 Processing and Cross-Correlation . . . 80
3.4.1 Wavelength Calibration Check . . . 83
3.4.2 Cross-Correlation . . . 84
3.5 Closing Remarks . . . 85

4 Discussion **87**
4.1 Potentially Relevant Properties of J0300 and Other Ca II BAL Quasars . . . 88
4.2 Velocity Range of Shocked ISM Gas . . . 89
4.3 Comparison to Choi et al. . . . 92
4.3.1 Searching for Matching Parameter Choices . . . 93
4.3.2 Observed vs. Model Column Densities . . . 96
4.4 Acceleration of Preexisting ISM Clouds . . . 97
4.4.1 Comparison to the J0300 Acceleration Upper Limit . . . 102
4.4.2 Acceleration in the Shocked Ambient Medium Region . . . 106
4.5 Closing Remarks . . . 108

5 Conclusions **108**
5.1 Future Directions . . . 111

Bibliography **112**

A Appendix A: Data Visualisation and Analysis with D&R Mapping **117**
A.1 Notation . . . 117
A.2 D-maps . . . 119
A.3 R-maps . . . 119
A.4 Toy Example . . . 121

A.5 Summary and Remarks 125

List of Tables

2.1 Variable Parameters and Random Sampling Intervals 11
2.2 Filters on the Master Dataset $\mathcal{X}$ 12
3.1 J0300 Cross-Correlation Table 86
4.1 J0300 Comparison Model Outflow Parameters 103

List of Figures

2.1 Outflow Shock Structure Diagram . . . 6
2.2 D&R Mapping of $(\mathcal{X} : \theta_w, \varphi_f, \alpha)$ . . . 15
2.3 D&R Mapping of $(\mathcal{X}(\texttt{ADI \& } t < t_{f,B}) : t, R_{2,B}/R_{2,S}, \theta_w)$ . . . 28
2.4 Outflow Phase Transition Diagram: TTP Cooling . . . 35
2.5 Outflow Phase Transition Diagram: REF Cooling . . . 36
2.6 D&R Mapping of $(\mathcal{X} : \alpha, \mathcal{C}_{TTP}, L_{AGN})$ . . . 41
2.7 D&R Mapping of $(\mathcal{X} : \alpha, \mathcal{C}_{TTP}, v_w)$ . . . 42
2.8 D&R Mapping of $(\mathcal{X} : \alpha, \mathcal{C}_{TTP}, \tau_w)$ . . . 43
2.9 D&R Mapping of $(\mathcal{X}(\texttt{IR}) : t_{PI}, t_{IE}, \alpha)$ . . . 46
2.10 D&R Mapping of $(\mathcal{X}(\texttt{IR \& FAST}) : t_{PI}, t_{IE}, v_w)$ . . . 47
2.11 D&R Mapping of $(\mathcal{X}(\texttt{IA}) : \alpha, t_{sf}^{FF}, L_{AGN})$ . . . 55
2.12 Shock Feature Locations . . . 59
2.13 Gas Velocity Profiles . . . 63
2.14 Gas Deceleration Profiles . . . 66
2.15 Self-similar Gas Acceleration Profiles for $\alpha = 4/3$ . . . 68
2.16 Gas Density Profiles (Varying Time) . . . 70
2.17 Gas Density Profiles (Varying Density Gradients) . . . 71
2.18 Gas Column-Density-per-Unit-Velocity Profiles (Varying Time) . . . 75
2.19 Gas Column-Density-per-Unit-Velocity Profiles (Varying Density Gradients) 76
3.1 UVES & GRACES Spectra of J0300 . . . 81
3.2 Normalised UVES/GRACES Cross-Correlation Function . . . 87
4.1 Cornerplot of J0300 Candidate Outflow Characteristics . . . 95
A.1 Toy Example 1: D&R Mapping of $(\mathcal{X} : a, b^{c/b}c^{a/c}, a)$ . . . 123
A.2 Toy Example 2: D&R Mapping of $(\mathcal{X} : a, b^{c/b}c^{a/c}, b^{c/b}c^{a/c})$ . . . 124

A.3 Toy Example 3: D&R Mapping of $(\mathcal{X}(\texttt{a < 2b}) : a, b^{c/b}c^{a/c}, \ln(a^{abc}b^{3/a}c^{a/3}))$. 125

1 Introduction

Lying at the centre of some galaxies are active galactic nuclei (AGN): supermassive black holes which are actively accreting matter from their host galaxy, with the inflowing matter forming a hot accretion disk around the black hole. AGN accretion disks are thought to give off a supersonic wind of outflowing material (e.g., Murray et al. 1995, Proga et al. 2000), which can shock and sweep up the ambient interstellar medium (ISM) into a large-scale outflow (e.g., Arav et al. 2018, Hopkins et al. 2016, King & Pounds 2015, Zubovas & King 2012). The expulsion of star-forming ambient ISM by wind-driven shocks is one potential mechanism of AGN feedback, the process (or collection of processes) by which star formation in the host galaxy is suppressed (Di Matteo et al. 2005, King et al. 2011, Vayner et al. 2021). The idea of disk winds as an AGN feedback feedback mechanism gained momentum by virtue of Silk & Rees (1998) being able to show that an outflow driven by the energy of a quasar disk wind could expel infalling gas from its host galaxy if the central black hole mass M_{bh} and gas velocity dispersion σ follow a $M_{bh} \propto \sigma^5$ relationship, remarkably close to the observed (and now famous) $M_{bh} - \sigma$ relation (where $M_{bh} \propto \sigma^{\sim 4-5}$, e.g. Ferrarese & Merritt 2000, Gebhardt et al. 2000). Later, King (2003) also showed that in contrast to the energy-driven outflow of Silk & Rees (1998), an outflow driven by the wind's momentum yielded a relationship $M_{bh} \propto \sigma^4$ with a normalisation constant that agreed well with observations.

The large amount of energy injected into the ambient environment by a central source motivates the use of the classical self-similar blast wave (Sedov 1946, Taylor 1950a) to model shock structures driven by AGN winds, noting earlier applications to phenomena such as supernovae (e.g., Kahn 1976), stellar winds (e.g., Weaver et al. 1977, Koo & McKee 1992, hereafter W77 and KM92) and quasars (extreme AGN with immensely luminous accretion disks, visible over very large distances; Ikeuchi 1981). Self-similar models are

attractive because they provide qualitative, scale-independent information about the behaviour of a system far from major transition boundaries (Barenblatt & Zel'dovich 1972, Ferreira et al. 2015), for example a transition from a phase of inefficient cooling to one of efficient cooling. Building on the spherically symmetric models of W77 and KM92 (the latter of which generalised the uniform density and constant energy injection of the former to power laws), Faucher-Giguère & Quataert (2012, hereafter FGQ12) described the global dynamics of an AGN wind blast wave with an inefficient two-temperature plasma (TTP) cooling mechanism, allowing for a "boost" of the outflow's momentum flux relative to the wind. In this work we build on the methods of W77 and KM92 and expand the KM92 model to accommodate various cooling mechanisms (including FGQ12's TTP cooling) and provide full, analytically approximate profiles for gas observables, namely velocity, acceleration, density and column density. We also briefly consider an idealised self-similar high-latitude wind (a "biconical" wind; we drop the quotations moving forward and use the term biconical for simplicity), motivated by the work of Zeilig-Hess et al. (2019) and Zeilig-Hess et al. (2020), hereafter ZH+19 and ZH+20. While quasar winds/outflows are generally not spherically symmetric, the assumption still provides a simple and useful analytic framework to serve as a starting point. We analyse and compare these models in the context of quasars, showing distributions and trends pertaining to scale comparisons (in the case of both models) and phase transitions (for the expanded KM92 model) for an assumed uniform (or log-uniform) distribution of model parameters.

Observationally, the spectroscopic features of certain broad absorption line (BAL) quasars (Weymann et al. 1991, Allen et al. 2011, Hamann et al. 2019) are at least qualitatively consistent with the structure of a blast wave model, which includes a negative velocity gradient (lower velocities found at higher radii) and a high-density contact discontinuity, as shown in Figure 2.1 in the following section. In *LoBAL* quasars (quasars where low-ionisation absorbing gas is seen, for example Mg II), the high-ionisation absorb-

ing gas (e.g. C IV) generally extends to higher velocities than low-ionisation absorbing gas; in the iron LoBAL (*FeLoBAL*) quasar SDSS J030000.56+004828.0 (Hall et al. 2003), hereafter J0300, the UV continuum source is fully covered by an outflow containing many ions and extending to at least v=10850 km s^{-1}. Among these ions is strongly absorbing Ca II, which is found at the lowest outflow velocities and shows a peculiar velocity segregation, whereby at outflow speeds $\gtrsim$ 4000 km s^{-1} the strong Ca II absorption terminates but strong Mg II and Fe II absorption is present. Due to its low ionisation potential, the strongly-absorbing Ca II must be shielded by an ionisation front, which is naturally explained by the blast wave's contact discontinuity. Thus, at least in J0300 and a handful of other FeLoBAL quasars with strong low-velocity Ca II absorption (Choi et al., 2022), the strongly-absorbing Ca II is likely located farther from the quasar, segregated from the higher-velocity, high-ionisation absorbing gas (which is located closer to the quasar) by an ionisation front; if not, the higher-velocity gas would also be shielded and show only low-ionisation absorption. In addition, for BAL quasars with more than one absorption system, the spectral fits of Choi et al. (2022) yield a statistical trend for lower-velocity absorbers to be located at larger distances from the quasar (see their Figure 12).

The above conclusions raise a question: how can faster-moving outflowing gas close to the quasar co-exist with slower-moving outflowing gas farther from the quasar? It may be that the lower-velocity absorbing gas is part of a wind launched farther from the quasar than the higher-velocity gas is, with nonzero transverse velocity ensuring that the gas streamlines do not intersect (Arav et al., 1999; Hall et al., 2003; Giustini & Proga, 2019). However, it is also worth investigating whether the lower-velocity absorbing gas could arise from swept-up ISM gas (or from cooling shocked wind gas) in a blast wave, given the negative velocity gradient and contact discontinuity implied by the blast wave model. It is possible that the absorbing gas decelerates over time as more ISM is swept up by the outflow, and thus comparing observed deceleration measurements or limits to

model predictions could in principle constrain quasar and ISM parameters as well as the age of the outflow.

In this work we make such predictions and compare them to observations of J0300 taken almost a decade apart in the rest frame. Section 2 is dedicated to establishing and analysing the model, describing the structure and evolution of the blast wave along with the gas properties within its various regions; Section 3 then describes the processing of our old and new J0300 spectra and the results of our deceleration measurements. In Section 4 we compare our observational results to the literature and discuss them in the context of possible explanations for the origin of the Ca II-absorbing gas in J0300, before summarising our conclusions in Section 5.

2 Blast Wave Model

As mentioned in Section 1, this work primarily considers self-similar spherical blast wave models previously considered by W77, KM92, and FGQ12, but also briefly considers the biconical wind model of ZH+19 and ZH+20 for comparison. The biconical model (which was mainly meant to provide a theoretical comparison to hydrodynamic simulations) is more coarse and global in nature compared to the spherical model, in the sense that the outflow only exists in a single phase and the entire shock structure is considered as one unit (the "wind head"). The physical scales of the two outflow models are compared throughout Sections 2.1.1 and 2.1.2, after which the paper solely focuses on spherical outflows.

2.0.1 General Theory and Model Parameters

The basic premise of these models is that a central AGN "turns on" at time $t = 0$, launching a high-speed wind from the accretion disk into the ambient gas environment. There the wind is highly supersonic, driving an outward-moving shock structure. As the

wind expands outward and sweeps up more and more ambient gas, the shock structure progressively decelerates. In this regard the outflow can be classified into two major regimes: *early times* (also called *free expansion*), where the wind is effectively unimpeded and deceleration is negligible (the wind and shock velocities are roughly the same); and *late times*, where the deceleration is significant. An approximate spatial and temporal boundary R_f and t_f separating these regimes can be obtained, and are respectively called the free expansion radius/time. Thus for a self-similar model, early times correspond to times $t \ll t_f$, while late times correspond to times $t \gg t_f$.

The general shock structure at late times, shown in Figure 2.1, consists of a forward shock at radius R_2 that sweeps up and shocks the intervening ambient gas, and a reverse shock at R_1 which shocks the incoming wind. The resulting shocked wind (SW) and shocked ambient (SA) regions are separated by a contact discontinuity at radius R_c. For spherical winds (see above comments on biconical winds), the global outflow dynamics are related to the cooling of the shocked wind, and are discussed in Section 2.1. Local gas dynamics and the cooling of the shocked ambient region are discussed in Section 2.2.

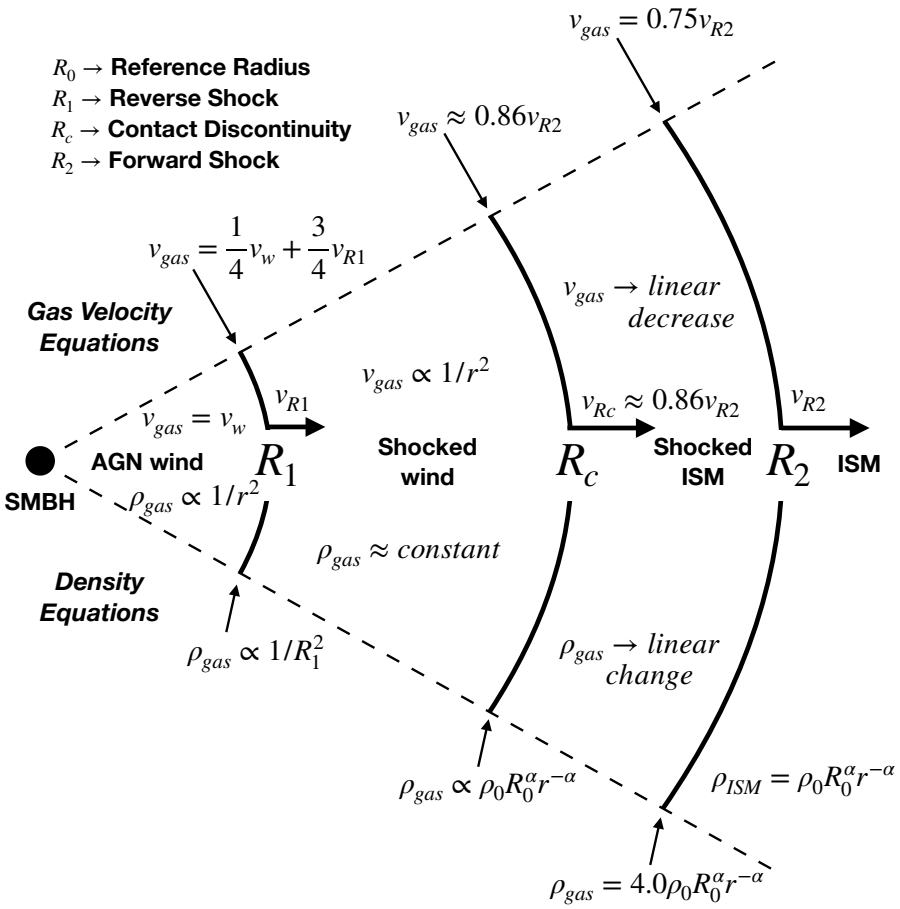

Figure 2.1: Diagram of the outflow shock structure at late times, including the different regions of shocked gas and their corresponding gas velocity and density profiles. The wind from the quasar starts with initial velocity v_w and the outer shock front sweeps into the ISM (which has density $\rho_0 R_0^\alpha r^{-\alpha}$) at a velocity of $v_{R2}(t)$.

The work herein uses spherical coordinates, assumes strong shocks at R_1 and R_2 (Mach numbers $\gg 1$) and assumes all gas is ideal (adiabatic index $\gamma = 5/3$), except in the case of *thin shell approximations*, where the shocked wind and/or shocked ambient regions lack thermal pressure support and the gas is treated as being compressed to a negligibly-thin region. In this limit the gas is incompressible with $\gamma = 1$, and so we use $\gamma_{sw} = 1$ and $\gamma_{sa} = 1$ to refer to situations in which these approximations apply, where $R_1 \rightarrow R_c$ and $R_c \rightarrow R_2$ respectively. We assume a mean mass of 1.4 atomic units per hydrogen nucleus

(cosmic abundance), i.e.

$$\mu \equiv \frac{\rho}{m_p n} = 1.4, \tag{2.1}$$

where ρ and n indicate the mass and hydrogen number density of the gas in question (and m_p is the proton mass). *All number densities will refer to the hydrogen number density hereafter.* A total of eight variable parameters are used: seven core model parameters and one secondary parameter. The core parameters consist of standalone parameters (time t and AGN luminosity L_{AGN}), wind parameters (velocity v_w and dimensionless momentum flux ratio τ_w) and ambient ISM parameters (gradient parameter/power law exponent α, reference radius R_0 and reference number density n_0). The secondary parameter is related to biconical winds (wind half-opening angle θ_w). A summary of the parameters and their ranges considered herein can be found in Table 2.1.

For the wind, the wind velocity v_w and mass outflow rate $\dot{M}_w$ are assumed to be constant. The more general case of $\dot{M}_w \propto t^{\eta_{in}-1}$ explored in KM92 is not treated here (i.e. this paper uses $\eta_{in} = 1$) because cooling, which plays a major role in the model, depends on $\dot{M}_w$. We are interested in the two-temperature cooling mechanism explored in FGQ12, which assumes $\eta_{in} = 1$ and is not trivially extended to $\eta_{in} \neq 1$. The constant wind velocity gives a natural expression for the free expansion time,

$$t_f \equiv \frac{R_f}{v_w}, \tag{2.2}$$

and then we follow FGQ12 by absorbing $\dot{M}_w$ into the momentum flux ratio

$$\tau_w \equiv \frac{\dot{P}_w}{\dot{P}_{rad}} = \frac{\dot{M}_w v_w}{L_{AGN}/c}, \tag{2.3}$$

where $\dot{P}_w \equiv \dot{M}_w v_w$ is the wind momentum flux and $\dot{P}_{rad} \equiv L_{AGN}/c$ is the radiative momentum flux. Since τ_w is a direct measure of the mass outflow rate (given L_{AGN} and v_w), it can also be thought of as an optical depth parameter, representing the amount of

mass "piling up" in the wind.

For the ambient ISM, we follow KM92 and assume a power law density profile

$$\rho_a(r) = \rho_0 \left(\frac{r}{R_0} \right)^{-\alpha}, \tag{2.4}$$

where $\rho_0 \equiv \rho_a(R_0)$. This generalises the singular isothermal sphere profile (e.g., Larson 1969, Shu 1977) where $\rho_a \propto r^{-2}$, while still allowing for simple outflow solutions. In the interest of not overcomplicating the model, we do not consider other commonly proposed profiles such as the Navarro-Frenk-White profile (Navarro et al. 1996). The exponent α represents the ambient density gradient, and turns out to be of primary importance (along with the mass outflow exponent η_{in}) in determining the outflow behaviour at late times (Section 2.1.2); we restrict ourselves to $\alpha \in (0, 1.5)$ (Section 2.0.2), and use the phrases *steep/shallow (ambient) density gradient* to refer to high/low magnitudes of α.

Because the mass density and number density are assumed to be in constant ratio (Equation (2.1)), we can write the density profile in terms of the number density:

$$n_a(r) = n_0 (r/R_0)^{-\alpha} \tag{2.5}$$

and the reference mass density in terms of the reference number density:

$$\rho_0 = \mu m_p n_0 = 1.4 m_p n_0. \tag{2.6}$$

Note that Equation (2.5) can also be written as $n_a(r) r^\alpha = n_0 R_0^\alpha$; in all equations/aspects of the model, n_0 and R_0 always appear together in the form on the right hand side, which we hereafter refer to $n_0 R_0^\alpha$ as the *ambient GCD* (GCD for "generalised column density"). Because of this the ambient GCD can essentially be thought of as a single model parameter, corresponding to various potential reasonable combinations of n_0 and

R_0 given α. In this paper, we consider R_0 from 1-1000 parsecs, much larger in magnitude than the 1-1000 cm^{-3}; in cgs units, the logarithm of the ambient GCD is tightly distributed about a linear function of α:

$$\log\left[\frac{n_0 R_0^\alpha}{1}\ \text{cm}^{-(3-\alpha)}\right] \approx 20\alpha + 1.5 \pm 1.5(1+\alpha), \tag{2.7}$$

where the $\pm 1.5(1+\alpha)$ term reflects the potential variations of n_0 and R_0. By virtue of this variation term being small in comparison to the 20α term, this approximation implies that the ambient GCD and density gradient α are effectively interchangeable for the purpose of qualitative order-of-magnitude analysis.

2.0.2 Methods

The primary tool for model analysis in this work, introduced herein, is dubbed *D&R mapping* and involves plotting two kinds of heatmaps – *D-maps* (D for density) and *R-maps* (R for representation) – to see various trends in a dataset. D&R mapping is described in detail in Appendix A, but in brief, we take a master dataset $\mathcal{X}$ (or a pre-filtered subset $\mathcal{X}_0 \subseteq \mathcal{X}$, if we wish) and plot its normalised distribution as a D-map, a heatmap in a 2D slice of feature space (i.e. a 2D histogram with respect to two features of interest, the *main features*). We then partition $\mathcal{X}_0$ by binning it into "bands" $\mathcal{X}_b \subseteq \mathcal{X}_0$ with respect to some other feature of interest, the *band feature*; each band yields a heatmap (an R-map) that shows how the band is represented in the D-map. The trends in the D-map of $\mathcal{X}_0$ with respect to the band feature are then seen in the collection of associated R-maps; given a filtered dataset $\mathcal{X}_0$, a collection of D&R maps given x-axis and y-axis histogram features (θ_x, θ_y) and band feature θ_z is notationally referred to as a D&R mapping of $(\mathcal{X}_0 : \theta_x, \theta_y, \theta_z)$. A toy example of D&R mapping (with figures) can be found in Appendix A.4.

Since we need a dataset for this method, we simulate a master dataset via random

sampling of the model parameter space; for α and θ_w we draw from a uniform distribution, while for the remaining parameters (which span multiple orders of magnitude), we draw from a log-uniform distribution. We adopt the notation above, using $\mathcal{X}, \mathcal{X}_0$ and $\mathcal{X}_b$ for the master dataset and pre-filtered/band-filtered subsets, and additionally use the function $|\cdot|$ on a dataset to denote the number of samples/data points; for this work, we use $|\mathcal{X}| = 10^7$. Table 2.1 gives the list of model parameters (with brief descriptions and sampling ranges), while Table 2.2 gives a list of filters for $\mathcal{X}$ used herein (with brief descriptions and technical conditions). The corresponding filtered subsets are denoted by $\mathcal{X}_0 = \mathcal{X}(\texttt{FILTER.NAME})$; for example, one can define a trivial filter `TRUE` by the condition $1 = 1$, which yields the filtered dataset $\mathcal{X}_0 = \mathcal{X}(\texttt{TRUE}) = \mathcal{X}$. We emphasise for the reader that a number of D&R mappings in this work use $\mathcal{X}_0 = \mathcal{X}$; those which do not will always refer to $\mathcal{X}_0$ as $\mathcal{X}(\texttt{FILTER.NAME})$ as described above.

With regards to Table 2.1, we draw attention to the fact that the sampling interval for the ambient density gradient α is $(0, 1.5)$. The stability considerations in Section 2.1.3 suggest an upper limit $\alpha < 2$, but for simplicity we restrict ourselves to $\alpha < 1.5$, where all of the shocked ambient gas is decelerating but errors in the acceleration profile due to analytic approximation are small (see Section 2.2.3.2). This range also covers the range of values $\alpha \in (0.5, 1.5)$ for parsec-scale gas profiles around AGN found in Yao & Gan (2020), who note that values of $\alpha \simeq 1$ have been inferred from observations of several nearby AGN.

Variable Parameters and Ranges Considered/Random Sampling Intervals

Parameter	**Description**	**Sampling Interval**	**Reference(s)**
$\log(t/1\ \mathrm{yr})$	time	$(3, 5)$	–
$\log(L_{AGN}/1\ \mathrm{erg\ s^{-1}})$	AGN bolometric luminosity	$(45, 48)$	–
$\log(v_w/1\ \mathrm{km\,s^{-1}})$	wind velocity	$(3, 5)$	–
$\log \tau_w$	wind momentum flux parameter	$(-2, 0)$	Eq. (2.3)
α	ambient density gradient (power law exponent)	$(0, 1.5)$	Eqs. (2.4), (2.5)
$\log(R_0/1\ \mathrm{pc})$	ambient density reference radius	$(0, 3)$	Eqs. (2.4), (2.5)
$\log(n_0/1\ \mathrm{cm^{-3}})$	ambient hydrogen number density at R_0	$(0, 3)$	Eq. (2.5)
θ_w	biconical wind half-opening angle	$(1^\circ, 89^\circ)$	–

Table 2.1: Variable parameters used in this work, including descriptions and ranges considered in this work/sampling intervals for the simulated master dataset $\mathcal{X}$. The random sampling assumes a uniform distribution for α and θ_w, and a log-uniform distribution for the remaining parameters (indicated by the log in the first column).

Filters on the Master Dataset $\mathcal{X}$

Filter Name	Description	Condition(s)	Reference(s)
`IR`	outflow is initially radiative	$\mathcal{C} < 1$ $t_f < t_{PI} < t_{IE}$	Eq. (2.41) Section 2.1.3.5
`IA`	outflow is initially adiabatic	$\mathcal{C} > 1$ $t_{EI} < t_f$	Eq. (2.41) Section 2.1.3.5
`LATE`	outflow is past free expansion stage	$t > t_f$	Eq. (2.2)

`UNS`	outflow is unstable at time t	`IR`
		`LATE`
		$t > t_{PI}$
		$\alpha > 1$
			Section 2.1.3.2
			Eq. (2.45)

`RAD`	outflow in radiative phase at time t	`IR`
		`LATE`
		$t < t_{PI}$
			Eq. (2.45)

`INT`	outflow in intermediate phase at time t	`IR`
		`LATE`
		$\neg$`UNS`
		$t_{PI} < t < t_{IE}$
			Eqs. (2.45), (2.46)

`ADI`	outflow in adiabatic phase at time t	`IR` `LATE` $\neg$`UNS` $t > t_{IE}$ or `IA` `LATE`	Eq. (2.46)
`PASS`	outflow is late-time, stable and passes consistency checks	`RAD` or `INT` or `ADI` $R_1 < R_c$	Eqs. (2.45) - (2.47); End of Section 2.1.3.5 Section 2.2.2.2
`FAST`	faster winds only	$v_w > 10^4$ km s^{-1}	–
`J0300`	outflow properties close to J0300 observations	$-a_{post} < 0.1$ km s^{-1} yr^{-1} $d_{obs} < \log 2$	Eqs. (2.87), (4.2)

Table 2.2: Filters used on the simulated master dataset $\mathcal{X}$ to generate D&R maps (aside from the `PASS` filter, which is used in the generation of $\mathcal{X}$). All filters, where applicable, assume for their conditions the two-temperature plasma (TTP) cooling law of FGQ12, given in Equation (2.28). Note that the `ADI` filter conditions do not include a lower limit $\alpha > -1/7$ for initially adiabatic outflows (in accordance with Figure 2.4), due to the sampling interval of $\alpha \in (0, 1.5)$ in Table 2.1. Transition time-related consistency checks (Section 2.1.3.5) are built into the `IR` and `IA` filters, which, along with late-time and stability, are built into the `RAD`, `INT` and `ADI` filters. The final consistency check $R_1 < R_c$ (Section 2.2.2.2) is then implemented into the `PASS` filter.

2.1 Global Dynamics

2.1.1 Free Expansion ($t \ll t_f$)

For the spherical (subscript S) and biconical (subscript B) wind models we respectively follow the methods of KM92 (their Section 2.1) and ZH+19 (their Appendix A) to determine the free expansion radius R_f. In both references, R_f is roughly the location at which the shock structure has decelerated to half the wind speed, and both show that the wind density and ambient density are comparable there ($\rho_w(R_f) \sim \rho_a(R_f)$). However, KM92 uses conservation of momentum for the entire mass of the shock structure while ZH+19 uses local pressure balance in the frame of the shock (which they refer to as momentum balance). These methods respectively give R_f as the solutions to the equations

$$\rho_{w,S}(R_{f,S}) = \bar{\rho}_a(R_{f,S}) \quad \text{and} \quad \rho_{w,B}(R_{f,B}) = \rho_a(R_{f,B}) \tag{2.8}$$

(see KM92 and ZH+20 respectively), where

$$\bar{\rho}_a(r) \equiv \frac{4\pi \int_0^r \rho_a(r') r'^2 dr'}{(4\pi/3) r^3} = \frac{3}{3-\alpha} \rho_a(r) \tag{2.9}$$

is the mean ambient density within r. The wind density is defined by $\rho_w(r) = \dot{M}_w / \dot{V}_w(r)$, where $\dot{V}_w(r)$ is the time derivative of the wind volume at radius r, equal to $4\pi r^2 v_w$ for spherical winds and $4\pi(1 - \cos\theta_w) r^2 v_w$ for biconical winds (accounting for two cones). This gives wind densities

$$\rho_{w,S}(r) = \frac{\dot{M}_w}{4\pi r^2 v_w} \quad \text{and} \quad \rho_{w,B}(r) = \frac{1}{(1-\cos\theta_w)} \rho_{w,S}(r); \tag{2.10}$$

substituting $\dot{M}_w$ and ρ_0 from Equations (2.3) and (2.6) gives the following solutions to Equation (2.8):

$$R_{f,S} = \left[\frac{(3-\alpha)\tau_w L_{AGN}}{12\pi\mu m_p n_0 R_0^\alpha c v_w^2}\right]^{\frac{1}{2-\alpha}} \quad \text{and} \quad R_{f,B} = \left[\frac{\tau_w L_{AGN}}{4\pi\mu m_p n_0 R_0^\alpha c v_w^2 (1-\cos\theta_w)}\right]^{\frac{1}{2-\alpha}}. \tag{2.11}$$

To compare the physical scale of the free expansion period between the two models, we denote the *free expansion ratio*

$$\varphi_f \equiv \frac{R_{f,B}}{R_{f,S}} = \frac{t_{f,B}}{t_{f,S}} = \left[\frac{3}{(3-\alpha)}\frac{1}{(1-\cos\theta_w)}\right]^{\frac{1}{2-\alpha}} \tag{2.12}$$

and show the relationship between φ_f, θ_w and α in Figure 2.2 by D&R mapping. Given the asymptotic nature of $R_{f,B}$ in the limit $\theta_w \to 0$, results regarding biconical outflows where θ_w is low should be taken with caution when using the ZH+19 model. Furthermore, wind collimation may also affect results about the size and velocity of the outflow: ZH+19 note that strong collimation is seen in their 2D simulations for "essentially all of the cases explored" (half-opening angles $\theta_w = 30°$, $45°$ and $60°$ with $\alpha = 0$ or 2).

Lastly, note that for $\alpha = 2$, the denominators in the exponents of Equations (2.11) and (2.12) approach zero. Here the assumption of a free expansion period breaks down because the dimensional quantities which characterise the wind and ambient gas (e.g. L_{AGN}, v_w and $\rho_0 R_0^\alpha$ – the last of which is the essential constant of Equation (2.4)) can no longer form units of length or time. This special case corresponds to a permanent constant-velocity outflow, similar but not identical to free expansion, where the forward shock $R_2 = K v_w t$ and $K \in (0, 1)$ is a function of the model parameters (as opposed to $K = 1$ during free expansion in the case of $\alpha \neq 2$). These outflows are not considered here, but the interested reader may refer to KM92 (their Appendix A) for their treatment.

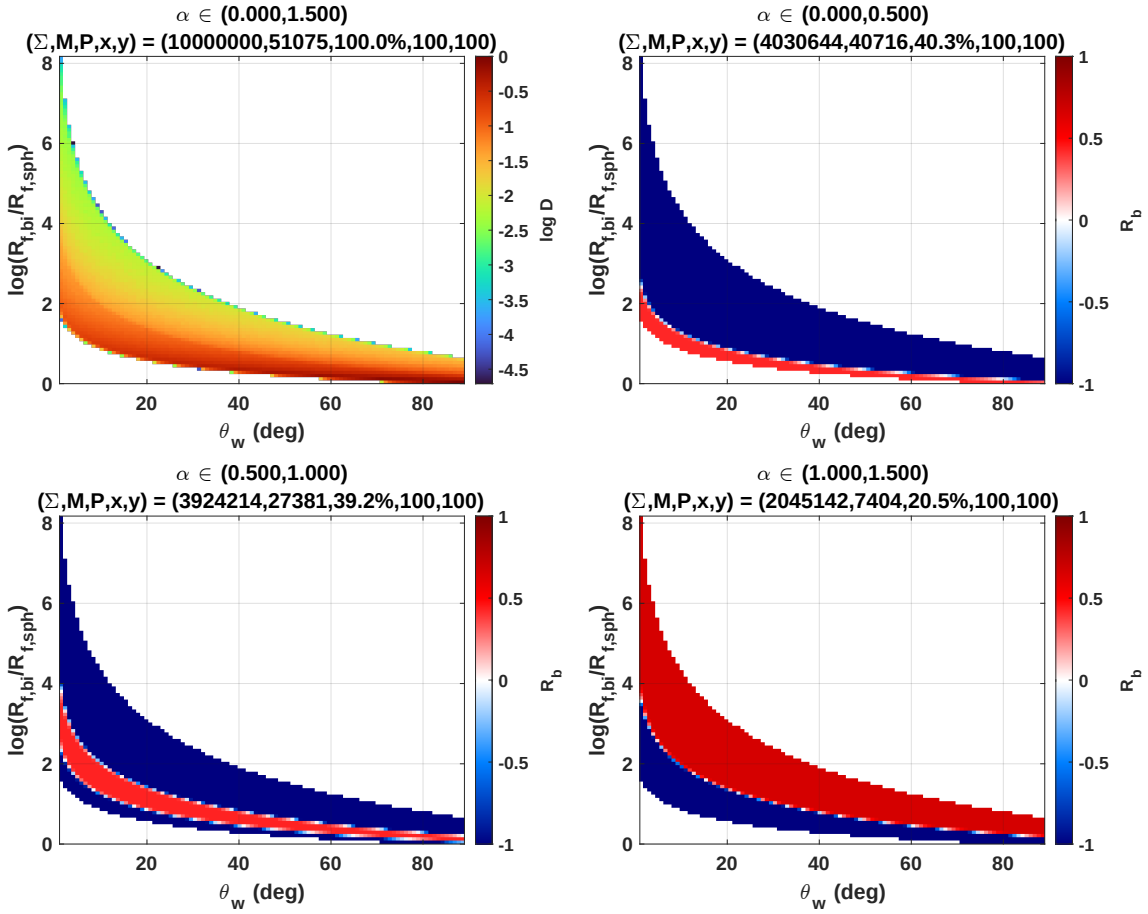

Figure 2.2: D&R Mapping of $(\mathcal{X} : \theta_w, \varphi_f, \alpha)$ showing the trends in Equation (2.12). The data comes from uniform random sampling on $\alpha \in (0, 1.5)$ and $\theta_w \in (1°, 89°)$, as noted in Table 2.1; we see that the free expansion ratio increases and takes on a wider range of values with increasing α. See Appendix A for an explanation of D&R mapping (including Section A.1 for explanation of the numbers found in the subplot titles).

2.1.2 Self-Similar Outflow Phases at Late Times ($t \gg t_f$)

To analyse the global outflow dynamics at late times, we look for a self-similar solution of the form

$$R_2 = At^{\beta}, \tag{2.13}$$

where the self-similarity parameters A and β are determined by the relevant physical circumstances of the outflow, which we will refer to as the (global) outflow phase. This

self-similarity is presumed to emerge at times $t \gg t_f$, in the limit where the velocities of the shock features are much less than the wind velocity. The general aspects of the outflow phase are captured by β, whose expression reflects how time factors into the physical laws; nuances of the outflow phase are captured in A, whose expression reflects any approximations used when implementing the physics (for example, the thin shell approximation). *For the sake of readability, in the expressions for A we omit phase or cooling subscripts or superscripts from β and the biconical or spherical subscripts from R_f and t_f; the reader should infer the appropriate subscripts or superscripts from context.*

Here we summarise the self-similar phases of the spherical and biconical models according to the methods of KM92 and ZH+20 respectively and give the corresponding self-similarity parameters. In particular, for the spherical case we condense KM92's method of determining the self-similarity parameters in the intermediate case where the cooling of the shocked wind (which governs the outflow phase) is neither negligible nor effectively instantaneous, so that the method can be easily applied to different cooling mechanisms; we then apply the method to the two-temperature plasma cooling mechanism explored in FGQ12.

Before proceeding, it will be useful to define the forward shock velocity

$$v_{R2} \equiv \frac{dR_2}{dt} = \beta A t^{\beta-1} \tag{2.14}$$

(along with analogous velocities v_{Rc} and v_{R1}) and the ratio

$$\begin{aligned}
\lambda_c &\equiv \frac{R_c}{R_2} \\
&\approx \frac{\gamma_{sa}^3 + 12\gamma_{sa}^2 + 8\gamma_{sa} + 1 - (1/2)(\gamma_{sa}+1)(3\gamma_{sa}+1)\alpha - (\gamma_{sa}+1)(4\gamma_{sa}+1)/\beta}{2\gamma_{sa}^3 + 12\gamma_{sa}^2 + 7\gamma_{sa} + 1 - (1/2)(\gamma_{sa}+1)(3\gamma_{sa}+1)\alpha - (\gamma_{sa}+1)(4\gamma_{sa}+1)/\beta} \\
&= \frac{1386 - 216\alpha - 552/\beta}{1466 - 216\alpha - 552/\beta} \quad (\text{for } \gamma_{sa} = 5/3) \\
&= 1 \quad (\text{for } \gamma_{sa} = 1).
\end{aligned} \tag{2.15}$$

The approximate value on the second line of Equation (2.15) is derived in KM92 (see their Appendix B1); assuming an energy-conserving outflow (Section 2.1.2.2) with an adiabatic shocked ambient region (Section 2.2.1), they showed that the hydrodynamic equations

$$\begin{aligned}
\frac{D\rho}{Dt} + \rho\left(\frac{\partial v}{\partial r} + \frac{2v}{r}\right) &= 0 \quad (\text{conservation of mass}) \\
\frac{Dv}{Dt} + \frac{1}{\rho}\frac{\partial p}{\partial r} &= 0 \quad (\text{conservation of momentum}) \\
\frac{D(p\rho^\gamma)}{Dt} &= 0 \quad (\text{conservation of energy})
\end{aligned} \tag{2.16}$$

yield a nearly linear self-similar velocity profile, where $D/Dt \equiv \partial/\partial t + v\partial/\partial r$ and ρ, v, p and γ are respectively the gas density, velocity, pressure and adiabatic index. Assuming a constant velocity gradient (the average of the analytic gradients at R_2 and R_c), the condition $v_{Rc} = \lambda_c v_{R2}$ yields the analytic expression in Equation (2.15), which is accurate to within $\lesssim 0.5\%$ of the numerically-determined λ_c values for the cases explored in KM92. We note in passing that for $\gamma_{sa} = 5/3$ we find similar accuracy for the radiative and intermediate outflows phases discussed below; however, *we assume* $\gamma_{sa} = 1$ *and therefore* $\lambda_c = 1$ *for these phases.* While it is possible in some cases that $\gamma_{sa} \neq 1$ during these phases, we assume $\gamma_{sa} = 1$ to avoid potential complications (see Section 2.2.1).

For spherical winds, KM92 defined the late-time phases (and determined their self-similarity parameters) according to how the shocked wind cools, and thus our primary quantity of interest is the shocked wind cooling time $t_{c,sw}$ (the timescale over which newly shocked wind radiates away its energy), which changes over time for the cases considered. At time t the space within the region $r \in (R_1, R_c)$ is assumed to be filled with *hot* shocked wind, i.e., the "fresh" shocked gas launched in the time range $[t - t_{c,sw}, t - t_{cr}]$, where

$$t_{cr} \equiv \frac{R_1}{v_w} \tag{2.17}$$

is the crossing timescale (over which wind launched from the disk crosses the inner shock). The hot shocked wind is assumed to be effectively adiabatic over the span of $t_{c,sw}$ (except near R_1 and R_c), with wind shocked prior to $t - t_{c,sw}$ cooling primarily at $r \approx R_c$. There are then three global phases, discussed below, given by how $t_{c,sw}$ compares to t_{cr} and the flow timescale

$$t_{flow} \equiv \frac{R_2}{v_{R2}} = \frac{t}{\beta}. \tag{2.18}$$

The cooling of the shocked ambient region is irrelevant here, but is discussed in Section 2.2 in the context of local dynamics.

2.1.2.1 Momentum-driven/Radiative Outflows ($t_{c,sw} \lesssim t_{cr}$)

If $t_{c,sw} \lesssim t_{cr}$ then $t - t_{c,sw} \gtrsim t - t_{cr}$, and so the existing shocked wind cools faster than it is replaced by new shocked wind. The shocked wind region loses pressure support and is crushed into a thin shell at $R_1 \approx R_c$ ($\gamma_{sw} \approx 1$); the shock structure is then driven by the wind's momentum. Momentum conservation for the wind (KM92 Sections 2.1 and 4.1)

yields the self-similarity parameters

$$\begin{aligned} \beta_P &= \frac{2}{4-\alpha} \\ A_P &= (3/\beta)^{\beta/2}\frac{R_f}{t_f^\beta}. \end{aligned} \tag{2.19}$$

Note that the expression for A_P also assumes the thin shell approximation for the shocked ambient region ($\gamma_{sa} = 1$); in this case the shocked ambient region has mass $M_{sa} = 4\pi n_0 R_0^\alpha R_2^{3-\alpha}/(3-\alpha)$ and momentum $P_{sa} = M_{sa} v_{R2}$.[1]

2.1.2.2 Energy-driven/Adiabatic Outflows ($t_{c,sw} \gtrsim t_{flow}$)

If $t_{c,sw} \gtrsim t_{flow}$, cooling is inefficient over timescales of roughly the age of the outflow, and the energy of the wind is effectively conserved (after potential losses from prior phases); energy conservation for the wind (KM92 Section 3) yields the self-similarity parameters

$$\begin{aligned} \beta_E &= \frac{3}{5-\alpha} \\ A_E &= (2\pi\Gamma_{rad}\xi)^{\beta/3}\frac{R_f}{t_f^\beta}, \end{aligned} \tag{2.20}$$

where

$$\Gamma_{rad}\xi \equiv \frac{9(\gamma_{sw}-1)(\gamma_{sa}+1)}{8\pi\lambda_c^3\beta[3(\gamma_{sw}-1)\beta+1][(4-\alpha)\beta-1]}, \tag{2.21}$$

given by KM92 Eq. (3.10), is a factor $\leqslant 1$ (but not $\ll 1$) which, loosely speaking, represents a free energy deficit due to radiative losses from prior phases (Γ_{rad}) and entropy production (ξ). The $(\gamma_{sa}+1)$ and λ_c^3 terms in Equation (2.21) imply that A_E depends not just on α, but whether or not the thin shell approximation applies to the shocked ambient gas at time t ($\lambda_c = 1$ for $\gamma_{sa} = 1$ and less than 1 otherwise). KM92 show that $\Gamma_{rad}\xi$ is about a

[1] We note that for $\gamma_{sa} \neq 1$, one must determine $\rho_{gas}(r)$ and $v_{gas}(r)$ in the region via Equation (2.16), integrate $\rho_{gas}(r)v_{gas}(r)$ over the region $R_c < r < R_2$ to obtain P_{sa}, then apply conservation of momentum to obtain A_P.

factor of two lower when $\gamma_{sa} = 1$, compared to when $\gamma_{sa} = 5/3$.

2.1.2.3 Intermediate-phase/Partially Radiative Outflows ($t_{cr} \lesssim t_{c,sw} \lesssim t_{flow}$)

If $t_{cr} \lesssim t_{c,sw} \lesssim t_{flow}$, the shocked wind cools slowly enough to be replenished by fresh hot wind and maintain pressure support in the region, but cools quickly compared to the flow timescale, with cooled gas being compressed into a thin shell near the contact discontinuity. To determine A and β, KM92 approximates mass conservation for the ***hot*** shocked wind with the approximate expression $M_{sw}(t) \approx \dot{M}_w t_{c,sw}$, and thus unlike the radiative and adiabatic phases, the self-similarity parameters for the intermediate phase depend on the physics governing the cooling. However, the structural assumptions of the outflow (self-similarity and adiabatic hot shocked wind) lead to an approximation of M_{sw} that is independent of the cooling physics; for the purpose of analysing different cooling regimes, this means that the mass conservation method can equivalently be thought of as equating the cooling time's physical expression $t_{c,sw}$ (i.e., the one based on the cooling physics) to a cooling-independent expression $t_{c,sw}^{MC} \equiv M_{sw}/\dot{M}_w$ (superscript MC for "mass conservation"), then solving for A and β.

We provide an expression for $t_{c,sw}^{MC}$ below, giving a condensed derivation from the core aspects of KM92's method (see their Sections 3, 4.2 and Appendix B for more details).

Assuming that the hot gas is adiabatic before cooling, the density at any given time is roughly constant and equal to the post-shock density $\rho_{sw} \equiv \rho_{sw}(R_1)$ throughout the shocked wind region at any given time; the Rankine-Hugoniot jump conditions then give us

$$\rho_{sw} \approx K_\rho \rho_w(R_1), \tag{2.22}$$

where $\rho_w(R_1)$ (the wind density at R_1; see Equation 2.10) is the pre-shock density and

$$\begin{aligned} K_\rho &\equiv \frac{\gamma+1}{\gamma-1} \\ &= 4 \quad (\text{for } \gamma = 5/3). \end{aligned} \tag{2.23}$$

An approximate expression for $\rho_w(R_1)$ can be obtained by first considering the ratio f_P of post-shock ram pressures at R_1 and R_2:

$$f_P \equiv \frac{\rho_w(R_1)(v_w - v_{R1})^2}{\rho_a(R_2)v_{R2}^2}. \tag{2.24}$$

KM92 showed that this ratio can be approximated by

$$\begin{aligned} f_P &\approx \frac{(\gamma_{sw}+1)[(4-\alpha)\beta-1]}{(\gamma_{sa}+1)(3-\alpha)\beta}\left[\frac{4\gamma_{sw}}{(\gamma_{sw}+1)^2}\right]^{\gamma_{sw}/(\gamma_{sw}-1)} \\ &\approx 1.418\frac{[(4-\alpha)\beta-1]}{(\gamma_{sa}+1)(3-\alpha)\beta} \quad (\text{for } \gamma_{sw} = 5/3), \end{aligned} \tag{2.25}$$

which is of order one. Rearranging the definition of f_P (Equation 2.24) in the self similarity limit ($v_{R1} \ll v_w$) and applying Equation (2.22), we get the expression

$$\begin{aligned} \rho_{sw} &\approx 4\rho_w(R_1) \\ &\approx 4f_P\left(\frac{\mu m_p n_0 R_0^\alpha}{v_w^2}\right) R_2^{-\alpha} v_{R2}^2 \quad (\text{for } \gamma_{sw} = 5/3) \end{aligned} \tag{2.26}$$

where we have evaluated $\rho_a(R_2)$ using Equations (2.4) and (2.6); in subsequent expressions containing f_P we then use the approximate value of Equation (2.25). Finally, the constant density implies $M_{sw} \approx \rho_{sw}V_{sw}$, where $V_{sw} \approx (4\pi/3)R_c^3 = (4\pi/3)\lambda_c^3 R_2^3$ is the shocked wind volume (assuming $R_c \gg R_1$). Using Equations (2.3) and (2.26) we can evaluate

$t_{c,sw}^{MC} \equiv M_{sw}/\dot{M}_w = c v_w \rho_{sw} V_{sw}/\tau_w L_{AGN}$, giving us the final expression:

$$\begin{aligned} t_{c,sw}^{MC} &= K_\rho \lambda_c^3 f_P \left[\frac{4\pi\mu m_p c n_0 R_0^\alpha}{3 v_w \tau_w L_{AGN}}\right] R_2^{3-\alpha} v_{R2}^2 \\ &= \frac{K_\rho}{9}(3-\alpha)\lambda_c^3 f_P \left[\left(\frac{R_2}{R_f}\right)^{3-\alpha}\left(\frac{v_{R2}}{v_w}\right)^2\right] t_f. \end{aligned} \tag{2.27}$$

The equality on the second line can easily be shown using Equation (2.11) for spherical winds, and shows the structural, cooling-independent nature of $t_{c,sw}^{MC}$. We now have a starting point to derive the intermediate-phase self-similarity parameters: equate the physically-derived cooling time $t_{c,sw}$ to the mass conservation cooling time $t_{c,sw}^{MC}$, then solve for β_I and A_I using Equation (2.13).

In the context of global dynamics, this paper primarily considers the two-temperature plasma (TTP) cooling regime of FGQ12 (see their Section 2), which derives from the fact that protons and electrons are differentially heated by the wind shock at R_1; both have the same post-shock velocity, and so electrons have a factor $\sim (m_e/m_p)$ of the proton kinetic energy in the post-shock gas. Protons therefore exert the majority of the thermal pressure in the shocked wind region and free-free cooling is negligible, meaning that the cooling of the shocked wind amounts to the cooling of the protons therein. The regime assumes a weak thermal coupling between protons and electrons, and that thermal conduction is suppressed by sufficiently strong but dynamically unimpactful magnetic fields; FGQ12 obtain an analytic approximation of the proton/shocked wind cooling timescale given by

$$t_{c,sw}^{TTP} = K_{TTP}\left[\frac{\mu^3 v_w^8}{\tau_w^2 L_{AGN}^5}\right]^{1/5} R_2^2 v_{R2}^{2/5}, \tag{2.28}$$

with the constant K_{TTP} given below. Note that this cooling time assumes the thin shell approximation ($\lambda_c = 1$); an extension of the cooling to $\gamma_{sa} \neq 1$ is outside the scope of this work, though this would likely involve factors of λ_c, which is of order one and would

therefore likely not have a significant impact on the cooling time. The constant K_{TTP} is given by

$$K_{TTP} \equiv \left[\left(\frac{3^8\pi^4}{2^{19}}\right)\frac{m_e^2 m_p^7 c^8}{(\ln\Lambda)^2\sigma_T^3 e^8}\right]^{1/5} \approx \frac{124}{(\ln\Lambda)^{2/5}}\ \mathrm{g\,cm^{-2}}, \tag{2.29}$$

where e is the electron charge (in esu), σ_T is the Thomson cross section and $\ln\Lambda$ is the Coulomb logarithm (e.g., Spitzer 1962); we follow FGQ12 and adopt $\ln\Lambda = 40$; we do not expect this value to vary enough to substantially affect any relevant calculations, and thus for our purposes $K_{TTP} \approx 28\ \mathrm{g\,cm^{-2}}$. Equating $t_{c,sw}^{TTP}$ to $t_{c,sw}^{MC}$ in Equation (2.27) yields the self-similarity parameters

$$\begin{aligned} \beta_I^{TTP} &= \frac{8}{13-5\alpha} \\ A_I^{TTP} &= (K_I^{TTP}/\beta^8)^{\beta/8}, \end{aligned} \tag{2.30}$$

where

$$K_I^{TTP} = \left[\left(\frac{3K_{TTP}}{16\pi\lambda_c^3 m_p c}\right)^5 \frac{v_w^{13}\tau_w^3}{\mu^2 f_P^5 (n_0 R_0^\alpha)^5}\right]. \tag{2.31}$$

To illustrate how different cooling regimes can affect the self-similarity parameters, we consider a reference cooling regime (hereafter the REF cooling regime) with a typical cooling time of the form $t_c \equiv \varepsilon/n^2\Lambda(T)$, which describes the cooling of a parcel of fluid with energy density ε, number density n and temperature T. The cooling function $\Lambda(T)$ has units of erg cm^3 s^{-1} and takes on different forms in different temperature ranges. In the shocked wind, the energy is mostly thermal: the energy density is $\varepsilon = p = x_t nkT$ for an ideal gas, where k is the Boltzmann constant and $x_t = 1.1$ is the number of atomic nuclei per hydrogen nucleus for a gas of cosmic abundances(the latter of which accounts for non-hydrogen species in the equipartition theorem but neglects electrons due to differential shock heating). Combined with constant density (as described above) and post-shock temperature ($v_{R1} \ll v_w$ at late times and thus the post-shock velocity is approximately constant), we can evaluate n_{sw} using Equations (2.1) and (2.26) to get the expression for

the shocked wind cooling time:

$$t_{c,sw}^{REF} = \left[\left(\frac{x_t k}{K_\rho f_P}\right)\frac{v_w^2 T_{sw}}{n_0 R_0^\alpha \Lambda(T_{sw})}\right] R_2^\alpha v_{R2}^{-2}$$
$$= \left[\left(\frac{3m_p}{2^6 f_P}\right)\frac{\mu^{1-\eta} v_w^{4-2\eta}}{\Lambda_0 (T_{REF}/c^2)^\eta n_0 R_0^\alpha}\right] R_2^\alpha v_{R2}^{-2} \quad (\text{for } \Lambda(T) = \Lambda_0 T^\eta \text{ and } \gamma_{sw} = 5/3), \tag{2.32}$$

where for the second equality we have substituted $(3/2)x_t k T_{sw} = (9/32)\mu m_p v_w^2$ (from the jump conditions for an ideal gas) and defined

$$T_{REF} \equiv \frac{3m_p c^2}{16 x_t k} \approx 1.86 \cdot 10^{12} \text{ K}, \tag{2.33}$$

which gives $T_{sw} = \mu(v_w^2/c^2)T_{REF}$ with $T_{REF}/c^2 \approx 2.06 \cdot 10^{-9}$ K cm^{-2} s^2. This second equality is included for simple cooling functions $\Lambda(T) = \Lambda_0 T^\eta$, which are used in KM92 (collisionally ionised equilibrium cooling, superscript CIE) and ZH+20 (free-free cooling, superscript FF). Their parameters, with appropriate temperature ranges, are:

$$\eta^{CIE} = -1/2 \quad \text{and} \quad \Lambda_0^{CIE} = 1.6 \cdot 10^{-19} \text{ erg cm}^3 \text{ s}^{-1} \text{ K}^{1/2} \quad (\text{for } 5 \lesssim \log[T/\text{K}] \lesssim 7.5)$$
$$\eta^{FF} = +1/2 \quad \text{and} \quad \Lambda_0^{FF} = 1.4 \cdot 10^{-26} \text{ erg cm}^3 \text{ s}^{-1} \text{ K}^{-1/2} \quad (\text{for } \log[T/\text{K}] \gtrsim 7.5), \tag{2.34}$$

with the boundary of $T_{sw} = 10^{7.5}$ K between the two cooling regimes corresponding to a wind velocity $v_w \approx 1000$ km s^{-1}. Contrast this with KM92's boundary of $v_w \approx 1500$ km s^{-1}, which includes electrons in the equipartition theorem ($x_t = 2.3$); thus, for us, where we consider $v_w > 1{,}000$ km s^{-1}, all REF cooling in the shocked wind region is free-free cooling. The use of $x_t = 1.1$ corresponds to a two-temperature plasma, however Equation (2.34) corresponds to a one-temperature plasma. In the case of free-

free cooling, ZH+20's value of Λ_0^{FF} corresponds to the electron-dominated regime where $T_e \gg (m_e/m_p)T_p$ (e.g. Mayer 2007), but in consideration of whether or not the shocked region is adiabatic (Section 2.2.1), is conservatively higher than normal by a factor of 10. Mayer (2007) showed that Λ_0 may be substantially lower in a two-temperature plasma, deriving $\Lambda_0 \approx 3 \cdot 10^{-29}$ erg s^{-1} cm^3 K$^{-1/2}$ in the limit $T_e \ll (m_e/m_p)T_p$ where electrons are effectively at rest (assuming a Gaunt factor of 1; see their Equation (15)), but their general two-temperature expression (their Equation (13)) is non-trivial and thus we use the one-temperature expression for simplicity. This implies phase transition times (Section 2.1.3.5) and shell formation times (Section 2.2.1) are underestimated. As with the TTP regime, we equate $t_{c,sw}^{TTP}$ to $t_{c,sw}^{MC}$ in Equation (2.27) to get the self-similarity parameters

$$\begin{aligned} \beta_I^{REF} &= \frac{4}{7-2\alpha} \\ A_I^{REF} &= (K_I^{REF}/\beta^4)^{\beta/4}, \end{aligned} \tag{2.35}$$

with

$$\begin{aligned} K_I^{REF} &\equiv \left[\left(\frac{9x_t k}{8\pi\mu m_p c\lambda_c^3 K_\rho^2 f_P^2}\right)\frac{v_w^3\tau_w L_{AGN}}{(n_0 R_0^\alpha)^2}\frac{T_{sw}}{\Lambda(T_{sw})}\right] \\ &= \left[\left(\frac{3^3}{2^{11}\pi c\lambda_c^3 f_P^2}\right)\frac{\mu^{-\eta}v_w^{5-2\eta}\tau_w L_{AGN}}{\Lambda_0(T_{REF}/c^2)^\eta(n_0 R_0^\alpha)^2}\right] \quad \text{(for } \Lambda(T)=\Lambda_0 T^\eta \text{ and } \gamma_{sw}=5/3\text{).} \end{aligned} \tag{2.36}$$

The value of β_I^{REF} is not impacted by the cooling function, however A_I^{REF} is, with the value for simple cooling function $\Lambda(T) = \Lambda_0 T^\eta$ shown in the second line of Equation (2.36). Equations (2.30) and (2.35) give us $\beta_I^{REF} < \beta_I^{TTP}$ with $\beta_I^{TTP} \in (0.615, 1.455)$ and $\beta_I^{REF} \in (0.571, 1)$ for $\alpha \in (0, 1.5)$; thus, the intermediate-phase flow timescale $t_{flow} = t/\beta$ is shorter in the TTP cooling regime than in the REF regime at any given time.

2.1.2.4 Biconical Outflows

For biconical winds, the model of ZH+19 considers the entire shock structure as a whole (the "wind head"); they derive an expression (their Equation (A3)) for the head velocity, which at late times translates to (ZH+20 Equation (3)):

$$v_h \approx v_w (r/R_f)^{-(2-\alpha)}. \tag{2.37}$$

This gives us a simple one-phase outflow, which we refer to herein as the biconical phase: if we approximate $r \approx R_2$ and $v_h \approx v_{R2}$, then Equation (2.37) can be directly integrated and compared to Equation (2.13) to obtain:

$$\begin{aligned} \beta_B &= \frac{1}{3-\alpha} \\ A_B &= (1/\beta)^{\beta} \frac{R_f}{t_f^{\beta}}. \end{aligned} \tag{2.38}$$

This value of β_B is problematic for the assumption of self-similarity with regards to the shocked ambient region: we find that using β_B in the KM92 hydrodynamic equations (their Equation (B5); note that they use the notation k_ρ and η in place of α and β, respectively) causes the numerical solutions to fail for $\alpha \leqslant 1$, with the gas velocity falling to zero (or the velocity gradient becoming infinite) before the self-similarity condition $v_{Rc} = \lambda_c v_{R2}$ is realised.

2.1.2.5 Remarks

We conclude this section on with a comparison of the global outflow phases and some final remarks: we first note that, excepting the intermediate phase, A is equal to a constant multiple of R_f/t_f^{β}. These constants are of order one for each phase, since β and $\Gamma_{rad}\xi$ are of order one. This and the fact that $\beta_B < \beta_P < \beta_E$ for $\alpha < 2$ implies that adiabatic

outflows are larger in scale than radiative ones at late times, given similar free expansion radii. To compare biconical and spherical winds however, one must take into account the free expansion ratio φ_f from Equation (2.12); noting that $R_f/t_f^\beta = v_w^\beta R_f^{1-\beta}$, we see that

$$A_B = (1/\beta)^\beta \varphi_f^{1-\beta} \frac{R_{f,S}}{t_{f,S}^\beta}. \tag{2.39}$$

This additional factor of $\varphi_f^{1-\beta}$ implies that biconical outflows will be smaller in scale than spherical outflows for high θ_w (where φ_f theoretically approaches 1), and potentially the same or higher in scale for lower θ_w (where $\varphi_f \to \infty$). This is shown to be the case below, where Figure 2.3 shows that biconical and adiabatic spherical outflows are generally comparable in scale outside of the extreme angles (mostly within a factor of a few). These results must be taken with caution though, as the ZH+20 model is coarse in assuming that the velocity profile is the same for all times $t > t_f$ without regard to how cooling affects the global outflow dynamics. This may be appropriate if the wind cones suffer large radiative losses to the surrounding ambient medium, but otherwise it is not clear how well the spherical outflow phases should translate to biconical outflows, if at all. The simulations of ZH+19 and ZH+20 show the formation of "cocoon" shock structures, similar to the spherical "bubble" shock structure, suggesting that cooling does indeed play a role in determining the global outflow dynamics, but such an investigation is outside the scope of this work. With this in mind, along with the above-mentioned problems with the shocked ambient hydrodynamic equations, we focus solely on spherical winds from this point onward.

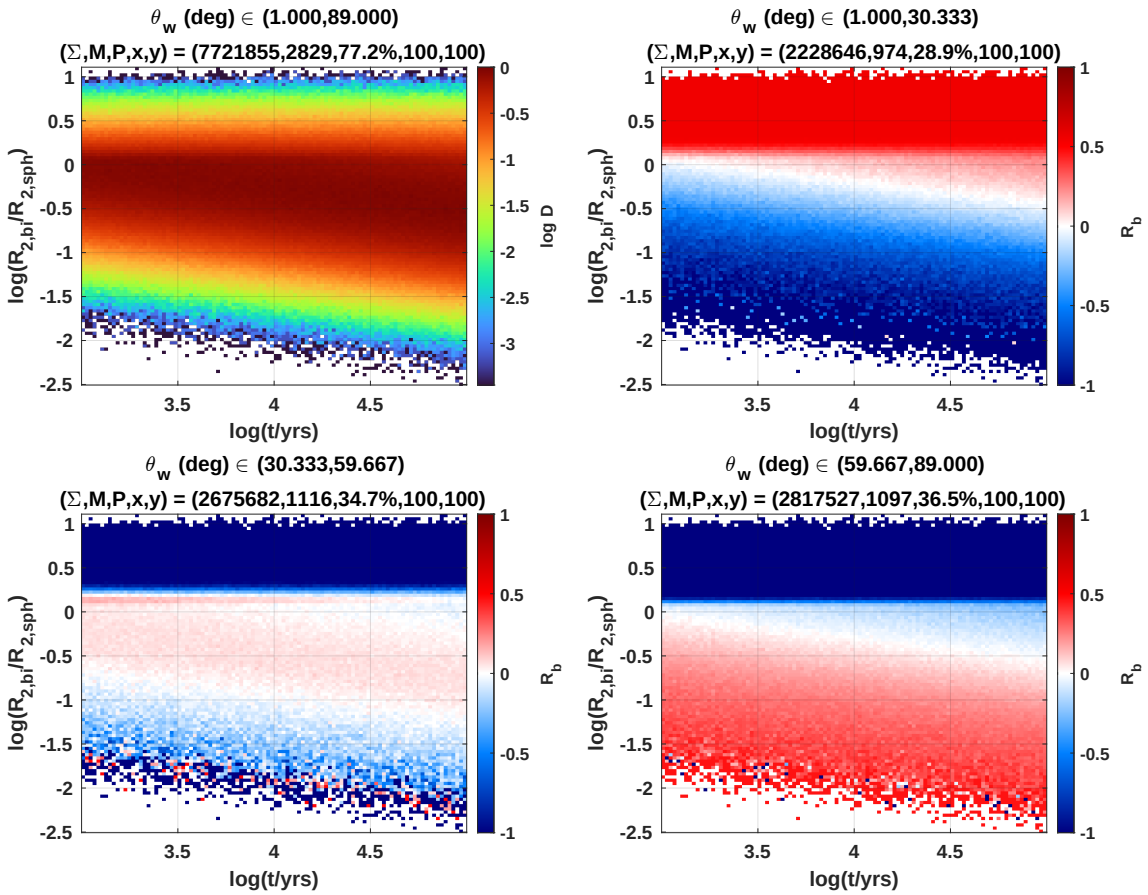

Figure 2.3: D&R mapping of $(\mathcal{X}(\texttt{ADI \& } t < t_{f,B}) : t, R_{2,bi}/R_{2,sph}, \theta_w)$, comparing the scale of biconical winds to that of adiabatic spherical winds over time. The main features are time t and forward shock position ratio (biconical wind to adiabatic spherical wind), with the biconical wind half-opening angle θ_w as the band feature. For the spherical winds, $\gamma_{sa} = 5/3$ is assumed, though this does not substantially affect the results. The D-map shows the ratio slightly decreasing over time overall (as is expected for $\beta_B < \beta_E$), with the data mostly clustered around a ratio of 1. The R-maps show the ratio increasing as θ_w decreases, due to the factor of $\varphi_f^{1-\beta}$ in Equation (2.39). The biconical outflows are mostly bigger in scale for $\theta_w \in (1^\circ, 30^\circ)$. See Appendix A for an explanation of D&R mapping (including Section A.1 for explanation of the numbers found in the subplot titles).

2.1.3 Stability & Evolution of Outflows

At late times, an outflow may transition from its current phase depending on the evolution of the shocked wind cooling time in that phase, along with stability considerations. In Sec-

tions 2.1.3.1 through 2.1.3.5 we summarise the evolutionary framework of KM92 derived throughout their sections 2 through 5; we then, in Section 2.1.3.6, show the distributions and trends in the initial phase parameter (Section 2.1.3.1) and phase transition times (Section 2.1.3.5). We also show that KM92's method for determining the intermediate-phase self-similarity parameters (Section 2.1.2.3) establishes a direct correspondence between the evolutionary framework and the hierarchy of late-time β values (Equation (2.13)), at least for TTP and REF cooling. We note that we do not treat the cases of pressure confinement (when the expansion of the outflow "bubble" becomes subsonic, which does not happen on the timescales we consider) and additional mass injection (KM92 Sections 4.4 and 5.3 respectively); KM92 show that pressure confinement may interfere with the transition from an adiabatic outflow to an intermediate-phase outflow (Section 2.1.3.3), but that this may be prevented by additional mass injection (for example, due to the mixing and/or evaporating of embedded clouds and/or the shocked ambient gas). However, analysis of these cases requires additional assumptions/model parameters regarding the speed of sound in the ambient medium and the amount of embedded mass. Therefore we neglect these cases in the interest of simplicity.

Combined with the self-similarity solution (Equation (2.13)), the simple form of the cooling timescales in Equations (2.28) and (2.32) implies that the outflow evolution is entirely determined by conditions on the ambient density gradient α, given the cooling regime and *initial phase* (the post-free expansion phase). We explicitly remind the reader here that the β values and cooling times in this paper (and in turn the above conditions on α) are for a fixed mass injection rate

$$\eta_{in} = 1 \quad (\text{for } \dot{M}_w \propto t^{\eta_{in}-1}), \tag{2.40}$$

and that a different value of η_{in} will affect how α governs the evolution of the outflow. This section details the evolution of outflows for the TTP and REF cooling regimes; we first

briefly introduce some convenient terms and notation regarding the initial phase before discussing the conditions for stability and phase transitions (taking the initial phase for granted), then proceed to examine the distribution of initial phases and phase transition times under the uniform sampling in Section 2.0.2.

2.1.3.1 Initial Phase

At the end of free expansion ($t = t_f$) outflows are either *initially radiative* if the shocked wind cooling timescale $t_{c,sw}(t_f) < t_f$, or *initially adiabatic* if $t_{c,sw}(t_f) > t_f$. This motivates the definition of the *criterion parameter*,

$$\mathcal{C} \equiv \frac{t_{c,sw}(t_f)}{t_f}, \tag{2.41}$$

so that $\mathcal{C} = 1$ separates initially radiative outflows ($\mathcal{C} < 1$) from initially adiabatic ones ($\mathcal{C} > 1$). This definition will help to give us a more quantitative picture of how the initial phases are distributed. The initial phase applies to both the shocked wind and shocked ambient gas. Initially radiative outflows will have $R_1 \approx R_c$ and $\lambda_c = 1$, while initially adiabatic outflows will have $R_1 < R_c$ and $\lambda_c < 1$.

2.1.3.2 Stability

The self-similarity solution of Equation (2.13) gives a shock front velocity and acceleration that can be written as

$$\begin{aligned} v_{R2} &= \frac{\beta R_2}{t} \\ a_{R2} &= (\beta - 1)\frac{v_{R2}}{t} \end{aligned} \tag{2.42}$$

(with analogous quantities for R_1, R_c, etc.), and thus outflows with $\beta > 1$ are accelerating; these will be subject to the Rayleigh-Taylor instability (e.g., Taylor 1950b, Livescu 2004,

Ribeyre et al. 2004), whereby the interface between the ambient and shocked ambient gas (i.e. the outer shock) is unstable to perturbations (which will grow exponentially in amplitude over time). The evolution of such outflows is uncertain, but the instability will likely increase the cooling rate in the shocked wind region by mixing hot and cold gas, making the outflow radiative; if the outflow is already radiative, the shocked wind region is a thin shell, and the instability could potentially destroy the shock structure. The condition $\beta > 1$ is equivalent to $\alpha > 2$ for radiative or adiabatic outflows and $\alpha > 1$ (TTP) or $\alpha > 1.5$ (REF) for intermediate-phase outflows; since all outflows where $\alpha > 2$ are unstable, we do not discuss outflows with $\alpha > 2$ further due to the above-mentioned uncertain evolution. The case of $\beta = 1$ yields $a_{R2} = 0$, corresponding to a constant-velocity outflow, which includes the intermediate-phase cases of $\alpha = 1$ (TTP) or $\alpha = 1.5$ (REF) in addition to the special case of $\alpha = 2$ discussed in Section 2.1.1. Note though, that these $\beta_I = 1$ outflows are different from an $\alpha = 2$ outflow; the former will transition or remain partially radiative (intermediate-phase), while the latter is a single unchanging phase similar to free expansion, separate from the normal free expansion and late-time phases.

We reject outflows in our dataset $\mathcal{X}$ that would qualify as unstable; this excludes about 13% of the random outflows, with those having higher wind speeds being more likely to be rejected.

2.1.3.3 Phase Transitions

Ignoring stability for a moment, observe the fact that the definition of the late-time outflow phases implies that radiative outflows eventually become partially radiative (intermediate-phase) if $t_{c,sw}/t_{cr}$ increases over time, or else remain radiative. Adiabatic outflows similarly become partially radiative if $t_{c,sw}/t_{flow}$ decreases with time, or else remain adiabatic. Intermediate-phase outflows can then become radiative (decreasing $t_{c,sw}/t_{cr}$), adiabatic

(increasing $t_{c,sw}/t_{flow}$) or remain partially radiative (increasing $t_{c,sw}/t_{cr}$ but decreasing $t_{c,sw}/t_{flow}$). This translates to a set of transition conditions for the various phases, given explicitly in the next section. We refer to stable phases in which the outflow does not meet any transition conditions as *steady*; outflows that transition to a steady phase remain in that phase for as long as the self-similarity solution is appropriate.

2.1.3.4 Evolution

Combining Sections 2.1.3.1, 2.1.3.2 and 2.1.3.3, we see that outflows transition through various phases following free expansion until they reach a steady or unstable state; for the TTP and REF cooling regimes, outflow always reach a terminal phase (steady or unstable). To summarise, a given outflow phase is stable if the instability condition

$$\beta > 1 \quad \text{(outflow unstable/evolution uncertain)} \tag{2.43}$$

does not apply; for stable outflows, the transition conditions for the various phases (pre-transition phase to post-transition phase) are

$$\begin{aligned} \frac{d}{dt}\left(\frac{t_{c,sw}}{t_{cr}}\right) &< 0 \quad \text{(radiative/intermediate to radiative)} \\ \frac{d}{dt}\left(\frac{t_{c,sw}}{t_{flow}}\right) < 0 < \frac{d}{dt}\left(\frac{t_{c,sw}}{t_{cr}}\right) &\quad \text{(any phase to intermediate)} \\ \frac{d}{dt}\left(\frac{t_{c,sw}}{t_{flow}}\right) &> 0 \quad \text{(intermediate/adiabatic to adiabatic),} \end{aligned} \tag{2.44}$$

where the expressions for β, $t_{c,sw}$ and t_{cr} are evaluated for the given (pre-transition) phase. A stable phase is steady if it meets the transition condition in which the pre- and post-transition phases are the same. For the TTP/REF cooling times in Equations (2.28) and (2.32), self-similarity (Equation 2.13) and the stability/transition conditions above translate to simple conditions on α, i.e. upper and/or lower bounds (for fixed values of

η_{in}).

It turns out that KM92's mass conservation method of determining β_I (Section 2.1.2.3) establishes a correspondence between the steady phase of the outflow (along with the transition conditions on α, at least for TTP and REF cooling) and the hierarchy of late-time β values: combining Equations (2.10), (2.13), (2.17), (2.22) and (2.26) yields $t_{cr} \propto R_1 \propto t^{1-\beta_I((2-\alpha)/2)}$ for the intermediate phase, while Equation (2.18) directly gives $t_{flow} \propto t$. Setting $(t_{c,sw})_I = t_{c,sw}^{MC}$ (using $\beta = \beta_I$ in Equation (2.27), since it applies to the intermediate phase) gives $(t_{c,sw})_I \propto t^{\beta_I(5-\alpha)-2} = t^{3(\beta_I/\beta_E-1)+1}$, and it becomes clear that $(t_{c,sw}/t_{cr})_I \propto t^{3(\beta_I/\beta_P-1)}$ and $(t_{c,sw}/t_{flow})_I \propto t^{3(\beta_I/\beta_E-1)}$. Taking the time derivatives of $(t_{c,sw}/t_{cr})_I$ and $(t_{c,sw}/t_{flow})_I$ then shows a direct correspondence to the transition conditions in Equation (2.44) for the intermediate phase. Intuitively, this result shows the outflow's "response" to a transition into the intermediate phase; for example, a radiative outflow with $\beta_I < \beta_P$ will always be "pushed back" to the radiative phase upon transitioning to the intermediate phase, and thus in this case the radiative phase is steady. Likewise, adiabatic outflows where $\beta_I > \beta_E$ will remain adiabatic and intermediate-phase outflows where $\beta_P < \beta_I < \beta_E$ will remain in the intermediate phase.

In light of this correspondence, we make note of the cases not covered by Equation (2.44). First, the case of $(d/dt)((t_{c,sw})_I/t_{cr}) < 0 < (d/dt)((t_{c,sw})_I/t_{flow})$ implies $\beta_E < \beta_I < \beta_P$, corresponding to an unstable $\alpha > 2$ case by virtue of $\beta_E < \beta_P$. The cases of $(d/dt)((t_{c,sw})_I/t_{cr}) = 0$ and $(d/dt)((t_{c,sw})_I/t_{flow}) = 0$ respectively imply $\beta_I = \beta_P$ and $\beta_I = \beta_E$, which correspond to outflows with two steady phases: the radiative/intermediate phases in the former case, and the adiabatic/intermediate phases in the latter. In these cases the terminal phase of the outflow is dependent on the initial phase; for example, in the $\beta_I = \beta_P$ case an initially radiative outflow with will remain radiative, while an initially adiabatic outflow will transition to and remain in the intermediate phase. The special case of $(d/dt)((t_{c,sw})_I/t_{cr}) = (d/dt)((t_{c,sw})_I/t_{flow}) = 0$ implies $\beta_P = \beta_E$, which

corresponds to the "permanent free expansion" case ($\alpha = 2$) discussed in Section 2.1.1, but this constitutes an overdetermined system of equations unless $\alpha = 2$ implies $\beta_I = 1$.

By determining the stable and unsteady phases for a given outflow as described above, one may then determine the outflow evolution by following the "transition path" of the outflow phases (starting with the transition to the initial phase from free expansion), until a steady or unstable phase is reached. If we consider free expansion and unstable outflows as individual "phases", we can represent the outflow evolution sequence for a particular cooling law as a phase transition diagram, analogous to the state transition diagrams used to represent Markov chains (among other things). Figures 2.4 and 2.5 show the $\eta_{in} = 1$ phase transition diagrams for the TTP and REF cooling regimes respectively; these offer a comparison of the global dynamics between both regimes. Also note that the special constant-velocity case $\alpha = 2$ is represented as the transition $F \to F$ on the phase transition diagrams. We see that for TTP cooling, in contrast to REF cooling, outflows become or remain adiabatic for a wider range of density profiles, including uniform density ($\alpha = 0$) and slight central underdensities ($-1/7 < \alpha < 0$). However, initially radiative outflows are subject to a lower instability threshold in the intermediate phase ($\alpha > 1$ instead of $\alpha > 1.5$).

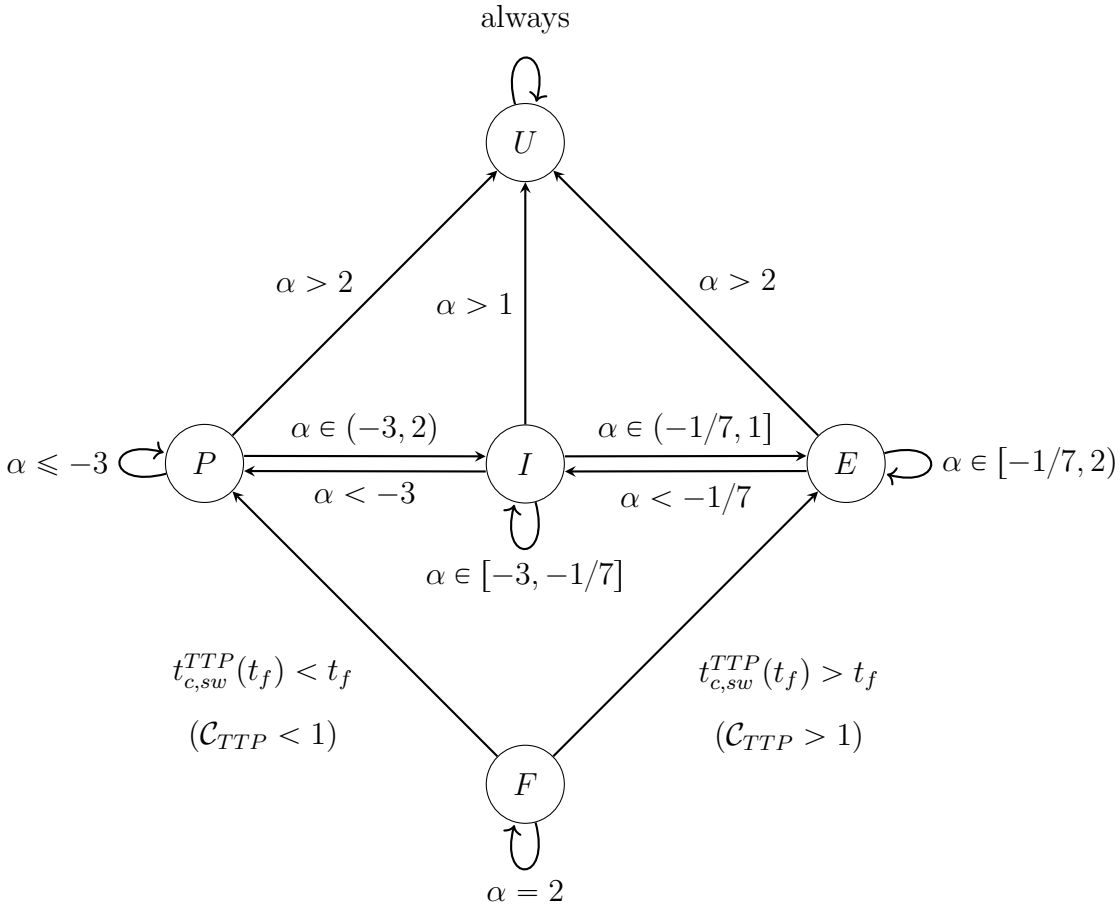

Figure 2.4: Phase transition diagram for the $\eta_{in} = 1$ TTP cooling regime. The nodes $\{F, P, I, E, U\}$ respectively refer to the free expansion, radiative (P for momentum-driven), intermediate, adiabatic (E for energy-driven) and unstable/uncertain phases. The conditions next to the edges must be satisfied for the corresponding transition to occur; the transition $F \to F$ represents the constant-velocity outflow case mentioned in Section 2.1.1. Outflows with $\alpha > 2$ are always unstable, while outflows with $\alpha < 2$ only experience instabilities if the outflow is initially radiative with $\alpha \in (1, 2)$, in which case the outflow becomes unstable when transitioning to the intermediate phase.

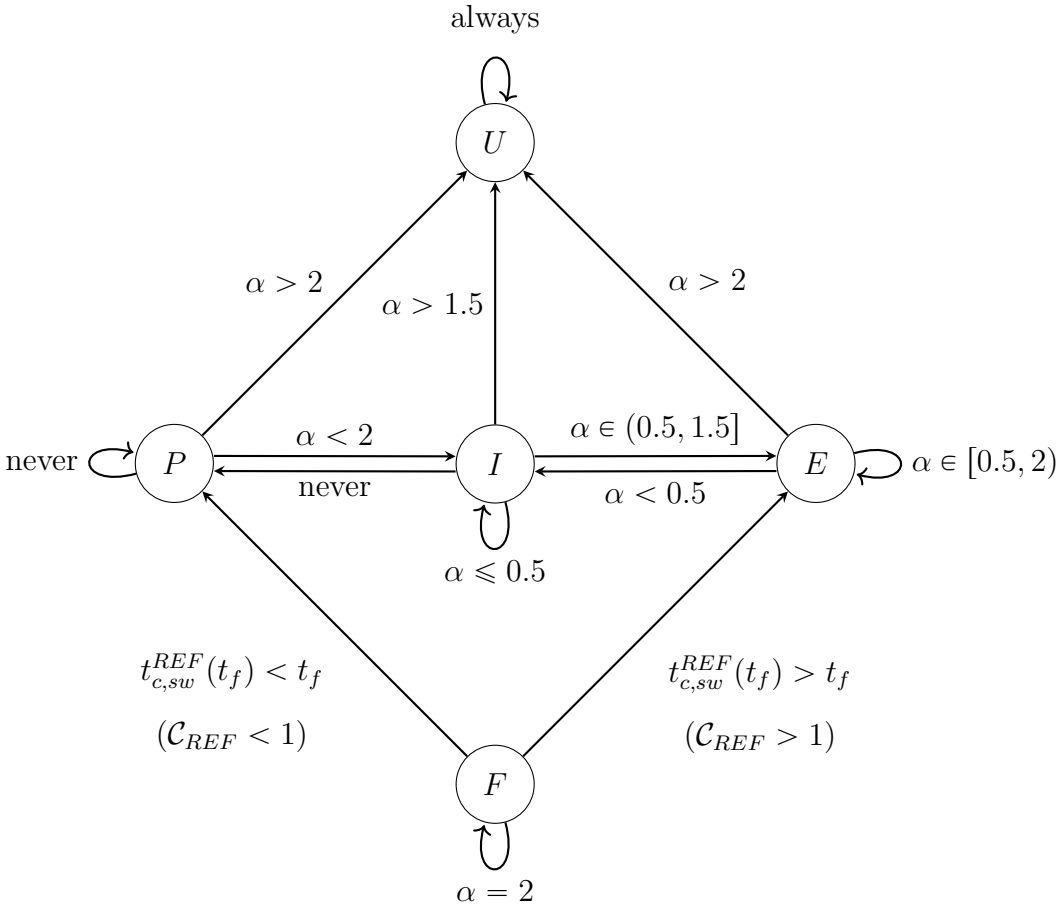

Figure 2.5: Phase transition diagram for the $\eta_{in} = 1$ REF cooling regime (a typical astrophysical cooling regime). The nodes $\{F, P, I, E, U\}$ respectively refer to the free expansion, radiative (P for momentum-driven), intermediate, adiabatic (E for energy-driven) and unstable/uncertain phases. The conditions next to the edges must be satisfied for the corresponding transition to occur; the transition $F \to F$ represents the constant-velocity outflow case mentioned in Section 2.1.1. Outflows with $\alpha > 2$ always become unstable, whereas outflows with $\alpha < 2$ only experience instabilities if the outflow is initially radiative with $\alpha \in (1.5, 2)$, in which case the outflow becomes unstable when transitioning to the intermediate phase.

2.1.3.5 Transition Times

Now that we have the general evolutionary trajectory for an outflow, i.e. the conditions that determine *if* certain transitions occur, it remains to show *when* those transitions

occur. Our sampling interval of $\alpha \in (0, 1.5)$ implies that radiative outflows always transition to intermediate outflows (ignoring instabilities). This gives us three phase transition times of interest: t_{PI} (radiative to intermediate) and t_{IE} (intermediate to adiabatic) for initially radiative outflows, and t_{EI} (adiabatic to intermediate). These are defined by:

$$\frac{t_{c,sw}(t_{PI})}{t_{cr}(t_{PI})} = 1 \quad \text{(radiative to intermediate)}, \tag{2.45}$$

$$\frac{t_{c,sw}(t_{IE})}{t_{flow}(t_{IE})} = 1 \quad \text{(intermediate to adiabatic)}, \tag{2.46}$$

and

$$\frac{t_{c,sw}(t_{EI})}{t_{flow}(t_{EI})} = 1 \quad \text{(adiabatic to intermediate)}, \tag{2.47}$$

where $t_{c,sw}$, t_{cr} and t_{flow} are evaluated in the pre-transition phase (radiative, intermediate and adiabatic for Equations 2.45, 2.46 and 2.47 respectively); because the model is approximate, the transition time between two states is not the same in the forward and reverse direction. We ignore this and simply use the transition times, given α and the initial phase, that match the evolutionary path of the phase transition diagram. Regardless, one must still check for consistency, with initially radiative bubbles by making sure that $t_f < t_{PI} < t_{IE}$ and with initially adiabatic bubbles by making sure that $t_{EI} < t_f$; these checks are incorporated into the generation procedure for the master dataset $\mathcal{X}$ (using the TTP cooling regime and the `PASS` filter in Table 2.2).

We mention in passing our observations of the rejected data: the consistency checks reject $\sim 6\%$ of parameter combinations under the uniform sampling regime, all of which are intially radiative outflows in a small band $\log \mathcal{C} \in (-0.32, 0)$; this likely reflects the fact that the self-similarity assumption requires that the system be far away from major transitional boundaries (Barenblatt & Zel'dovich 1972), and thus parameter combinations that yield $\log \mathcal{C} \sim 0$ may be problematic. A near-complete absence of data is left in this band, which can be seen in the $(\alpha, \log \mathcal{C})$ D-maps in Section 2.1.3.6. Most of the rejected

data have slower wind velocities (specifically, winds with $v_w < 10,000$ km s^{-1} constitute roughly 75% of the rejected data), with faster winds tending to be be rejected at steeper density gradients; there is nothing otherwise immediately remarkable about the rejected data, and including them does not substantially affect any D&R map sets explored herein.

2.1.3.6 Distributions & Trends

With the stability and phase transition conditions established, we now analyse the distribution of initial phases and transition times under the uniform sampling methods in Section 2.0.2. Of course, the true distribution of states depends on the true distribution of parameters, but uniform random sampling is still at least qualitatively informative.

Regarding initial phases, we analyse the initial criterion parameter $\mathcal{C}$ as mentioned in Section 2.1.3.1. Briefly recalling that $t_f = R_f/v_w$, we have the TTP criterion parameter

$$\mathcal{C}_{TTP} \equiv \frac{t_{c,sw}^{TTP}(t_f)}{t_f} = K_{TTP}\frac{\mu^{3/5}v_w^3 R_f}{\tau_w^{2/5}L_{AGN}} \propto \left[\mu^{1-3\alpha}L_{AGN}^{-5(1-\alpha)}v_w^{5(4-3\alpha)}\tau_w^{1+2\alpha}\right]^{\frac{1}{5(2-\alpha)}}. \tag{2.48}$$

We see that for μ, τ_w, v_w and L_{AGN}, there are corresponding values of α at which trends in $\mathcal{C}_{TTP}$ with respect to these parameters reverse (the other parameters reverse trends at $\alpha > 2$ which, again, we do not consider due to instability). For μ this is unimportant since it is of order one, however τ_w, v_w and L_{AGN} may range over several orders of magnitude (ignoring likely correlations between them), and thus their critical α values are worth noting. They are:

$$\alpha_L^{TTP} = 1; \quad \alpha_v^{TTP} = 4/3; \quad \alpha_\tau^{TTP} = -1/2, \tag{2.49}$$

where we have used subscripts L, v and τ to respectively indicate L_{AGN}, v_w and τ_w. The D&R map sets of Figures 2.6, 2.7 and 2.8 show the trends in $\log \mathcal{C}_{TTP}$ with respect to L_{AGN}, v_w and τ_w, in accordance with Equation (2.48). Since the sampling interval $\alpha \in (0, 1.5)$ is outside the stationary point α_τ, we see that outflows with higher τ_w tend

to be initially adiabatic, with no trend reversal; for L_{AGN}, lower luminosity AGN tend to be initially adiabatic for $\alpha < \alpha_L$, and initially radiative for $\alpha > \alpha_L$. For v_w, despite the critical point of $\alpha_v^{TTP} = 4/3$, we do not see many initially adiabatic outflows at low wind speeds beyond this point, due to these outflows having very long free expansion times (we reject outflows where $t < t_f$).

Analogous to the TTP cooling regime, one obtains for the REF regime:

$$\begin{aligned}\mathcal{C}_{REF} \equiv \frac{t_{c,sw}^{REF}(t_f)}{t_f} &= \left[\left(\frac{3m_p}{16K_\rho f_P}\right)\frac{\mu^{1-\eta}v_w^{3-2\eta}R_f^{\alpha-1}}{\Lambda_0(T_{REF}/c^2)^\eta n_0 R_0^\alpha}\right] \\ &= \left[\left(\frac{m_p}{2^6}\right)\frac{(3-\alpha)\mu^{1-\eta}v_w^{3-2\eta}R_f^{\alpha-1}}{\Lambda_0(T_{REF}/c^2)^\eta n_0 R_0^\alpha}\right] \quad (\text{for } \gamma_{sw} = 5/3) \\ &\propto \left[(L_{AGN}\tau_w)^{-(1-\alpha)}v_w^{(8-4\eta)-(5-2\eta)\alpha}\right]^{\frac{1}{2-\alpha}},\end{aligned} \tag{2.50}$$

noting that in the second equality we have evaluated $f_P(t_f) = 3/(3-\alpha)$ from the definition in Equation (2.24) with $R_1 = R_2 = R_f$, $v_{R1} = v_{R2} = v_w/2$ and $\rho_w(R_f) = \bar{\rho}_a(R_f)$. This gives the stationary points

$$\alpha_L^{REF} = 1; \quad \alpha_v^{REF,CIE} = 5/3; \quad \alpha_v^{REF,FF} = 3/2; \quad \alpha_\tau^{REF} = 1 \tag{2.51}$$

(where as with Equation (2.49) we have used subscripts L, v and τ to respectively indicate L_{AGN}, v_w and τ_w), and shows that the most notable difference in trends between the two cooling regimes is that with TTP cooling, the tendency of more relatively higher-momentum winds to be initially adiabatic extends over the whole range of $\alpha \in (-1/2, 2)$. We note in passing that for both free-free and CIE cooling (disregarding stability or consistency checks for those regimes), the D&R-mappings of $(\mathcal{X} : \alpha, \mathcal{C}_{REF}, \{L_{AGN}, v_w, \tau_w\})$ are analogous in terms of profile shape and trends to those found in Figures 2.6 through 2.8 for TTP cooling, but the profiles are scaled/translated and the R-map trends are

as appropriate for the stationary points in Equation (2.51). We find the minimum $\log \mathcal{C}$ values to be similar for all three cooling mechanisms, while the maximum $\log \mathcal{C}$ values differ between mechanisms (~ 5, 7.5 and 12 for TTP, free-free and CIE cooling respectively) but in all cases are roughly constant with respect to α. Thus for all three cooling regimes we see that the initial phase following free expansion is predominantly adiabatic for $\alpha \lesssim 1$, with initially radiative outflows becoming more common at higher α, yet TTP cooling is still distinct from the REF regimes in terms of evolutionary paths (Figures 2.4 and 2.5).

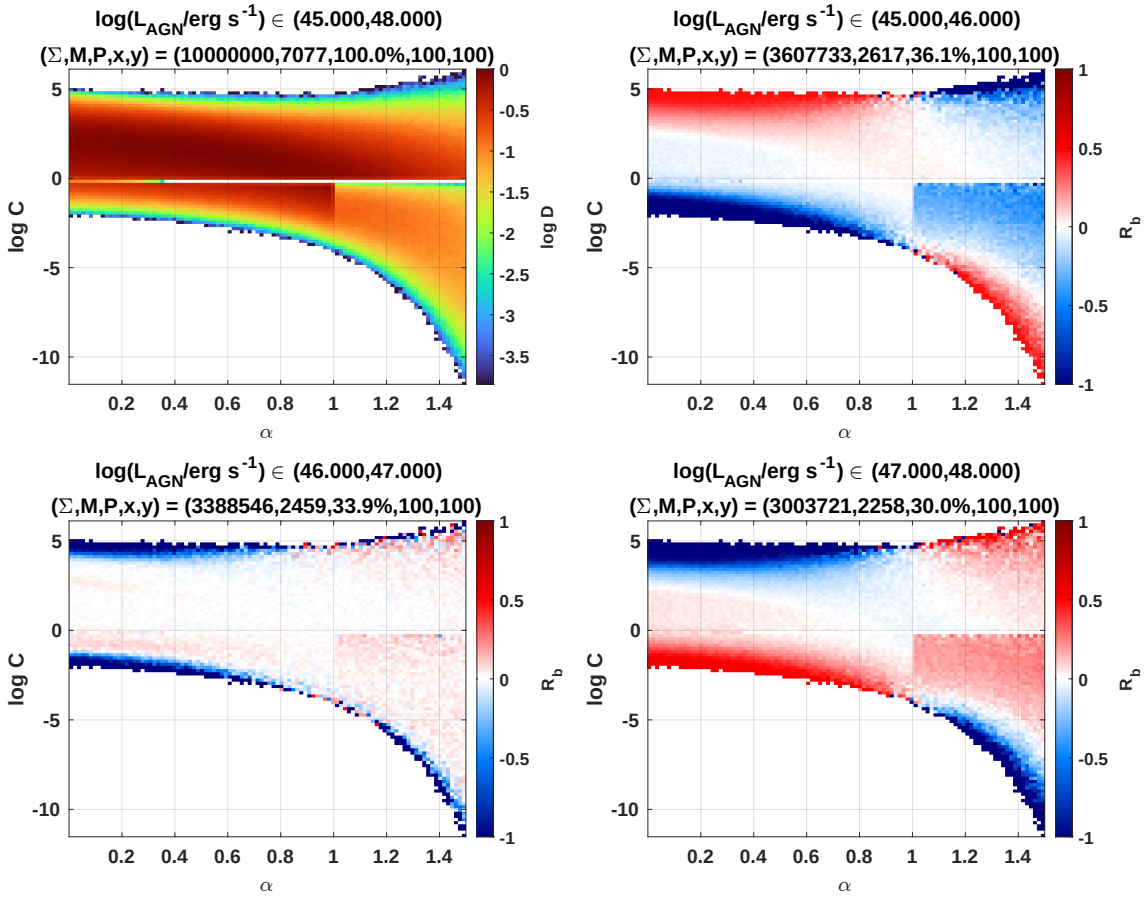

Figure 2.6: D&R Mapping of $(\mathcal{X} : \alpha, \mathcal{C}_{TTP}, L_{AGN})$ showing the trends in $\log \mathcal{C}$ with respect to L_{AGN} in accordance with Equation (2.48), and showing the stationary point $\alpha_L = 1$ in Equation (2.49). Lower luminosities have a greater tendency to be initially adiabatic below α_L, with the opposite being true above above α_L. The irregularities in the maps are due to rejected data, particularly unstable outflows (the irregular patch of data where $\log \mathcal{C} < 0$, $\alpha > 1$) and out-of-order transition times (horizontal white line). See Appendix A for an explanation of D&R mapping (including Section A.1 for explanation of the numbers found in the subplot titles).

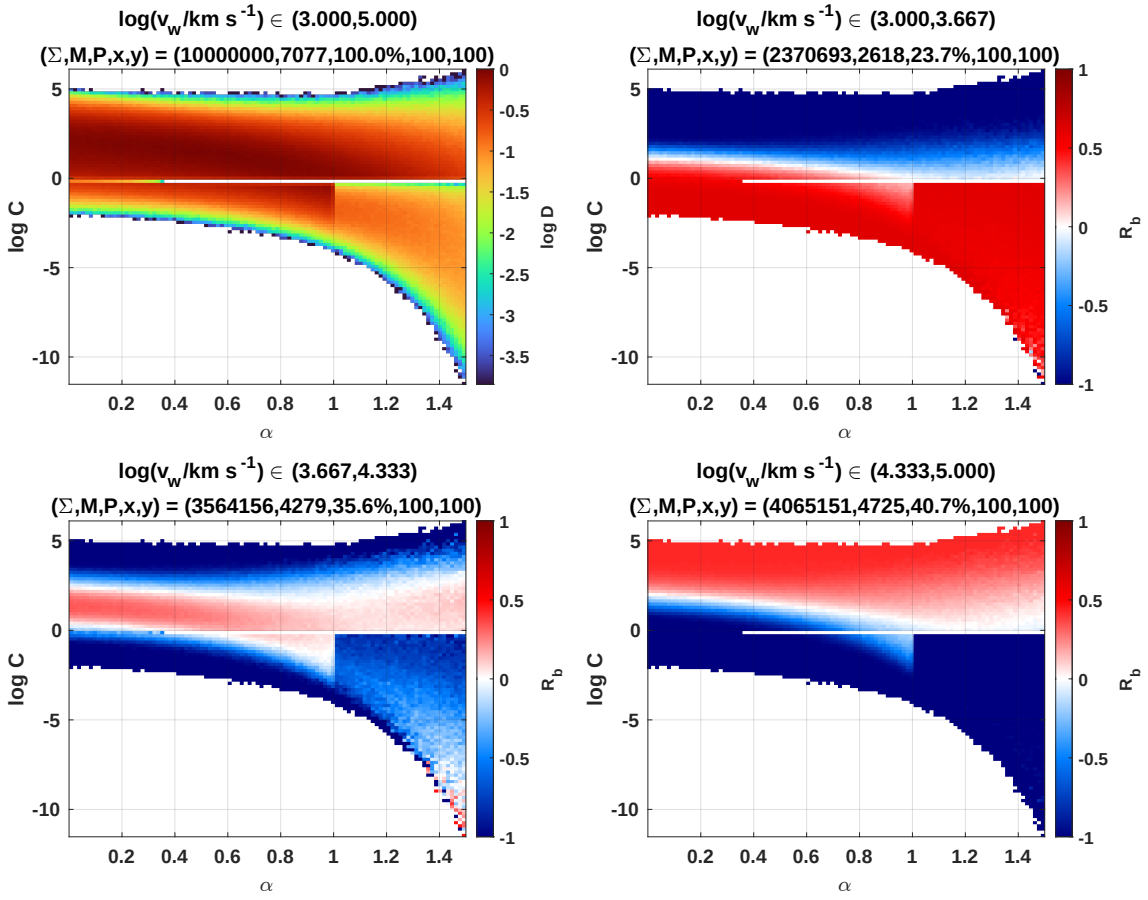

Figure 2.7: D&R Mapping of $(\mathcal{X} : \alpha, \mathcal{C}_{TTP}, v_w)$ showing the trends in $\log \mathcal{C}$ with respect to v_w in accordance with Equation (2.48). Despite the critical point of $\alpha_v^{TTP} = 4/3$, we do not see many initially adiabatic outflows at low wind speeds beyond this point, due to these outflows having very long free expansion times (we reject outflows where $t < t_f$). We see that at higher outflow velocities, initially radiative outflows are only found at higher values of α. The other irregularities in the maps are also due to rejected data, particularly unstable outflows (the irregular patch of data where $\log \mathcal{C} < 0$, $\alpha > 1$) and out-of-order transition times (horizontal white line). See Appendix A for an explanation of D&R mapping (including Section A.1 for explanation of the numbers found in the subplot titles).

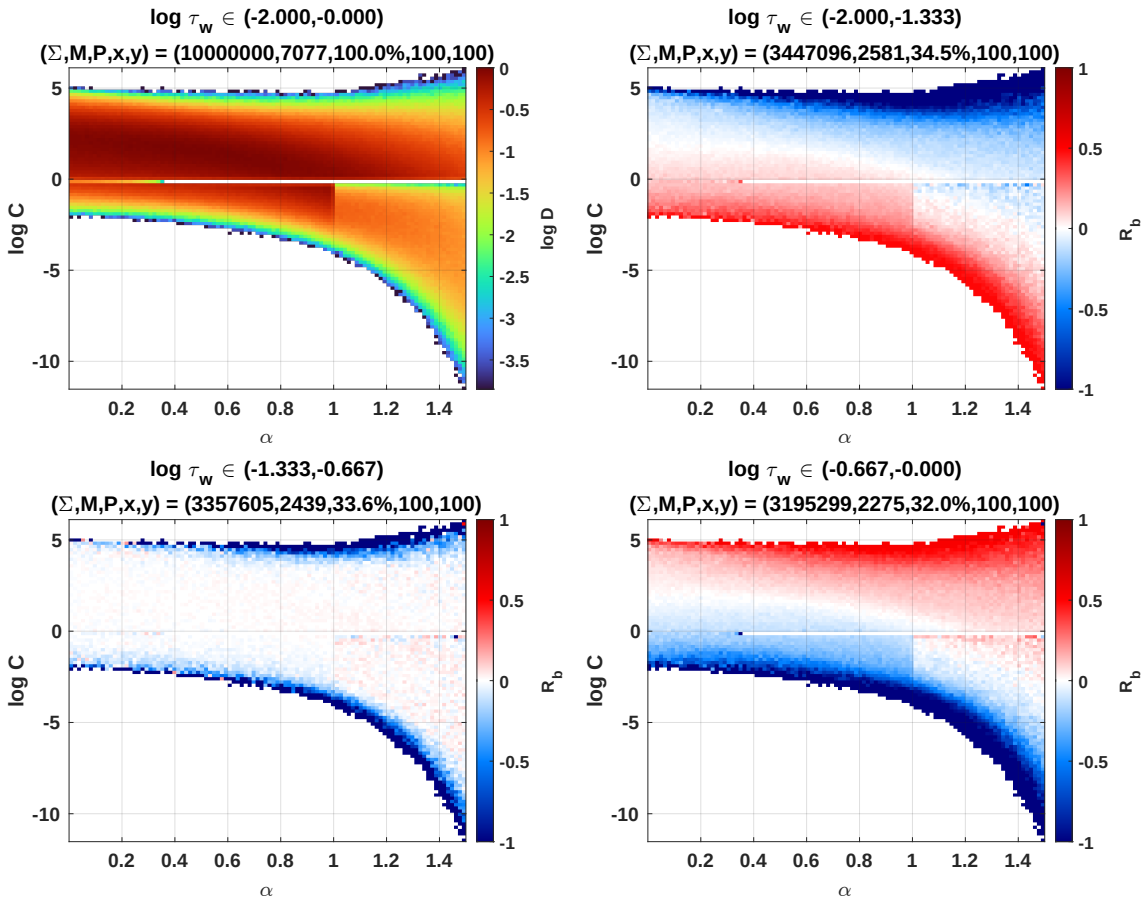

Figure 2.8: D&R Mapping of $(\mathcal{X} : \alpha, \mathcal{C}, \tau_w)$ showing the trends in $\log \mathcal{C}$ with respect to τ_w in accordance with Equation (2.48), with the stationary point $\alpha_\tau = -1/2$ in Equation (2.49) not shown, due to the sampling interval $\alpha \in (0, 1.5)$. We see that there are initially adiabatic and radiative bubbles across the entire range of τ_w, with initially adiabatic outflows being more common at higher τ_w. The irregularities in the maps are due to rejected data, particularly unstable outflows (the irregular patch of data where $\log \mathcal{C} < 0$, $\alpha > 1$) and out-of-order transition times (horizontal white line). See Appendix A for an explanation of D&R mapping (including Section A.1 for explanation of the numbers found in the subplot titles).

Regarding transition times, in this work we analyse only the the TTP regime; primarily because the TTP transition times are built into the consistency checks for the master dataset $\mathcal{X}$ (i.e., into the `PASS` filter in Table 2.2), but also because, of the two REF sub-regimes considered (Section 2.1.2.3), CIE cooling only applies for wind speeds $\lesssim$ 1000 $\mathrm{km\,s^{-1}}$ while our Λ_0 value for free-free cooling is overestimated by a factor of at

least 10 (leading to highly inflated or deflated transition times by analogy to Equations (2.53) through (2.55) below). Using the definitions of the crossing and flow times in Equations (2.17) and (2.18), the TTP cooling time expression in Equation (2.28) and the self-similarity assumption of Equation (2.13), one can easily show that

$$\begin{aligned}\left(\frac{t_{c,sw}^{TTP}}{t_{cr}}\right)^5 &= \beta^2 K_{TTP}^5 \left[\frac{\mu^3 v_w^{13} A^{12}}{\tau_w^2 L_{AGN}^5}\right] R_1^{-5} t^{12\beta-2}; \\ \left(\frac{t_{c,sw}^{TTP}}{t_{flow}}\right)^5 &= \beta^7 K_{TTP}^5 \left[\frac{\mu^3 v_w^8 A^{12}}{\tau_w^2 L_{AGN}^5}\right] t^{12\beta-7}.\end{aligned} \tag{2.52}$$

To get the transition times t_{PI}, t_{IE} and t_{EI}, we use Equations (2.45) through (2.47), noting that $R_1 \approx R_c = \lambda_c A t^\beta$ for the radiative phase, and simply use the values of A and β for the pre-transition phase. This yields

$$t_{PI} = \left[\frac{\lambda_c^5 \tau_w^2 L_{AGN}^5}{\beta_P^2} K_{TTP}^5 \mu^3 v_w^{13} A_P^7\right]^{1/(7\beta_P-2)}, \tag{2.53}$$

$$t_{IE} = \left[\frac{\tau_w^2 L_{AGN}^5}{\beta_I^7} K_{TTP}^5 \mu^3 v_w^8 A_I^{12}\right]^{1/(12\beta_I-7)} \tag{2.54}$$

and

$$t_{EI} = \left[\frac{\tau_w^2 L_{AGN}^5}{\beta_E^7} K_{TTP}^5 \mu^3 v_w^8 A_E^{12}\right]^{1/(12\beta_E-7)}. \tag{2.55}$$

We note again that the TTP cooling time assumes the thin shell approximation; an extension to the TTP cooling time where $\lambda_c < 1$ (in which factors of λ_c may appear in the denominator) may increase these transition times. The shocked ambient region will be in the same initial phase as the overall outflow, and thus the consistency checks for initially adiabatic outflows may rule out slower winds in the parameter space. Either way, since these checks are implemented in the generation of the master dataset $\mathcal{X}$, the distribution of t_{EI} is not relevant for $\alpha > -1/7$. For initially radiative outflows, it is technically possible

that the shocked ambient region becomes adiabatic before the outflow does (see Section 2.2.1), but we do not address this in the context of the transition times. The D&R mapping of $(\mathcal{X}(\texttt{IR}) : t_{PI}, t_{IE}, \alpha)$ is given in Figure 2.9, and shows that intially radiative outflows (where v_w is small) in near-uniform density gradients ($\alpha \sim 0$) have very long radiative and intermediate phases. We also find that the "wing" of outflows with long transition times have $R_1 \lesssim 2R_c$ in the intermediate phase, and thus these outflows borderline violate our assumption that $R_1^3 \ll R_c^3$ (so that the shocked wind volume is approximately $(4\pi/3)R_c^3$). Outflows where $v_w > 10{,}000$ km s^{-1} make up $\sim 10\%$ of initially radiative outflows in our sampling regime; the D&R mapping of $(\mathcal{X}(\texttt{IR \& FAST}) : t_{PI}, t_{IE}, v_w)$ is given in Figure 2.10, and shows that the transition to the adiabatic phase occurs quickly for very fast winds ($t_{IE} \lesssim 10^3$ years for $v_w \gtrsim 30{,}000$ km s^{-1}), but may take as long as 10^6 years for winds with $v_w \approx 10{,}000$ km s^{-1}. These longer values of t_{IE} occur for more luminous AGN, due to L_{AGN} spanning three orders of magnitude and having a dominant exponent in Equation (2.54); α is always high in these fast wind cases since fast winds with low α tend to be initially adiabatic (Figure 2.7).

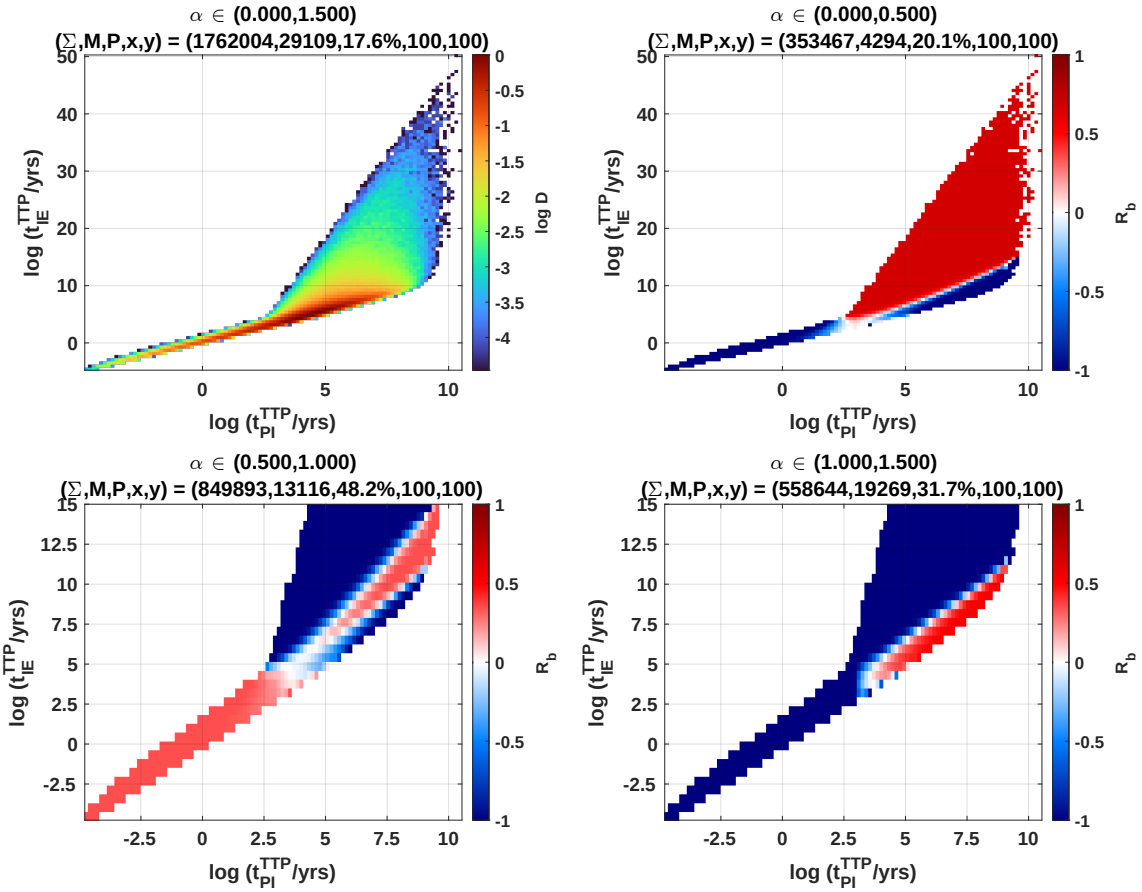

Figure 2.9: D&R Mapping of $(\mathcal{X}(\texttt{IR}) : t_{PI}, t_{IE}, \alpha)$, showing the radiative-to-intermediate and intermediate-to-adiabatic transition times for initially radiative outflows. The "wing" of large t_{IE} values in the top panels occurs for low α and low v_w, where both the bracketed term and exponent of Equation (2.54) are correspondingly high. For higher α (bottom panels), the transition to the adiabatic phase occurs more quickly for faster winds. See Appendix A for an explanation of D&R mapping (including Section A.1 for explanation of the numbers found in the subplot titles).

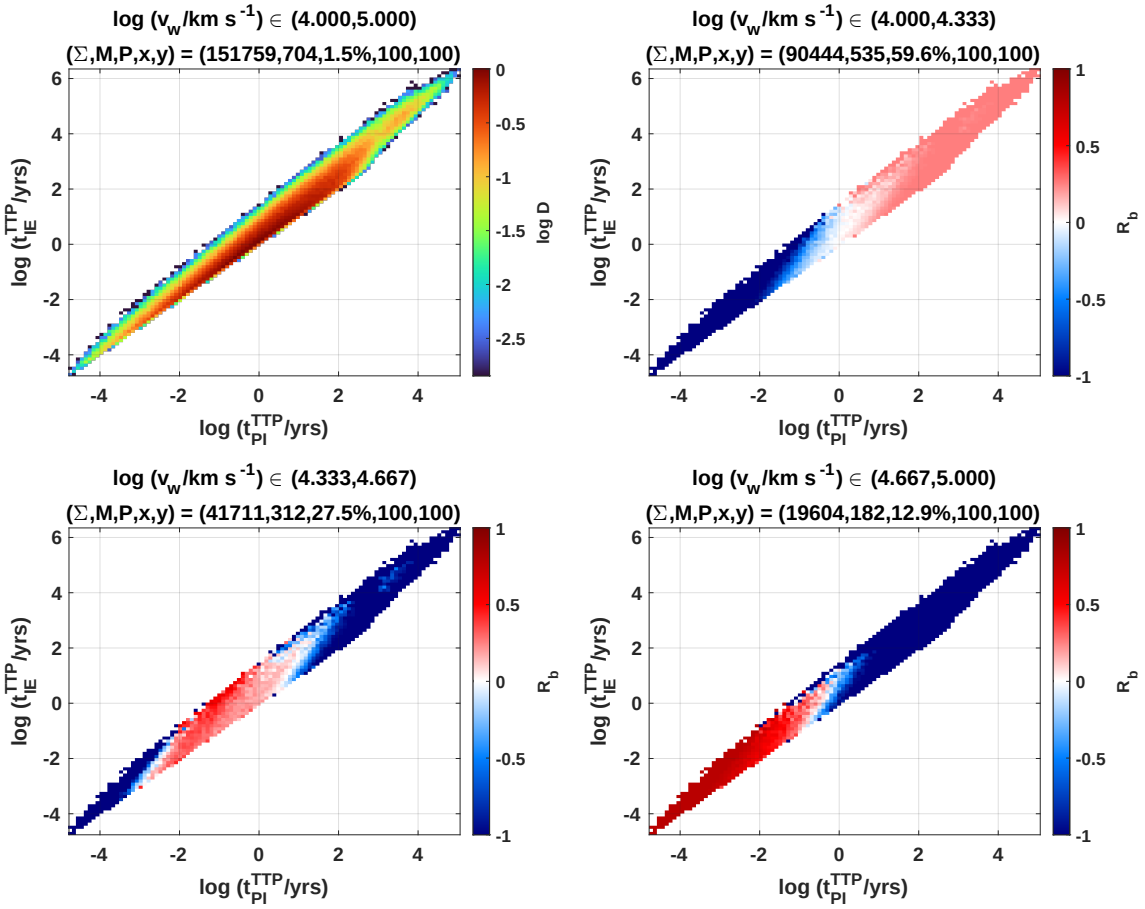

Figure 2.10: D&R Mapping of $(\mathcal{X}(\texttt{IR \& FAST}) : t_{PI}, t_{IE}, v_w)$, showing the radiative-to-intermediate and intermediate-to-adiabatic transition times for initially radiative outflows with wind velocities $v_w >$ 10,000 km s^{-1} (and where the density gradient is non-uniform, in accordance with Figure 2.9 above). We see that the intermediate phase, for high L_{AGN} and τ_w, can be at high as 10^6 years for wind velocities $\sim$ 10,000 km s^{-1} and $10^{4.5}$ years for wind velocities $\sim$ 20,000 km s^{-1}. See Appendix A for an explanation of D&R mapping (including Section A.1 for explanation of the numbers found in the subplot titles).

2.1.4 Energy & Momentum Coupling

Here we discuss the coupling of energy and momentum between the wind and the shocked ambient medium, denoted by $\mathcal{E}$ and $\mathcal{B}$ respectively. FGQ12 explored momentum coupling in the context of outflow "momentum boosts" (i.e. outflows where $\dot{P} \gg \dot{P}_{rad} = L_{AGN}/c$) observed in local ultra-luminous infrared galaxies (ULIRGs) and FeLoBAL quasars (see their Sections 1 and 3.5). They found that the observed momentum boosts were well

matched by those predicted for outflows with $\tau_w = 1$ and an energy coupling factor $\mathcal{E} = 1/2$ (see below). For consistency with FGQ12's analysis, we assume the thin shell approximation ($\gamma_{sa} = 1$) and consider the shell as a single unit of mass when calculating its kinetic luminosity and momentum flux (i.e., we exclude the jump condition factors which apply to the gas within the shell). We discuss the trends in $\mathcal{E}$ and $\mathcal{B}$ for the late-time phases, and show that the signs of intermediate phase time derivatives $\dot{\mathcal{E}}_I$ and $\dot{\mathcal{B}}_I$ correspond to the hierarchy of late-time β values (and in turn the steady phases/phase transition conditions) in a manner similar to the correspondence described in Section 2.1.3.4).

Integrating Equation (2.4) from $r = 0$ to $r = R_2$, the mass of the shocked ambient shell is

$$M_{sa} = \frac{4\pi\mu m_p n_0 R_0^\alpha}{3-\alpha} R_2^{3-\alpha}, \tag{2.56}$$

and its time derivative is

$$\dot{M}_{sa} = 4\pi\mu m_p n_0 R_0^\alpha R_2^{2-\alpha} v_{R2}. \tag{2.57}$$

The energy and momentum coupling factors $\mathcal{E}$ and $\mathcal{B}$ ($\mathcal{B}$ for momentum *boost*, e.g. FGQ12) are then defined by:

$$\begin{aligned} L_{sa} &= \mathcal{E} L_w \\ \dot{P}_{sa} &= \mathcal{B} \dot{P}_w, \end{aligned} \tag{2.58}$$

where the kinetic luminosities and momentum fluxes for the wind and shocked ambient region are given by:

$$\begin{aligned} L_{sa} \equiv \frac{1}{2}\dot{M}_{sa} v_{R2}^2 \quad \text{and} \quad L_w \equiv \frac{1}{2}\dot{M}_w v_w^2 \\ \dot{P}_{sa} \equiv \dot{M}_{sa} v_{R2} \quad \text{and} \quad \dot{P}_w \equiv \dot{M}_w v_w. \end{aligned} \tag{2.59}$$

Noting that Equation (2.11) can be written as $R_f^{2-\alpha} = [(3-\alpha)/3][\dot{M}_w/4\pi\mu m_p n_0 R_0^\alpha v_w]$,

one can easily show that $\dot{M}_{sa}/\dot{M}_w = [(3-\alpha)/3][R_2/R_f]^{2-\alpha}[v_{R2}/v_w]$; combining Equations (2.58) and (2.59) then yields:

$$\begin{aligned}\mathcal{E} &= \frac{3-\alpha}{3}\left(\frac{R_2}{R_f}\right)^{2-\alpha}\left(\frac{v_{R2}}{v_w}\right)^3 = \mathcal{B}\left(\frac{v_{R2}}{v_w}\right) \\ \mathcal{B} &= \frac{3-\alpha}{3}\left(\frac{R_2}{R_f}\right)^{2-\alpha}\left(\frac{v_{R2}}{v_w}\right)^2 = \mathcal{E}\left(\frac{v_w}{v_{R2}}\right).\end{aligned} \tag{2.60}$$

By applying Equation (2.13) to Equation (2.60) and taking the time derivative, one can show that the different late-time phases correspond to different regimes of $\dot{\mathcal{E}}$ and $\dot{\mathcal{B}}$; in particular, one can easily show by parsing Equation (2.60) that $\mathcal{E} \propto t^{3(\beta/\beta_E-1)}$ and $\mathcal{B} \propto t^{2(\beta/\beta_P-1)}$. Therefore the radiative phase has $\dot{\mathcal{E}}_P < 0$ and $\dot{\mathcal{B}}_P = 0$, the adiabatic phase has $\dot{\mathcal{E}}_E = 0$ and $\dot{\mathcal{B}}_E > 0$ for stable outflows, while $\dot{\mathcal{E}}_P > 0$ and $\dot{\mathcal{B}}_E < 0$ equivalently imply instability ($\beta_E < \beta_P$). The intermediate phase time derivatives $\dot{\mathcal{E}}_I$ and $\dot{\mathcal{B}}_I$ respectively follow sign patterns analogous to $(t_{c,sw})_I/t_{flow}$ and $(t_{c,sw})_I/t_{cr}$, as discussed in Section 2.1.3.4. Therefore, outflows with $\dot{\mathcal{E}}_I < 0$, $\dot{\mathcal{B}}_I < 0$ are steady in the radiative phase; those with $\dot{\mathcal{E}}_I < 0$, $\dot{\mathcal{B}}_I > 0$ are steady in intermediate phase; those with $\dot{\mathcal{E}}_I > 0$, $\dot{\mathcal{B}}_I > 0$ are steady in the adiabatic phase, and those with $\dot{\mathcal{E}}_I < 0$, $\dot{\mathcal{B}}_I > 0$ are unstable (this last case again implying $\beta_E < \beta_P$).

Of interest are the constant $\mathcal{E}_E$ and $\mathcal{B}_P$; one can parse the definitions in Equation (2.60) with the self-similarity variables in Section 2.1.2 to get the $\eta_{in} = 1$ expressions

$$\begin{aligned}\mathcal{E}_E &= \frac{3-\alpha}{3}2\pi\Gamma_{rad}\xi\beta_E^3 = \frac{18\pi(3-\alpha)\Gamma_{rad}\xi}{(5-\alpha)^3} \\ \mathcal{B}_P &= (3-\alpha)\beta_P = 2\frac{(3-\alpha)}{(4-\alpha)}.\end{aligned} \tag{2.61}$$

For $0 \leqslant \alpha \leqslant 1.5$ we have $\mathcal{E}_E \in (0.735, 0.781)$ (not a monotonic function of α) and $1.5 \geqslant \mathcal{B}_P \geqslant 1.2$. Since $\mathcal{B}_P$ is of order one, we have $\mathcal{E}_P = \mathcal{B}_P(v_{R2}/v_w) \approx 0$ for the radiative phase in the late-time limit $v_{R2} \ll v_w$. For the adiabatic phase, the relationship

$\mathcal{B}_E = \mathcal{E}_E(v_w/v_{R2})$ is analogous to FGQ12's result (in their Equation (37)). However, we note that FGQ12 approximate $\mathcal{E}_E = 1/2$, but use two different definitions: the definition implied by their Equation (37) matches our definition, but their Equation (A1) defines energy-driven (adiabatic) outflows by $\mathcal{E}'_E L_w t = (1/2) M_{sa} v_{R2}^2$. Parsing the latter definition gives $\mathcal{E}'_E = \mathcal{E}_E/(3-\alpha)\beta_E$, in which case $0.408 \leqslant \mathcal{E}'_E \leqslant 0.606$ for $0 \leqslant \alpha \leqslant 1.5$, in line with their value of 1/2. It is likely the case that $\mathcal{E}_E$ and $\mathcal{B}_P$ are respectively late-time upper and lower limits for $\mathcal{E}$ and $\mathcal{B}$, and thus offer another set of consistency checks, but we do not incorporate this into the generation of $\mathcal{X}$.

2.1.5 Remarks

Here we conclude this section on global dynamics, where we have defined for the self-similar model the various outflow phases, stability/initial phase/transition conditions, transition times and energy/momentum coupling parameters. We reiterate here the fact that the self-similarity condition assumes that the system is far from the boundaries of major transitions (e.g., t is far away from t_f, t_{PI}, t_{IE}), and that model parameter choices placing the system near said boundaries may yield pathological results.

Regarding TTP cooling, we note that, in addition to assuming a thin shell and purely thermal energy profile for the shocked wind, FGQ12 also assume a Compton temperature $T_X = 2 \cdot 10^7$ K (based on the results of Sazonov et al. 2004) and a shocked wind density profile according to an adiabatic outflow with $v_{R2} = 1000\ \mathrm{km\,s^{-1}}$. These assumptions are in general not consistent with the self-similarity assumption or the assumed AGN luminosity, but nonetheless provide a useful starting point for this type of cooling without overcomplicating the model; a proper extension is not in the scope of this work. In particular, a lower Compton temperature may imply that TTP cooling applies to the shocked ambient medium (discussed in the next section), but again, such an extension is beyond the scope of this work.

Finally, regarding unstable outflows, FGQ12 discuss the mixing of hot and cold gas in the shocked wind. They show that mixing is well-tolerated in adiabatic outflows, and it may be the case that this tolerance extends to unstable but short-lived intermediate-phase outflows, allowing them to transition to the adiabatic phase and stabilise.

2.2 Outflow Structure and Local/Regional Dynamics

This section discusses the structural details of the outflow, including the locations of the shocks, local gas properties/dynamics in the shocked wind/shocked ambient regions, and the cooling of the shocked ambient medium. For profiles of the various properties, aside from varying one parameter of interest we use the following fiducial set of parameters:

$$\begin{aligned} t &= 10^{3.5}\ \text{yr} \\ L_{AGN} &= 10^{46}\ \text{erg s}^{-1} \\ v_w &= 20,000\ \text{km s}^{-1} \\ \tau_w &= 1 \\ \alpha &= 0 \\ n_0 &= 100\ \text{cm}^{-3} \\ R_0 &= 100\ \text{pc}. \end{aligned} \tag{2.62}$$

When varying time, we ignore the shell formation time t_{sf} (see below), which, for free-free cooling and the fiducial parameters, is equal to $10^{4.0}$ years.

2.2.1 Shocked Ambient Cooling & Shell Formation

Like the shocked wind, the shocked ambient gas has a cooling time $t_{c,sa}$ and a set of associated phases, though these phases have no bearing on the self-similarity parameter β in Section 2.1.2. KM92 explore shocked ambient cooling in the CIE REF regime (appro-

priate for stellar winds); we extend this to free-free cooling, which is more appropriate for fast AGN winds. TTP cooling is also possible, but an extension of the TTP regime to the shocked ambient region is not in the scope of this work. We follow KM92 in using a simple two-phase model where the shocked ambient region is either radiative ($\gamma_{sa} = \lambda_c = 1$) or adiabatic ($\gamma_{sa} > 1$, $\lambda_c < 1$); the transition time between these phases, t_{sf}, is called the *shell formation time* and is defined by

$$\frac{t_{c,sa}(t_{sf})}{t_{sf}} = 1. \tag{2.63}$$

The name "shell formation time" implicitly assumes that $t_{c,sa}/t$ decreases over time, meaning the (initially adiabatic) shocked ambient region of an initially adiabatic outflow will eventually collapse into a thin shell, with $\gamma_{sa} = \lambda_c = 1$ at times $t \gg t_{sf}$. This is usually, but not necessarily the case; as we shall see, $t_{c,sa}/t$ increases over time for α values above a high threshold. TTP cooling may lower this threshold.

The cooling time $t_{c,sa}^{REF}$ is derived in a manner analogous to that of the shocked wind, and is given by

$$\begin{aligned} t_{c,sa}^{REF} &\equiv \frac{x_t k T_{post}}{n_{post}\Lambda(T_{post})} \\ &= \left[\left(\frac{3m_p}{2^6}\right)\frac{\mu^{1-\eta}}{\Lambda_0(T_{REF}/c^2)^\eta n_0 R_0^\alpha}\right] R_2^\alpha v_{R2}^{2-2\eta} \quad \text{(for } \Lambda(T) = \Lambda_0 T^\eta \text{ and } \gamma_{sa} = 5/3\text{)} \end{aligned} \tag{2.64}$$

where we've substituted $n_{post} = 4n_a(R_2) = 4n_0 R_0^\alpha R_2^{-\alpha}$ and $(3/2)x_t k T_{post} = (9/32)\mu m_p v_{R2}^2$ for the case of $\gamma_{sa} = 5/3$. The definition of T_{REF} in Equation (2.33) gives us $T_{post} = \mu(v_{R2}^2/c^2)T_{REF}$. If we use the $\gamma_{sa} = 5/3$ expression in Equation (2.64) for initially radiative outflows (as is done with the shocked wind), we can see that $t_{c,sa}^{REF}(t_f) = f_P(t_f)t_{c,sw}^{REF}(t_f) \approx t_{c,sw}^{REF}(t_f)$, and thus the shocked ambient region begins in the same initial phase as the

overall outflow. This might allow for a radiative shocked ambient region to become adiabatic, but as mentioned in Section 2.1.2 we simply assume the shocked ambient radiation remains radiative for initially radiative outflows. Using Equation (2.13) we obtain

$$\frac{t_{c,sa}^{REF}}{t} = \left[\left(\frac{3m_p}{2^6}\right)\frac{\mu^{1-\eta}\beta^{2-2\eta}A^{\alpha+2-2\eta}}{\Lambda_0(T_{REF}/c^2)^{\eta}n_0R_0^{\alpha}}\right]t^{\beta(\alpha+2-2\eta)-2+2\eta}. \tag{2.65}$$

Setting the left hand side to 1, setting $t = t_{sf}$ and using the appropriate cooling regime parameters in Equation (2.34), we can solve for t_{sf}, giving us:

$$t_{sf}^{CIE} = \left[\left(\frac{3m_p}{2^6}\right)\frac{\mu^{3/2}(T_{REF}/c^2)^{1/2}\beta^3A^{\alpha+3}}{\Lambda_0^{CIE}n_0R_0^{\alpha}}\right]^{1/[4-\beta(\alpha+3)]} \tag{2.66}$$

and

$$t_{sf}^{FF} = \left[\left(\frac{3m_p}{2^6}\right)\frac{\mu^{1/2}\beta A^{\alpha+1}}{\Lambda_0^{FF}(T_{REF}/c^2)^{1/2}n_0R_0^{\alpha}}\right]^{1/[2-\beta(\alpha+1)]}. \tag{2.67}$$

The exponents of Equations (2.66) and (2.67) give rise to stationary points which depend on the phase (i.e., the value of β); these are given by:

$$\begin{aligned} &\alpha_{sf,P}^{CIE} = 5/3 = 1.\bar{6}; \quad \alpha_{sf,I}^{CIE} = 1; \quad \alpha_{sf,E}^{CIE} = 11/7 \approx 1.57; \\ &\alpha_{sf,P}^{FF} = 3/2 = 1.5; \quad \alpha_{sf,I}^{FF} = 1; \quad \alpha_{sf,E}^{FF} = 7/5 = 1.4. \end{aligned} \tag{2.68}$$

At α values below these stationary points, the adiabatic shocked ISM region becomes radiative and begins to collapse at t_{sf}, while for values above the stationary points, the radiative shocked ISM region becomes adiabatic and begins to expand; in the case where α is equal to the stationary points, the shocked ambient phase does not change over time. For radiative outflows, both stationary points are at or beyond the upper limit of our sampling range $\alpha \in (0, 1.5)$, while for intermediate-phase outflows governed by TTP cooling, both stationary points also correspond to the threshold for instability. For adiabatic outflows, the CIE cooling stationary point is beyond our sampling range, while

for free-free cooling we note that all outflows in our sampling regime where $\alpha > 1.4$ are initially adiabatic, and thus their shocked ISM regions will remain adiabatic throughout their lifetimes. Figure 2.11 shows the D&R Mapping of $(\mathcal{X}(\texttt{IA}) : \alpha, t_{sf}^{FF}, L_{AGN})$, giving the distribution of shell formation times for initially adiabatic outflows; we empirically find that, searching over multiple potential band parameters, lower t_{sf} are most consistently found in outflows with lower L_{AGN} and vice-versa, as shown by the clear trends in Figure 2.11).

Due to the potential effects of TTP cooling to lower the stationary points discussed above and/or increase the shell formation time, we flag, but otherwise disregard, cases where $t > t_{sf}^{FF}$ when analysing trends with respect to time. For the fiducial parameters in Equation (2.62), we find $t_{sf}^{FF} = 10^{4.0}$ years.

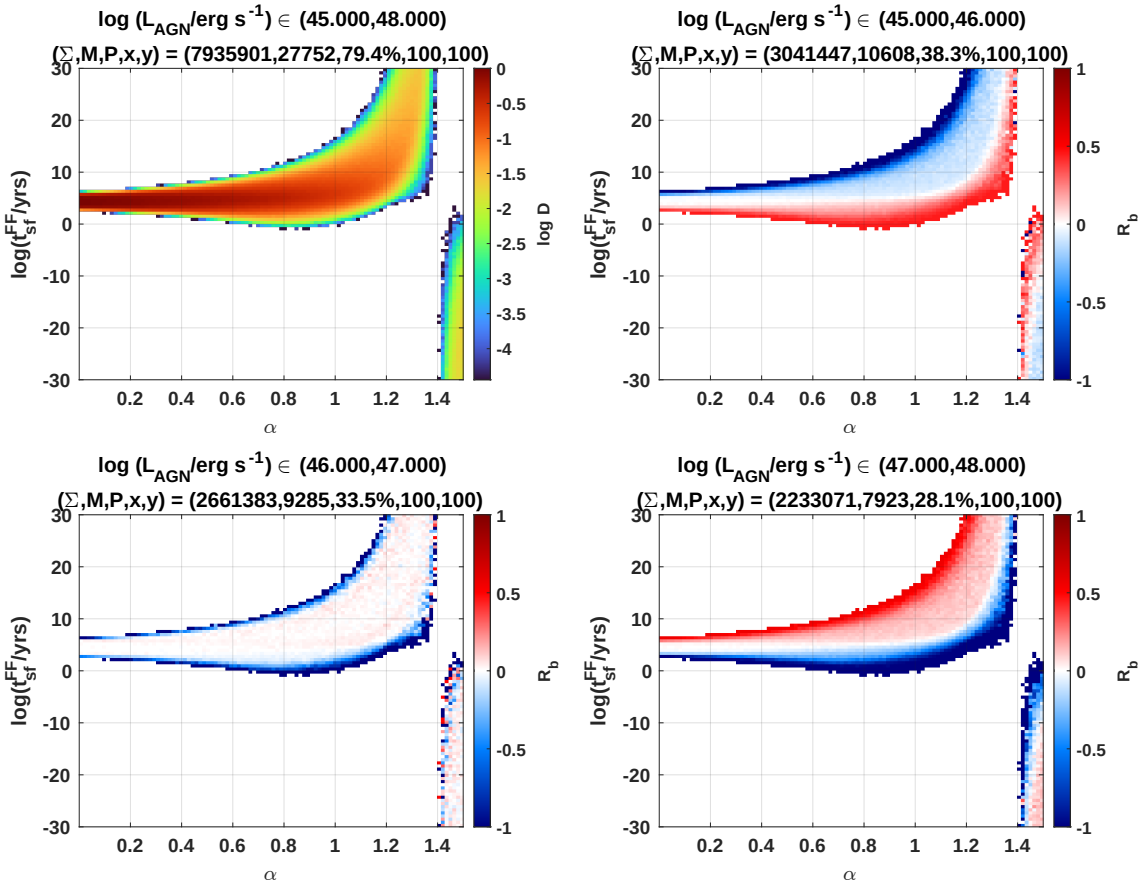

Figure 2.11: D&R Mapping of $(\mathcal{X}(\texttt{IA}) : \alpha, t_{sf}^{FF}, L_{AGN})$ showing the trends in the free-free cooling shell formation time t_{sf}^{FF} for initially adiabatic outflows in accordance with Equation (2.67), with respect to L_{AGN} and limited to $|\log t_{sf}^{FF}| < 30$ to avoid asymptotic effects at the critical $\alpha_{sf,E}^{FF} = 1.4$ (in which the shocked ambient region does not change phase over time). We see that higher luminosities yield higher shell formation times. See Appendix A for an explanation of D&R mapping (including Section A.1 for explanation of the numbers found in the subplot titles).

2.2.2 Shock Features

2.2.2.1 Outer Shock and Contact Discontinuity

The outer shock is located at $R_2 = At^\beta$ by the self-similarity assumption, from which the time derivatives v_{R2} and a_{R2} are easily obtained, and with self-similarity parameters β and A for the various phases as derived in Section 2.1.2. By definition the contact discontinuity is given by $R_c = \lambda_c R_2$, with λ_c given in Equation (2.15). Since λ_c is independent of time,

we have $v_{Rc} = \lambda_c v_{R2}$ and $a_{Rc} = \lambda_c a_{R2}$. For initially radiative outflows (i.e. outflows with a radiative shocked ambient region) we have $\lambda_c = 1$, while for initially adiabatic outflows prior to shell formation (outflows with an adiabatic shocked ambient region), substituting $\beta = \beta_E = 3/(5-\alpha)$ and $\gamma_{sa} = 5/3$ into Equation (2.15) gives us

$$\lambda_{c,E} = \frac{123 - 8\alpha}{143 - 8\alpha} \quad (\text{for } \gamma_{sa} = 5/3 \quad \text{and } t < t_{sf}). \tag{2.69}$$

Since the adiabatic self-similarity parameter A_E depends on $\Gamma_{rad}\xi$, which depends on both γ_{sa} and λ_c, we note that where Equation (2.69) applies, $\gamma_{sw} = 5/3$ and $0 \leqslant \alpha \leqslant 1.5$ yields $0.860 > \lambda_{c,E} > 0.847$ and $0.541 > \Gamma_{rad}\xi > 0.394$; if the shocked ambient region is radiative in the adiabatic phase (i.e. $\gamma_{sa} = \lambda_{c,E} = 1$) we have $0.259 > \Gamma_{rad}\xi > 0.180$.

2.2.2.2 Inner Shock

To determine the inner shock location R_1, we consider the various outflow phases. As discussed in Section 2.1.2, $\gamma_{sw} \approx 1$ for radiative outflows, and thus

$$R_1 \approx R_c = \lambda_c R_2 \quad (\text{for radiative outflows}). \tag{2.70}$$

Since $\lambda_c = 1$ for radiative outflows (the radiative phase must also be the initial phase), R_1 and R_2 coincide, as do their time derivatives.

For the intermediate phase we can determine R_1 directly from the definition of f_P in Equation (2.24); in the late-time limit $v_w \gg v_{R1}$, we use the analytic approximation of f_P and Equation (2.10) to obtain

$$R_1 = \left[\frac{3}{(3-\alpha)f_P}\right]^{1/2} R_f \left(\frac{R_2}{R_f}\right)^{\alpha/2} \left(\frac{v_{R2}}{v_w}\right)^{-1} \quad (\text{for intermediate-phase outflows}). \tag{2.71}$$

Enforcing $R_1 < R_2$ amounts to another consistency check for intermediate-phase and

adiabatic outflows; this is built into the `PASS` filter described in Table 2.2. The check rejects approximately 27% of outflows in $\mathcal{X}$ that otherwise qualify as intermediate-phase under our sampling scheme (initially radiative and stable with $t_f < t_{PI} < t < t_{IE}$), likely due to crude assumptions involved in deriving the self-similarity parameters (such as a sufficiently long prior radiative phase so that $R_c \gg R_1$). All of these pathological cases have $\alpha < 1$ and virtually all ($> 99\%$) have $v_w < 10,000$ km s^{-1} (though we find a maximum $v_w \sim 15,000$ km s^{-1}). Taking the time derivatives and simplifying yields

$$v_{R1} = \left[1 - \frac{\beta_I(2-\alpha)}{2}\right]\frac{R_1}{t} \quad \text{(for intermediate-phase outflows)} \tag{2.72}$$

and

$$a_{R1} = -\left[\frac{\beta_I(2-\alpha)}{2}\right]\frac{v_{R1}}{t} \quad \text{(for intermediate-phase outflows).} \tag{2.73}$$

For adiabatic outflows, Equations (2.71) through (2.73) are valid for late times $t \gg t_f$; however, using mass conservation for the shocked wind, KM92 derive an expression for R_1 in the adiabatic phase (which we adopt here) that is valid for both initially radiative and initially adiabatic outflows, at both late times and early times where $t \ll t_f$ (see their Section 5.1). The expression is

$$R_1 = \frac{\lambda_{c0} R_2}{[1 + \Upsilon(R_2/R_f)^{(1-\alpha/2)}]^{1/3}} \quad \text{(for adiabatic outflows)} \tag{2.74}$$

where

$$\begin{aligned} \lambda_{c0} &\equiv \left(\frac{R_c}{R_2}\right)_{t \ll t_f} = \lambda_c(\beta = 1) \\ &\approx \frac{215 - 54\alpha}{235 - 54\alpha} \quad (\text{for } \gamma_{sa} = 5/3), \end{aligned} \tag{2.75}$$

is the free expansion expression for λ_c, and

$$\Upsilon \equiv \beta_E^3 \lambda_{c0}^3 (2\pi\Gamma_{rad}\xi) \left[\frac{(3-\alpha)}{3} f_P\right]^{3/2}. \tag{2.76}$$

In the denominator of Equation (2.74), the unity term on the left accounts for early times while the Υ term on the right accounts for late times. With this expression we find no inconsistencies in $\mathcal{X}$ when enforcing $R_1 < R_2$. In the range $0 \leqslant \alpha \leqslant 1.5$, we have $0.303 > \Upsilon > 0.239$ and $0.915 > \lambda_{c0} > 0.870$. Taking the time derivatives of R_1, we obtain

$$v_{R1} = \beta_E \left[1 - \Psi\right] \frac{R_1}{t} \quad \text{(for adiabatic outflows)} \tag{2.77}$$

and

$$a_{R1} = \left[\beta_E \left(\frac{4\Psi^2 - (3-\alpha/2)\Psi + 1}{1-\Psi}\right) - 1\right] \frac{v_{R1}}{t} \quad \text{(for adiabatic outflows)}, \tag{2.78}$$

where for convenience we have defined

$$\Psi \equiv \frac{1}{3}\frac{2-\alpha}{2}\frac{\Upsilon(R_2/R_f)^{1-\alpha/2}}{1+\Upsilon(R_2/R_f)^{1-\alpha/2}}; \tag{2.79}$$

because $\alpha \in (0, 1.5)$, one can show that $\Psi < 1/3$ and thus $a_{R1} < 0$.

Figure 2.12 below shows the location of the shock features as a function of time for the fiducial parameters in Equation (2.62).

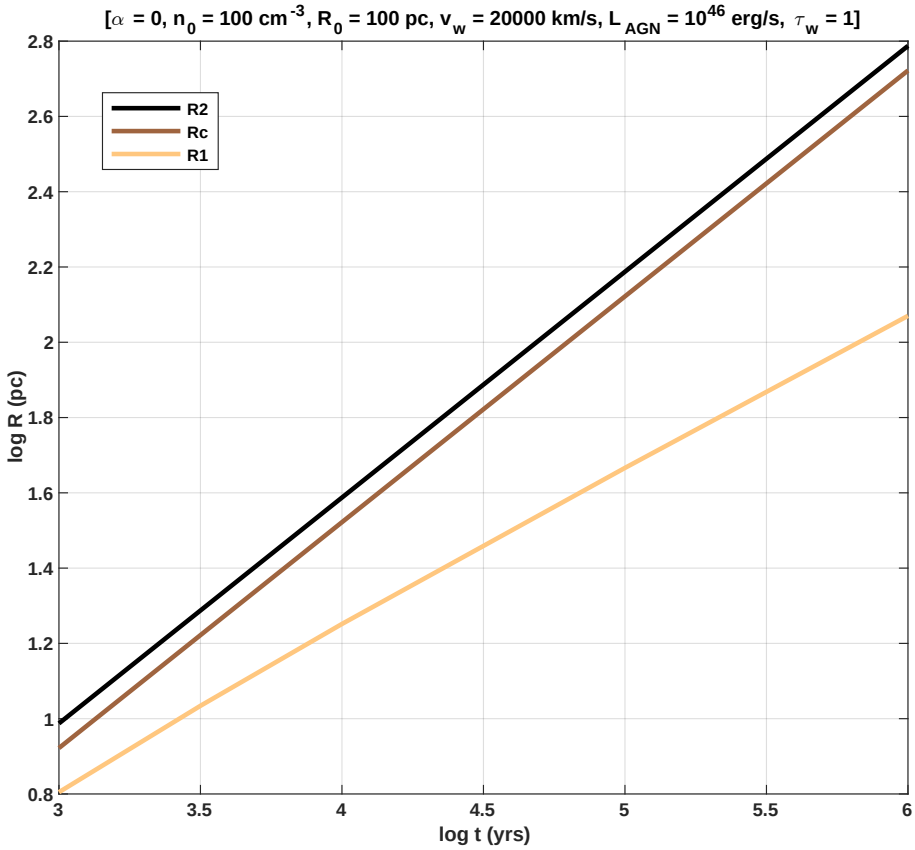

Figure 2.12: Radii of the different shock features (relative to the AGN) as a function of time, for the fiducial parameters in Equation (2.62) and ignoring the corresponding shell formation time $t_{sf}^{FF} \approx 10^{4.0}$ yr, when the shocked ISM region will begin to collapse and $R_c(t)$ and $R_2(t)$ will converge to the same value (Section 2.2.1).

2.2.3 Regional Gas Observables

This section gives the profiles for various observable gas properties (velocity, density, etc.) within the regions of freely expanding wind, shocked wind and shocked ambient gas. Given our range of α considered, the freely expanding wind at $r < R_2$ is the only region for the radiative phase where $\gamma_{sa} = \gamma_{sw} = 1$. For initially radiative outflows in the intermediate or adiabatic phase where $\gamma_{sa} = 1$, we have the freely expanding wind and (hot) shocked wind regions to consider. For initially adiabatic outflows prior to shell formation, we have freely expanding wind, shocked wind and shocked ambient gas.

For the analysis of the shocked wind, we follow the method of W77 and KM92 but note that this breaks down for KM92's approximation of the intermediate phase. Extending the model to include the intermediate phase is not in the scope of this work, and so we restrict our analysis of the region to the adiabatic phase. To briefly describe the problem, it is assumed that the hot shocked wind is nearly isobaric far from R_1 due to the high speed $\sim v_w$ of the wind shock. One then obtains the velocity profile $v(r,t)$ for the region by integrating the continuity equation; enforcing the jump condition at R_1 yields the result $R_1^{-2} \propto t/R_c^3 \propto t^{1-3\beta}$ (e.g., KM92's Equation (B16)), but then one can also show that $R_1^{-2} \propto t^{\beta(2-\alpha)-2}$ by combining Equations (2.10), (2.13) and (2.26). Equating the time dependencies yields $\beta = 3/(5-\alpha) = \beta_E$, and thus the method is only consistent for the adiabatic phase. The dependency $R_1^{-2} \propto t^{\beta(2-\alpha)-2}$ results from assuming that the pressure at the contact discontinuity is roughly equal to the mean pressure ($p(R_c) \approx \bar{p}_{sw}$) in the region $R_1 \ll r \leqslant R_c$; this is reasonable for the adiabatic phase where none of the shocked wind has effectively cooled, but is likely too simplistic for the intermediate phase where the gas is cooling faster than the flow timescale.

2.2.3.1 Velocity

The equations for the gas velocity $v_{gas}(r,t)$ in the various regions are as follows (explained below):

$$\begin{aligned}
v_{gas}(r < R_1) &= v_w \\
v_{gas}(r = R_1) &= (1 - K_{v,sw})v_w + K_{v,sw}v_{R1} \\
v_{gas}(R_1 < r < R_c) &= -\frac{\phi_E}{3\gamma_{sw}}\frac{r}{t} + \frac{R_c^3}{r^2 t}\left[\beta_E + \frac{\phi_E}{3\gamma_{sw}}\right] \\
v_{gas}(r = R_c) &= v_{Rc} \\
v_{gas}(R_c < r < R_2) &= \left[C_{v0} + 2C_{v1}\frac{r}{R_2} + C_{v2}\frac{r^2}{R_2^2}\right] K_{v,sa}v_{R2} \\
v_{gas}(r = R_2) &= K_{v,sa}v_{R2} \\
v_{gas}(r > R_2) &= 0,
\end{aligned} \tag{2.80}$$

where

$$\begin{aligned}
K_v &\equiv \frac{2}{\gamma + 1} \\
&= 3/4 \quad (\text{for } \gamma = 5/3)
\end{aligned} \tag{2.81}$$

represents the shock jump condition for the velocity,

$$\phi_E \equiv 1 - 3\beta_E = -\frac{4 + \alpha}{5 - \alpha} \tag{2.82}$$

represents the adiabatic phase pressure relation $p \propto E_{sw}/V_{sw} \propto t^{\eta_{in}-3\beta} = t^{1-3\beta}$ and

$$
\begin{aligned}
C_{v0} &\equiv 1 - \frac{v_{\nabla c} + (1-2\lambda_c)v_{\nabla 2}}{2(1-\lambda_c)} \\
&= \frac{90(1-\lambda_c) + (33-8\alpha)}{60(1-\lambda_c)} \quad \text{(for } \beta = \beta_E \text{ and } \gamma_{sa} = 5/3\text{)} \\
C_{v1} &\equiv \frac{v_{\nabla c} - \lambda_c v_{\nabla 2}}{2(1-\lambda_c)} \\
&= -\left[\frac{15(1-\lambda_c) + (33-8\alpha)}{60(1-\lambda_c)}\right] \quad \text{(for } \beta = \beta_E \text{ and } \gamma_{sa} = 5/3\text{)} \\
C_{v2} &\equiv \frac{v_{\nabla 2} - v_{\nabla c}}{2(1-\lambda_c)} \\
&= \frac{33-8\alpha}{60(1-\lambda_c)} \quad \text{(for } \beta = \beta_E \text{ and } \gamma_{sa} = 5/3\text{)}
\end{aligned}
\tag{2.83}
$$

are parabolic approximation coefficients, with $v_{\nabla 2}$ and $v_{\nabla c}$ being the exact dimensionless velocity gradients at R_2 and R_c (KM92's Equations B7a and B7b):

$$
\begin{aligned}
v_{\nabla 2} &= \frac{-(7\gamma_{sa}+3) + \alpha + 3/\beta}{\gamma_{sa}+1} \\
&= -1/2 \quad \text{(for } \beta = \beta_E \text{ and } \gamma_{sa} = 5/3\text{)} \\
v_{\nabla c} &= \frac{-2(\gamma_{sa}+1) + \alpha + 2/\beta}{2\gamma_{sa}/(\gamma_{sa}+1)} \\
&= -\left[\frac{4(6-\alpha)}{15}\right] \quad \text{(for } \beta = \beta_E \text{ and } \gamma_{sa} = 5/3\text{).}
\end{aligned}
\tag{2.84}
$$

Figure 2.13 below shows the velocity profile for various times as a function of radius, for the fiducial parameters in Equation (2.62).

For the freely expanding wind the gas velocity is v_w by assumption. For the shock features, $v_{gas}(r = R_1)$ and $v_{gas}(r = R_2)$ are the post-shock velocities in the quasar rest

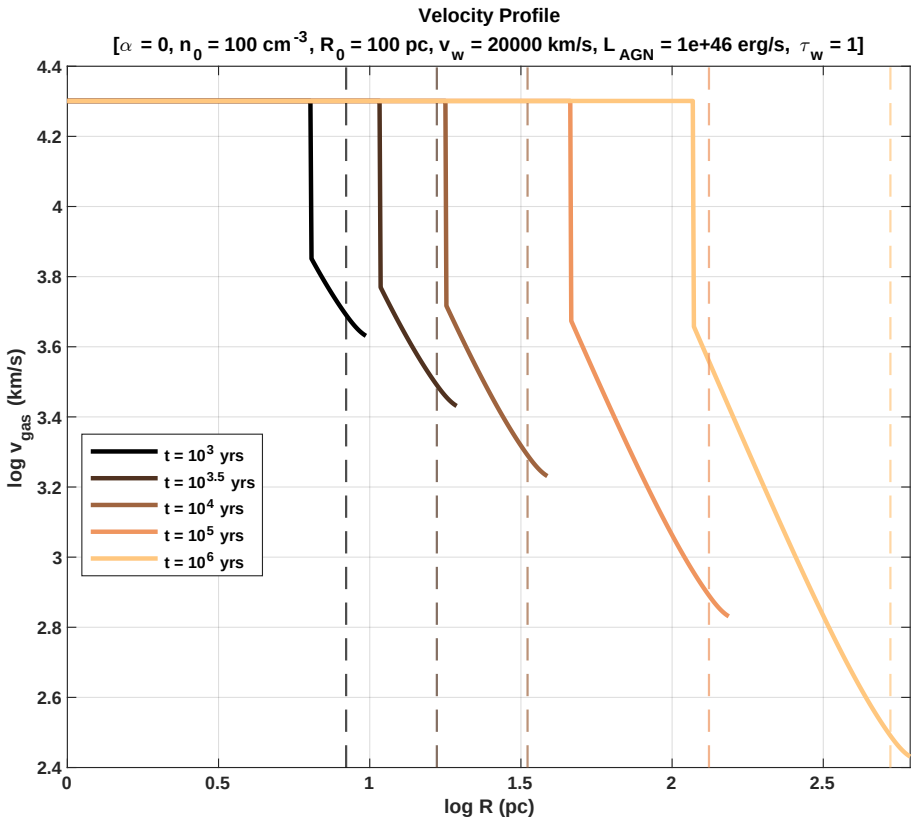

Figure 2.13: Gas velocity vs. distance from the AGN for varying times and fiducial parameters in Equation (2.62), with the dashed lines indicating the contact discontinuity R_c for each profile and the abrupt change in velocity (solid vertical lines) indicating the jump discontinuity in velocity as the wind crosses R_1. We note the shell formation time $t_{sf}^{FF} \approx 10^{4.0}$ years, as mentioned in Section 2.2.1.

frame (given by the jump conditions), while $v_{gas}(r = R_c)$ comes from the self-similarity assumption.

For the shocked wind in the adiabatic phase, as mentioned above we follow W77 and KM92 in integrating the continuity equation

$$\nabla \cdot \mathbf{v} = -\frac{d \ln \rho}{dt} = -\frac{1}{\nu}\frac{d \ln p}{dt} = \frac{-\phi}{\nu t} \tag{2.85}$$

(assuming a polytropic process with pressure $p \propto \rho^{\nu} \propto t^{\phi}$), using $\phi = \phi_E$ and the isentropic $\nu = \gamma_{sw} = 5/3$ for the region far from the inner shock.

For the shocked ambient gas, we use a parabolic approximation of the self-similar velocity profile obtained from the hydrodynamic equations, with the coefficients in Equation (2.84) determined by the boundary conditions for the velocity and its gradient (KM92 Section B1). As noted by KM92, the profile is nearly linear for $\gamma_{sa} = 5/3$ and $\alpha \in [0, 2]$ (see their Figure 4b), but as will be shown in the next section, the assumption of a constant gradient in the region results in a poor approximation of the self-similar acceleration profile. For simplicity we use the expression for λ_c in Equation (2.15) in order to determine the parabolic approximation coefficients; this expression comes from the linear velocity profile approximation, but we find this has little impact on the accuracy of the approximation.

Finally, the ambient gas is stationary ($v_{gas}(r > R_2) = 0$) by assumption.

2.2.3.2 Acceleration

For the gas acceleration $a_{gas}(r,t) = dv_{gas}/dt$, we take the time derivative of the velocity equations above, giving us the following gas acceleration equations:

$$\begin{aligned}
a_{gas}(r < R_1) &= 0 \\
a_{gas}(r = R_1) &= K_{v,sw} a_{R1} \\
a_{gas}(R_1 < r < R_c) &= \frac{\beta_E \phi_E}{\gamma_{sw}} \frac{r}{t^2} - \left[2\frac{R_c^3}{r^3} \left(\beta_E + \frac{\phi_E}{3\gamma_{sw}} \right) + \left(1 - 3\beta_E + \frac{\phi_E}{3\gamma_{sw}} \right) \right] \frac{v_{gas}}{t} \\
a_{gas}(r = R_c) &= a_{Rc} \\
a_{gas}(R_c < r < R_2) &= \left[\frac{v_{gas}}{K_{v,sa} v_{R2}} + \frac{2\beta}{1-\beta} \left(\frac{v_{gas}}{v_{R2}} - \frac{r}{R_2} \right) \left(C_{v1} + C_{v2} \frac{r}{R_2} \right) \right] K_{v,sa} a_{R2} \\
a_{gas}(r = R_2) &= \left[1 + \frac{\beta}{1-\beta} (1 - K_{v,sa}) v_{\nabla 2} \right] K_{v,sa} a_{R2} \\
a_{gas}(r > R_2) &= 0.
\end{aligned} \tag{2.86}$$

We note for the reader that the expressions for the shocked wind and shocked ambient regions are not easily derived from the usual definition of the derivative ($da/dt = v\partial_r v + \partial_t v$, where ∂_x represents the partial derivative with respect to x): for the shocked wind, one can more easily recover the above equation by instead applying $da/dt = v\partial_r v + v_{R2}\partial_{R2} v + \partial_t v$ and expressing v_{R2} in terms of v_{gas}. For the shocked ambient region, we use the chain rule $d\tilde{v}/dt = (\partial_\lambda \tilde{v})(d\lambda/dt)$, where $\lambda \equiv r/R_2$ and $\tilde{v} \equiv v_{gas}/K_{v,sa} v_{R2}$ are the dimensionless gas position and velocity parameters defined in KM92. Figure 2.14 below shows the deceleration curves with varying time, for the fiducial parameters in Equation (2.62).

Figure 2.15 below shows the true self-similar acceleration profile $\tilde{a}(\lambda) \equiv a_{gas}/K_{v,sa} a_{R2}$ given by the hydrodynamic equations for the case of $\alpha = 4/3$, along with comparisons to the profiles derived from approximating the velocity profile as linear ($\tilde{a}_{lin}$) or parabolic ($\tilde{a}_{para}$). We see that $\tilde{a}_{lin}$ underestimates $\tilde{a}$ to a progressively higher degree as we approach the outer shock at $\lambda = 1$, where $\tilde{a}_{lin} \approx 0$, while $\tilde{a}_{para}$ is much more consistent with the

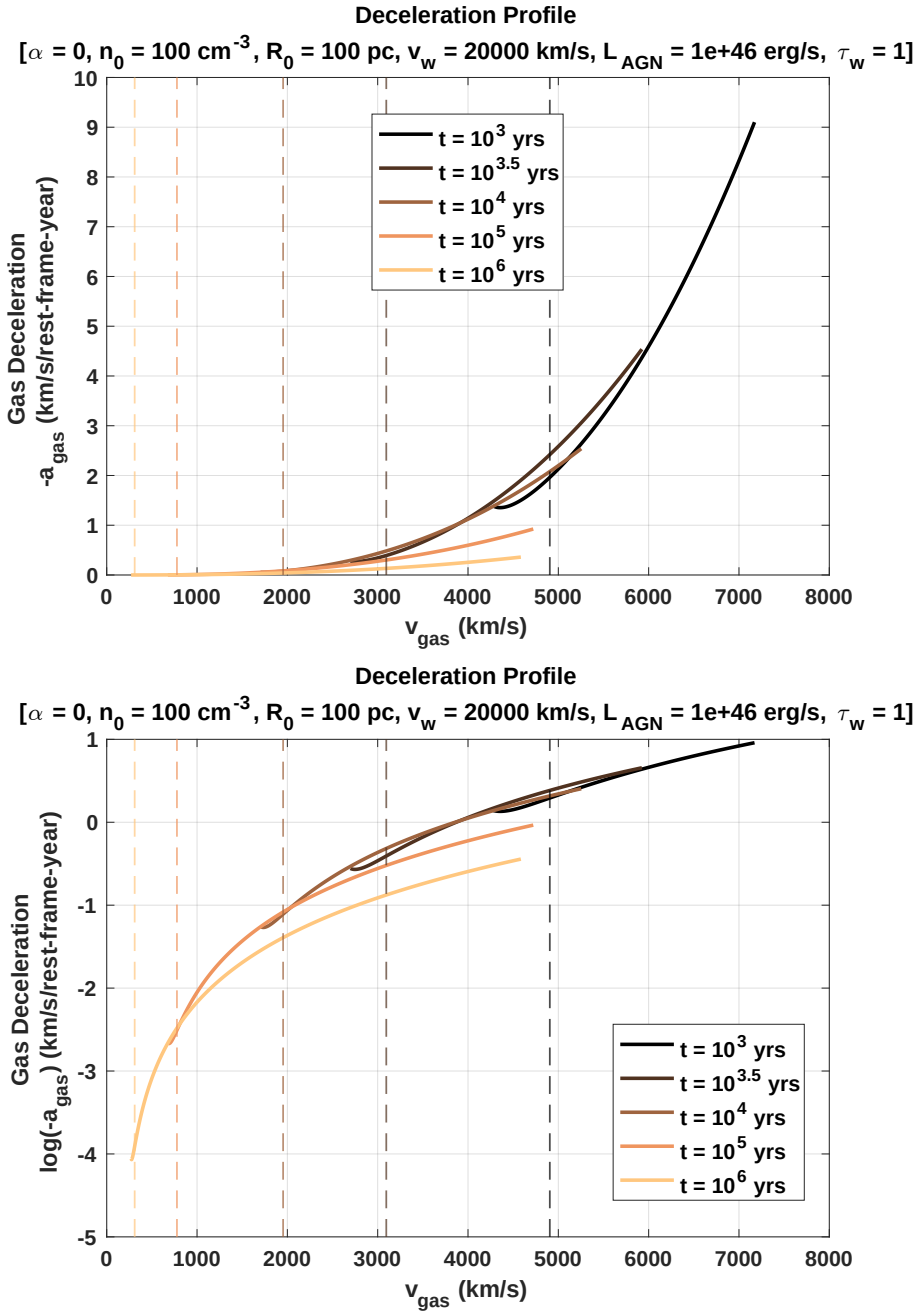

Figure 2.14: Gas deceleration (decrease in velocity per rest-frame year) vs. velocity for varying times and fiducial parameters in Equation (2.62), with the dashed lines indicating the contact discontinuity R_c for each profile. Shown in linear scale (top panel) and log scale (bottom panel). We see that the largest deceleration occurs in the youngest outflow. We note the shell formation time $t_{sf}^{FF} \approx 10^{4.0}$ years, as mentioned in Section 2.2.1.

true profile, matching at the boundaries and only slightly underestimating the profile in between. One can show that for $\beta = \beta_E$ and $\gamma_{sa} = 5/3$ the (true) immediate post-shock acceleration $a_{gas}(R_2)$ is

$$a_{post} = \frac{3}{4}\left[\frac{13 - 8\alpha}{8(2-\alpha)}\right] a_{R2}, \tag{2.87}$$

which is positive for $\alpha > 1.625$, and we find that all gas in the region decelerates below this threshold; the threshold is lower ($\alpha = 97/72 \approx 1.347$) if using the linear velocity approximation (which overestimates the true velocity gradient at R_2), but is not affected by the parabolic approximation (which matches the true velocity gradient at R_2). We find empirically that the true gradient of $\tilde{a}$ is purely negative at $\alpha \geqslant 1.625$, and thus in these cases a_{post} is the minimum deceleration. For $\alpha < 1.625$ the gradient becomes positive at some point near R_2, meaning a_{post} is not the minimum deceleration, but we find a_{post} only deviates from the true minimum by only 1.7% at $\alpha = 0$, down to 0.03% at $\alpha = 1.5$. Since $\tilde{a}_{para}$ underestimates $\tilde{a}$, we would find $\tilde{a}_{para} < 0$ in the region for α values slightly below 1.625, but find that this does not occur for $\alpha \leqslant 1.5$.

2.2.3.3 Density

Reminding the reader that $\dot{M}_w = \tau_w L_{AGN}/v_w c$ and $K_\rho \equiv (1+\gamma)/(1-\gamma)$, the equations for the gas number density $n_{gas}(r,t)$ (and mass density $\rho_{gas}(r,t)$, via the factor μm_p) are

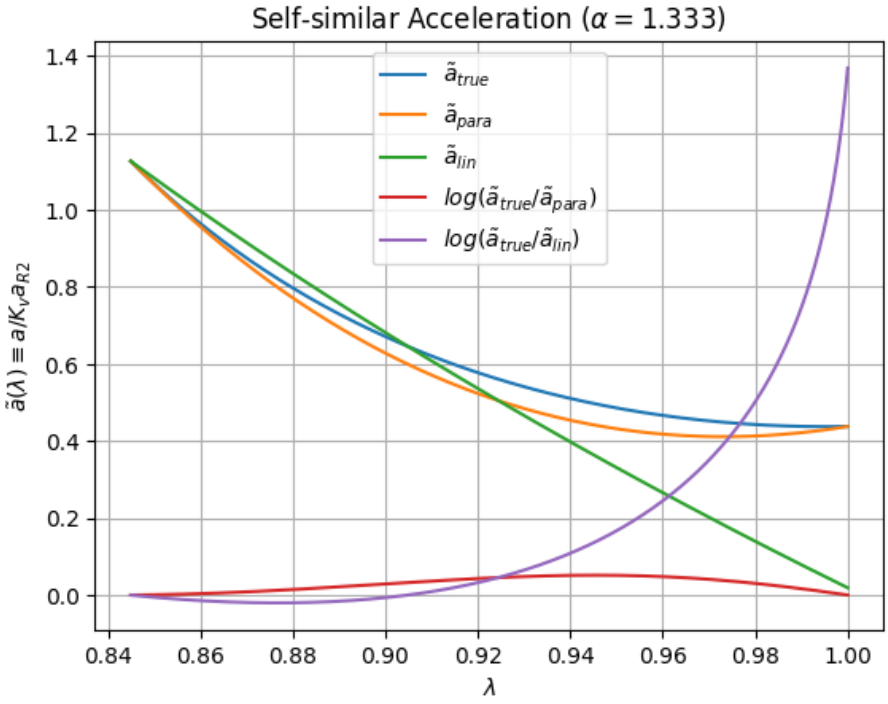

Figure 2.15: The self-similar acceleration profile $\tilde{a} \equiv a_{gas}/K_{v,sa}a_{R2}$ for the adiabatic phase ($\beta = \beta_E$) with $\gamma_{sa} = 5/3$ and $\alpha = 4/3$. The blue curve shows the true profile from the hydrodynamic equations, while the orange and green curves show the profiles resulting from the assumption of a parabolic or linear velocity profile. The red and purple curves show the log of the ratio between the true and approximate values, which can be thought of as a multiplicative correction factor.

(with explanations below):

$$
\begin{aligned}
n_{gas}(r < R_1) &= \frac{\dot{M}_w}{4\pi\mu m_p r^2 v_w} \\
n_{gas}(r = R_1) &= \frac{K_\rho \dot{M}_w}{4\pi\mu m_p R_1^2 v_w} \\
n_{gas}(R_1 < r < R_c) &= \left[\beta_E + \frac{\phi_E}{3\gamma_{sw}}\right]^{-1} \left[1 - \frac{r^3}{R_c^3(t)}\right]^{-\frac{2(4+\alpha)}{3(11-\alpha)}} \frac{\dot{M}_w t}{4\pi\mu m_p R_c^3} \\
n_{gas}(r = R_c) &= j_c n_0 (R_2/R_0)^{-\alpha} \\
n_{gas}(R_c < r < R_2) &= \left[\frac{\lambda_c}{1-\lambda_c} J_c \left(\frac{r}{R_c} - 1\right) + 1\right] n_{gas}(R_c) \\
n_{gas}(r = R_2) &= K_\rho n_0 (R_2/R_0)^{-\alpha} \\
n_{gas}(r > R_2) &= n_0 (r/R_0)^{-\alpha},
\end{aligned}
\tag{2.88}
$$

where

$$
j_c \equiv 1.60 + 2.04\alpha^2 \tag{2.89}
$$

and

$$
\begin{aligned}
J_c &\equiv \frac{K_{v,sa} - j_c}{j_c} \\
&= \frac{4 - j_c}{j_c} \quad (\text{for } \gamma_{sa} = 5/3).
\end{aligned}
\tag{2.90}
$$

Figures 2.16 and 2.17 below respectively show the gas density profiles with varying time and α, for the fiducial parameters in Equation (2.62). For the freely expanding wind, $n(r < R_1)$ is given by Equation (2.10), while the densities at R_1 and R_2 are given by the jump conditions. For the density at R_c, the factor j_c in Equation (2.89) gives an empirical approximation of $n(R_c)$ for the purpose of linearly approximating the shocked ambient density profile (see below).

For the shocked wind, we have extended the work of KM92's Section 3 and Appendix B to include the analysis of W77. Note that the form of density in Equation (2.88) uses

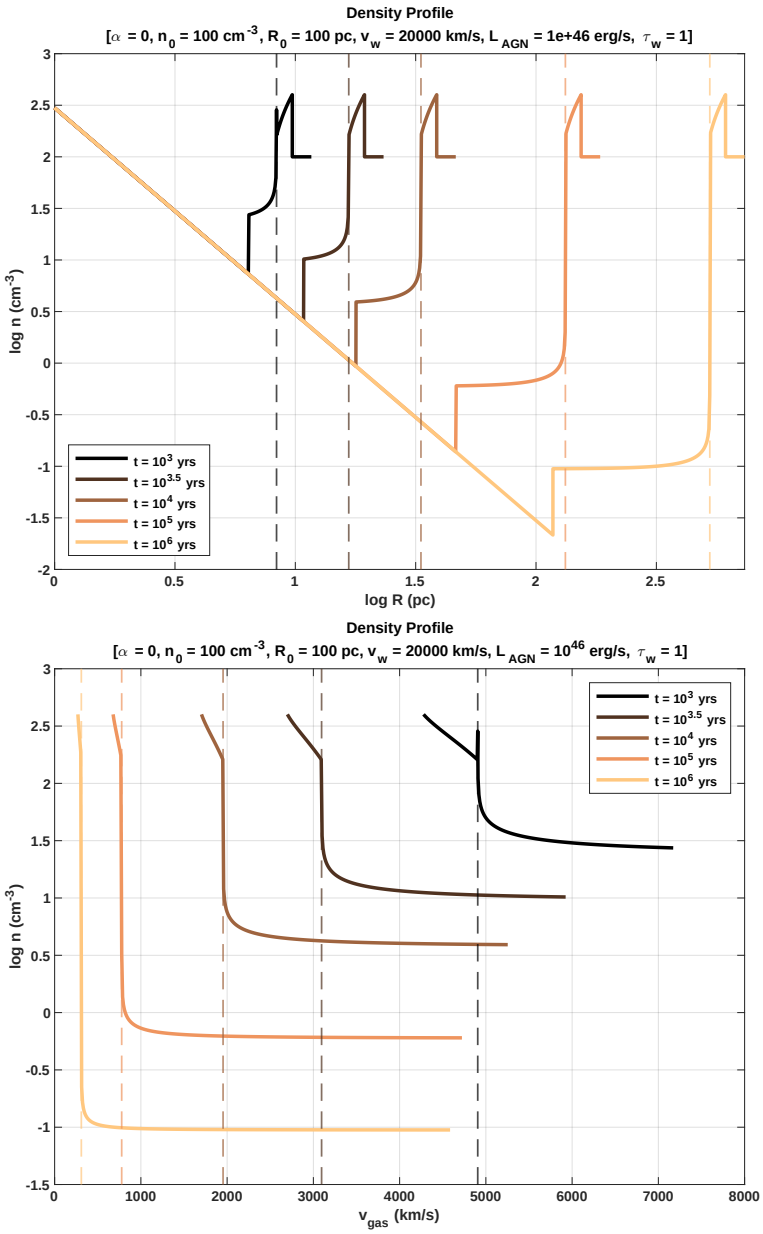

Figure 2.16: Gas density vs. distance from the AGN (top panel) and gas velocity (bottom panel) with varying times for the fiducial parameters in Equation (2.62), with the dashed lines indicating the contact discontinuity R_c for each profile. We note the shell formation time $t_{sf}^{FF} \approx 10^{4.0}$ years, as mentioned in Section 2.2.1.

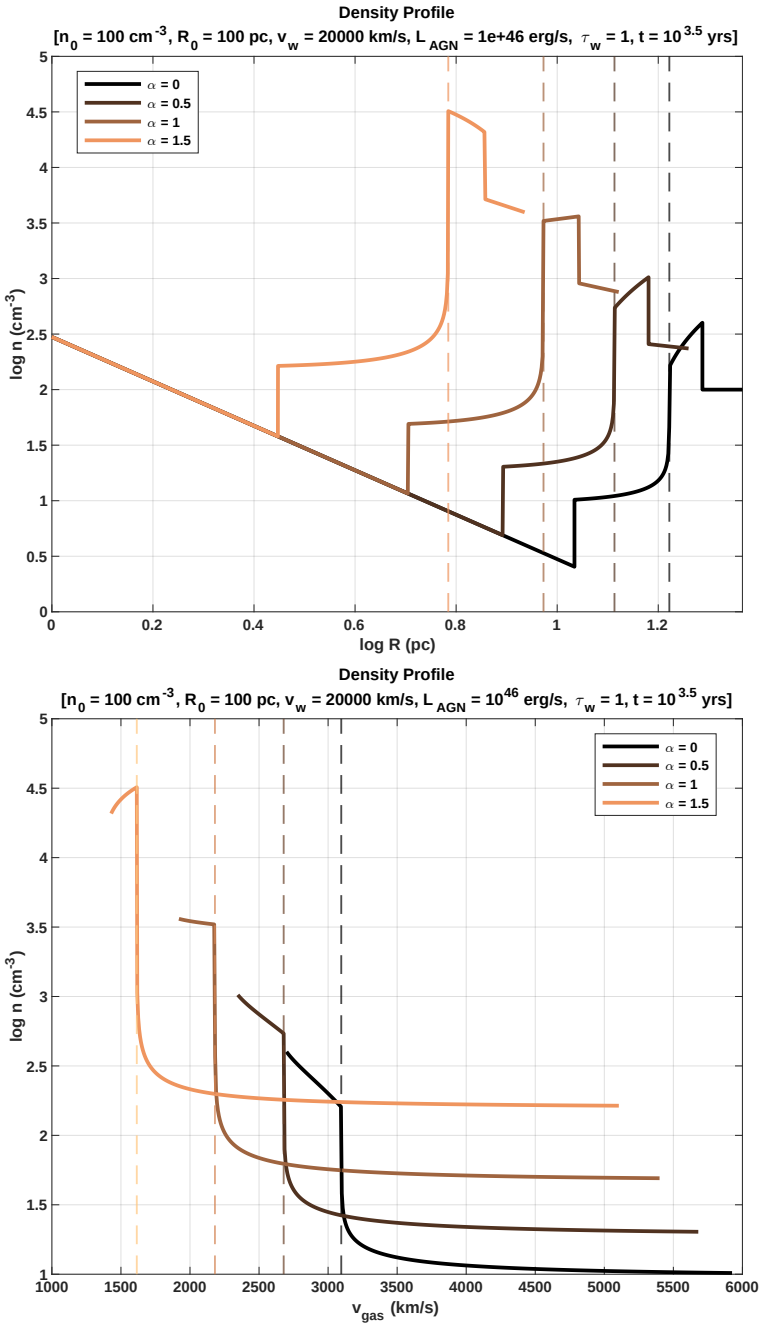

Figure 2.17: Gas density vs. distance from the AGN (top panel) and gas velocity (bottom panel) with varying density gradients for the fiducial parameters in Equation (2.62), with the dashed lines indicating the contact discontinuity R_c for each profile. We note that the outflow is initially radiative for the fiducial parameters with $\alpha = 1.5$, and will be unstable in the intermediate phase; ignoring this, the outflow becomes adiabatic after ~ 30 yr and the shocked ambient region becomes adiabatic after ~ 240 yr, since $\alpha > \alpha_{sf,E}^{FF}$ (Section 2.2.1).

KM92's late-time expression for R_1 (see their equation (B16)) which is different than their expression obtained by mass conservation (their Equation (5.4)), which is valid for both early and late times. To directly compare to W77 (their Equation (16)), we can obtain the mass density for the region (in their format) by taking n_{gas} and expanding the left-most bracketed term on the right hand side of the expression (in terms of α, via Equations (2.20) and (2.82)), expanding the unbracketed $1/R_c^3$ term (in terms of t and $\dot{M}_w$, via Equations (2.3), (2.13) and (2.20)), and then multiplying by μm_p. This yields

$$\rho_{gas}(R_1 < r < R_c) = \frac{5(5-\alpha)}{4\pi(11-\alpha)\lambda_c^3}\left[\frac{6\rho_0 R_0^\alpha \dot{M}_w^{\frac{2-\alpha}{3}}}{(3-\alpha)v_w^2\Gamma_{rad}\xi}\right]^{\frac{3}{5-\alpha}}\left[1-\frac{r^3}{R_c^3}\right]^{-\frac{2(4+\alpha)}{3(11-\alpha)}} t^{-\frac{4+\alpha}{5-\alpha}}, \quad (2.91)$$

and we see that the model parameter exponents are the same; evaluating the numerical terms along with the λ_c, $\Gamma_{rad}\xi$ and α-dependent terms for $\alpha = 0$, $\gamma_{sw} = 5/3$ confirms W77's original result, yielding a scaling factor of 0.623, only 0.8% lower than W77's 0.628. The density becomes infinite at R_c (unless $\alpha > 11$, which is implausible), but the integrated mass is finite for all $\alpha < 5$.

For the shocked ambient gas, KM92's Figure 4b shows that a linear density profile is a reasonable approximation for most of the region, with the slope being a decreasing function of α; to make this approximation, we approximate the value j_c using the results in KM92 Table 3 and Figure 4b. The slope is zero for $\alpha = \sqrt{20/17} \approx 1.085$, and we note that the density at the contact discontinuity is increasingly underestimated as α increases past this point, by up to a factor of $\sim$1.5 in $\sim$5% of the shocked ISM region just outside R_c as $\alpha \to 2$.

Finally, the ambient density is just a reiteration of the assumed profile in Equation 2.5.

2.2.3.4 Column Density

The particle column density N_{gas} is found by integrating the number density n_{gas} along the line of sight toward the centre, from larger r to smaller r in steps of $-dr$. We consider the column densities of the different regions separately, so that

$$\begin{aligned} N_{region}(R_{in} < r < R_{out}) &= -\int_{R_{out}}^{r} n_{gas}(r)dr = \int_{r}^{R_{out}} n_{gas}(r)dr \\ N_{region,tot} &= N_{region}(r = R_{in}) = \int_{R_{in}}^{R_{out}} n_{gas}(r)dr, \end{aligned} \tag{2.92}$$

where R_{in} and R_{out} are the inner and outer boundaries of the region (e.g., $R_{in} = R_c$ and $R_{out} = R_2$ for the shocked ambient region). We present results for the freely expanding wind and shocked ambient gas regions, while for the shocked wind region the the term $[1 - r^3/R_c^3]^{-2(4+\alpha)/3(11-\alpha)}$ needs to be integrated numerically.

Integrating Equation (2.88) for the freely expanding wind is straightforward, though we cannot integrate all the way inward to $r = 0$; we assume that the wind is launched from a radius r_L and enters our line of sight at a radius $r_{LOS} \in (r_L, R_1)$, so that

$$\begin{aligned} N_w(r_{LOS} < r < R_1) &= \frac{\dot{M}_w}{4\pi\mu m_p v_w}\left(\frac{1}{r} - \frac{1}{R_1}\right) \\ N_{w,tot} &= \frac{\dot{M}_w}{4\pi\mu m_p v_w}\left(\frac{1}{r_{LOS}} - \frac{1}{R_1}\right). \end{aligned} \tag{2.93}$$

For the shocked ambient region, the integration is simplified by the use of dimensionless variables; defining the dimensionless radii and number density

$$r_\circledast \equiv \frac{r}{R_c} - 1; \quad \mathcal{F}_\circledast \equiv \frac{\lambda_c}{1-\lambda_c} r_\circledast; \quad n_\circledast \equiv \frac{n_{gas}}{n_{gas}(R_c)} - 1 \tag{2.94}$$

so that the "fractional distance" $\mathcal{F}_\circledast \in [0, 1]$, our linearity assumption for the density in the

region (Equation (2.88)) becomes $n_{\circledast} = J_c \mathcal{F}_{\circledast}$ and one can show that $dr = (1-\lambda) R_2 d\mathcal{F}_{\circledast}$ and $n_{gas} = j_c n_0 R_0^{\alpha} R_2^{-\alpha} (n_{\circledast} + 1)$. Making the appropriate substitutions in the integral, the column density for the region is

$$\begin{aligned} N_{sa}(R_c < r < R_2) &= (1-\lambda_c) n_0 R_0^{\alpha} R_2^{1-\alpha} [j_c(1-\mathcal{F}_{\circledast}) + (4-j_c)(1-\mathcal{F}_{\circledast}^2)/2] \\ N_{sa,tot} &= (1-\lambda_c) n_0 R_0^{\alpha} R_2^{1-\alpha} [2 + j_c/2], \end{aligned} \tag{2.95}$$

where for the total column density we have substituted $\mathcal{F}_{\circledast} = 0$ (representing the contact discontinuity).

Another quantity of interest is the velocity derivative of N_{gas} – since this is what we actually observe in a high-resolution spectrum – in units of $(\mathrm{cm}^{-2})/(\mathrm{km\,s}^{-1})$. Our column density differential is $dN_{gas} = -n_{gas} dr$ (negative because we integrate inward), and thus we have

$$N_v \equiv \frac{dN_{gas}}{dv} = -n_{gas} \frac{dr}{dv} = -\frac{n_{gas}}{\partial v / \partial r}, \tag{2.96}$$

where in the last equality we have substituted $dr/dv = (\partial v/\partial r)^{-1}$ due to the fact that the column density is integrated at an instant in time, i.e. $dt = 0$. Taking the radial partial derivative of Equation (2.80), we get:

$$\begin{aligned} N_v(R_1 < r < R_c) &= \left[\frac{\phi_E}{3\gamma_{sw}} + 2\left(\beta_E + \frac{\phi_E}{3\gamma_{sw}}\right) \frac{R_c^3}{r^3} \right]^{-1} n_{gas} t \\ N_v(R_c < r < R_2) &= \left[2\beta K_{v,sa} \left(C_{v1} + C_{v2} \frac{r}{R_2} \right) \right]^{-1} n_{gas} t \end{aligned} \tag{2.97}$$

Since n_{gas} represents a hydrogen density and hydrogen is the most abundant element, one may convert N_v to an upper limit N_v for other ions by accounting for their relative abundance and ionisation fraction.

Figures 2.18 and 2.19 below respectively show the gas N_v profiles with varying time and α, for the fiducial parameters in Equation (2.62).

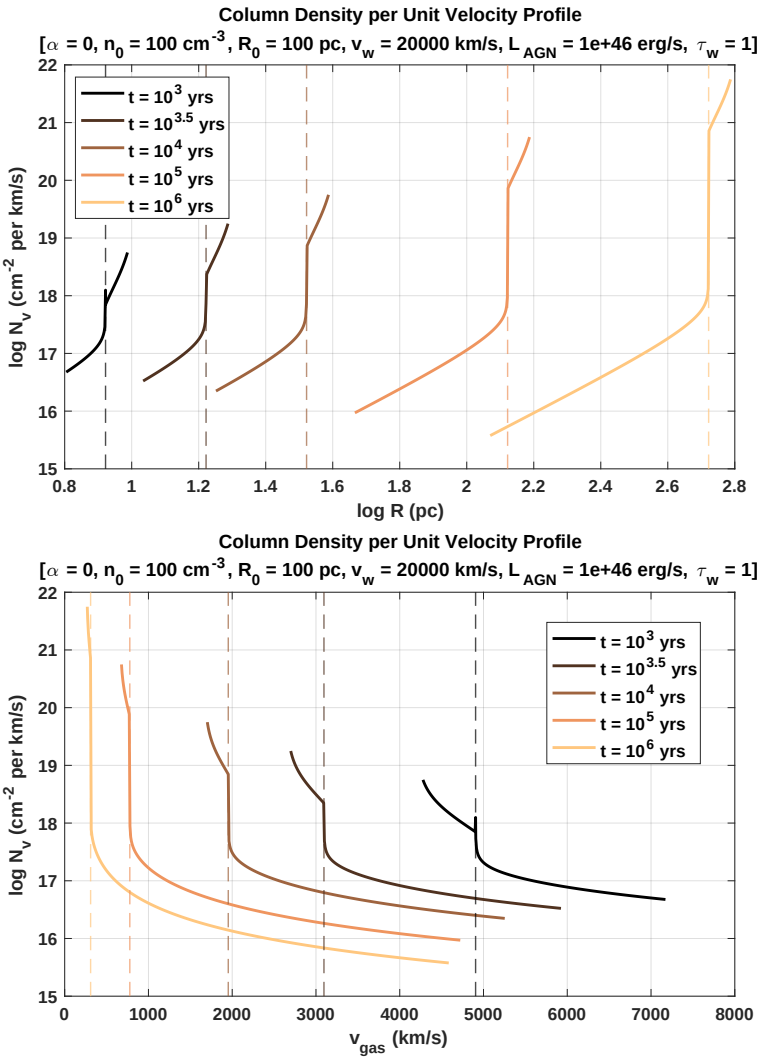

Figure 2.18: Gas column density per unit velocity vs. distance from the AGN (top panel) and gas velocity (bottom panel) with varying times, for the fiducial parameters in Equation (2.62), with the dashed lines indicating the contact discontinuity R_c for each profile. We note the shell formation time $t_{sf}^{FF} \approx 10^{4.0}$ years, as mentioned in Section 2.2.1.

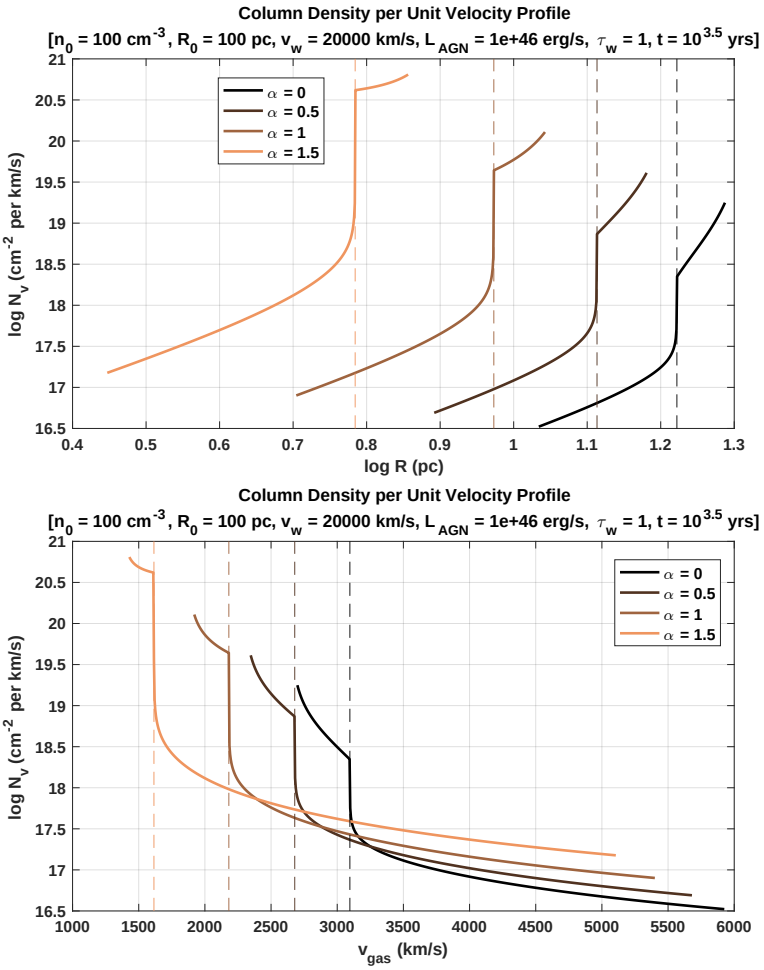

Figure 2.19: Gas column density per unit velocity vs. distance from the AGN (top panel) and gas velocity (bottom panel) with varying density gradients for the fiducial parameters in Equation (2.62), with the dashed lines indicating the contact discontinuity R_c for each profile. We note that the outflow is initially radiative for the fiducial parameters with $\alpha = 1.5$, and will be unstable in the intermediate phase; ignoring this, the outflow becomes adiabatic after ~ 30 yr and the shocked ambient region becomes adiabatic after ~ 240 yr, since $\alpha > \alpha_{sf,E}^{FF}$ (Section 2.2.1).

2.3 Closing Remarks

In this section we have presented an expanded spherical blast wave model of quasar accretion disk winds, built on the methods of W77 and KM92, for the case of constant mass injection ($\eta_{in} = 1$, Equation (2.40)). We also briefly analysed the biconical outflow model of ZH+19, deriving the self-similarity parameter for its single phase and comparing its physical scale to the spherical model (Sections 2.1.1, 2.1.2.4 and 2.1.5).

In terms of global outflow dynamics (Section 2.1), for the self-similar solution (Section 2.1.2) we have condensed KM92's method of determining the intermediate-phase self-similarity parameters, allowing for quick adaptation of different cooling mechanisms to the model. In particular, we derived the self-similarity parameters for FGQ12's two-temperature plasma (TTP) cooling and a generic referential (REF) cooling mechanism where the energy loss rate $\dot{\varepsilon} \propto n^2\Lambda(T)$, with cooling function $\Lambda(T) = \Lambda_0 T^\eta$ (KM92 used $\eta = -1/2$ for cooling in a gas in collisional ionisation equilibrium). Notably, we found that for the REF regime, β_I is notably independent of η, leading to phase transition conditions (Sections 2.1.3.3 and 2.1.3.4) which are also independent of η. In the process of exploring phase transitions and energy/momentum coupling (2.1.4), we found a correspondence between the phase transition conditions in the intermediate phase, the steady phases of evolution, the hierarchy of late-time β values and the increasing or decreasing (or stationary) nature of the intermediate-phase energy and momentum coupling factors $\mathcal{E}_I$ and $\mathcal{B}_I$. In Section 2.1.3.6 we presented plots the distributions of the criterion parameter (which determines the initial phase; Equation (2.41)) and phase transition times for the TTP cooling regime, using the assumed uniform (or log-uniform) distribution of model parameters outlined in Section 2.0.2.

In terms of the outflow structure and local/regional gas dynamics (Section 2.2), we expanded KM92's analysis of shocked ambient cooling to the case of free-free cooling (REF cooling with $\eta = 1/2$) and calculated/plotted the distribution of shell formation times

using the Λ_0 value of ZH+20 and the random model parameter sampling regime outlined in Section 2.0.2. Finally, we provided novel, analytically approximate expressions for the profiles of various gas observables (velocity, acceleration, density and column density) throughout the various regions of the outflow structure, with sample plots of said profiles showing their trends over time and, in the case of density and column density, varying density gradients (α).

3 Searching for Deceleration: Observations of J0300

Given our range of α, the blast wave model predicts strictly decelerating gas in the outflow despite the constant energy input, with the deceleration magnitude in each region given by Equation (2.86) and minimum magnitude being reasonably approximated by Equation (2.87). We search for this deceleration directly in the Ca II portion of our target's spectrum, paving the way for a discussion of the results (Section 4) in the context of Section 2.

3.1 Choice of Target

Our target J0300 (SDSS J030000.56+004828.0; Hall et al. 2002) was observed at high spectral resolution in 2001 (Hall et al. 2003; see Section 3.2), and we adopt the same systemic redshift of $z = 0.89185$ used in that paper. It is an iron low-ionisation broad absorption line (FeLoBAL) quasar, and has the highest equivalent width Ca II BAL trough known. Strong Ca II $\lambda\lambda$3934,3969 absorption is seen outflowing at $v \simeq 2000 - 4000$ km s^{-1} with weaker Ca II absorption at $v \simeq 1700 - 2000$ km s^{-1} and $v \simeq 4000 - 5660$ km s^{-1} (Figure 3.1 and Figures 3-6 of Hall et al. 2003).

We chose this target for its outflow in which, as mentioned in Section 1, lower velocity gas is inferred to be at greater distances (see also Figure 2.13), and for its existing high-

resolution spectrum. Also, unlike low-velocity Mg II or C IV in many BAL quasars, the unsaturated Ca II absorption in J0300 (Figure 3.1) has considerable structure in velocity space which should aid in detecting velocity shifts. Lastly, the relatively high velocities of its Ca II suggest that if the outflow's current phase does arise from a blast wave, the outflow is relatively young, which is when any deceleration is expected to be largest and most easily detectable.

3.2 Previous High-Resolution Spectrum (UVES)

Observations of J0300 were obtained on UT 10-12 Aug 2001 (MJD 52131-52133) using the ESO Very Large Telescope (VLT) Unit 2 (Kueyen) and Ultra-Violet Echelle Spectrograph (UVES; proposal PI: Patrick Hall). A $1''$ slit was used, which in combination with subarcsecond seeing yielded a resolution $R \simeq 52,000$ at our wavelengths of interest. A depolariser was also used for all observations. We use the SQUAD (Murphy et al., 2019) reductions of these observations, downloaded from the ESO Science Archive. The SQUAD reductions produce continuum-normalised spectra at vacuum heliocentric wavelengths. We found that the wavelength solution of the UVES spectrum used in Hall et al. (2003) was such that features in it appear at wavelengths 2.1 ± 0.1 km s^{-1} to the red as compared to the same features in the SQUAD spectrum. The wavelength solution of the SQUAD reduction is consistent with the wavelength solution of the new observations discussed in the next section. The spectrum has an average signal-to-noise ratio per km s^{-1} in the wavelength region of interest of SNR/(km s^{-1}) = 25.5 and is shown in the top panel of Figure 3.1.

3.3 New High-Resolution Spectrum (GRACES)

New observations of J0300 were obtained on the night of November 13th 2019 (MJD 58800) using the GRACES instrument (Chene et al., 2014) on the Gemini-North telescope

(proposal PI: Patrick Hall). GRACES consists of a fiber optic cable which takes the light collected with Gemini-North through a 1.2 arcsecond diameter aperture on the sky and feeds it to the ESPaDOnS spectrograph (Donati et al., 2006) at the Canada-France-Hawaii Telescope (CFHT).

We used the one-fiber observing mode to obtain a spectrum of resolution $R \simeq 60,000-65,000$ with 2.6 $\mathrm{km\,s^{-1}}$ $\mathrm{pixel^{-1}}$. We obtained 4 exposures of 2400s each.

Each exposure was reduced individually using the OPERA pipeline (Martioli et al., 2012). OPERA is based on the Libre-ESpRIT package (Donati et al., 1997). OPERA places the individual GRACES exposures on an heliocentric atmospheric wavelength scale, corrected using telluric lines. (The telluric corrections range from $-0.079\,\mathrm{km\,s^{-1}}$ to $+0.045\,\mathrm{km\,s^{-1}}$, and were applied despite having quoted uncertainties of $\pm 0.33\,\mathrm{km\,s^{-1}}$.) We converted these wavelengths to vacuum heliocentric wavelengths using the formula of Morton (1991). We describe how we combined these exposures in the next subsection; the combined spectrum is shown in the bottom panel of Figure 3.1.

3.4 Processing and Cross-Correlation

We measured the velocity shift over the time between the UVES and GRACES observations by cross-correlating the spectra and finding the shift that gives the maximum correlation. The processing prior to this is described below.

First, we visually compared the Ca II broad absorption troughs in the two spectra; no dramatic changes in the broad absorption profile shapes occurred between the two epochs.

The wavelength region of interest was isolated as 7312.000 Å to 7520.026 Å (vacuum heliocentric). We have four separate GRACES exposures, and in each exposure there are two orders which overlap in wavelength near the centre of the above wavelength range. Because the central wavelengths for each pixel in each exposure were slightly different, we treated each order from each exposure as a separate spectrum and combined all spectra

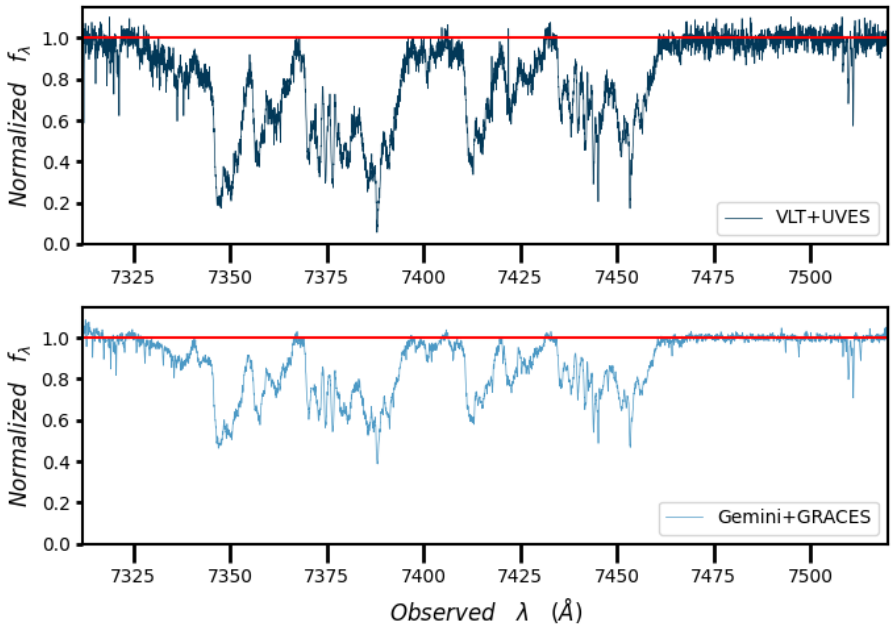

Figure 3.1: Top: Ca II $\lambda\lambda$3934,3969 absorption in the continuum-normalised 2001 UVES spectrum of J0300. At far left, below 7340 Å there is weak high-velocity λ3934 absorption. At far right, the narrow absorption at 7510 Å is λ3969 absorption at the quasar systemic redshift. In between is absorption in both transitions at wavelengths corresponding to outflow velocities v=1700-4000 km s^{-1}. Bottom: Ca II $\lambda\lambda$3934,3969 absorption in the continuum-normalised 2019 GRACES spectrum of J0300. The absorption is shallower in the GRACES spectrum because that spectrum was obtained through an optical fiber which includes light from the sky.

at a given wavelength together as discussed below.

To combine the GRACES spectra, we used the scombine task in IRAF.[2] Prior to combining, we used fifth-order polynomial interpolation to resample the spectra to a logarithmic wavelength scale of 0.1 $\mathrm{km\,s^{-1}}$ $\mathrm{pixel^{-1}}$, for 84100 pixels total over our wavelength range. We created a weighted average spectrum using the uncertainty values at each pixel from each exposure. The weighted average GRACES spectrum has a SNR/($\mathrm{km\,s^{-1}}$) ranging from 22 to 47 in the region of interest.

We confirmed that pixels with spurious values (from cosmic rays, e.g.) were not affecting the weighted average spectrum by comparing to a median spectrum (with the median of an even number of pixels computed as the average of the two central values); no significant differences were found. The GRACES spectrum does, however, contain a number of sky emission-line and absorption-line features, particularly below 7350 Angstroms. We manually created pixel masks used to interpolate over emission-line features, but did not do the same for absorption-line features.

The UVES spectrum was resampled to the same wavelengths as the GRACES spectrum using fifth-order polynomial interpolation.

Finally, we normalised the GRACES spectrum by an estimate of the underlying quasar continuum consisting of a fourth-order polynomial fit to five wavelength regions in which the UVES spectrum had an average normalised flux of 0.98 or higher. The normalised GRACES spectrum is shown in the bottom panel of Figure 3.1.

For purposes of estimating cross-correlation uncertainties, we created 100 simulated UVES spectra and 100 simulated GRACES spectra, each with added noise: in both cases the simulated flux in a given pixel, $f_{\lambda,sim}$, was randomly drawn from the normal distribution $\mathcal{N}(f_\lambda, \sigma_\lambda^2)$, where f_λ and σ_λ are the measured flux and corresponding uncertainty at that pixel. For UVES, the original spectrum was used as f_λ, and the simulated spec-

[2]The Image Reduction and Analysis Facility was distributed by the National Optical Astronomy Observatories.

trum was then resampled in the same fashion as the actual spectrum. For GRACES, each order from each exposure was used as f_λ, and the resulting simulated input spectra were processed in the same fashion as the actual spectra to produce a simulated output spectrum.

3.4.1 Wavelength Calibration Check

To check for any shift in the wavelength calibration between the UVES and GRACES spectra, we compared two regions of strong sky absorption lines using vacuum geocentric wavelengths. For the UVES spectrum, this meant removing the heliocentric correction that had been applied. For each individual GRACES exposure, we removed its heliocentric correction before converting to vacuum wavelengths and combining all exposures in the same manner as the science exposures. The two regions cover vacuum geocentric wavelengths of 7590 Å to 7640.004 Å (in the atmospheric A band) and 6868 Å to 6923.002 Å (in the B band), both using $0.1\,\mathrm{km\,s^{-1}}$ pixels.

We cross-correlated the spectra for each sky line region separately. Before doing so, following the cross-correlation scheme of Tonry & Davis (1979) we zeroed their continua by subtracting 1 and then tapered their edges (5% of the total pixels at each edge of the spectra) by multiplying them with a half-cosine bell function to de-weight any abrupt cutoff.

We estimated uncertainties using 100 simulated spectra of each region for each instrument, created as described above (before the beginning of this subsection). We cross-correlated all 10,000 possible pairs of such spectra and adopted the standard deviations of the resulting shift distributions as our uncertainties. This procedure yields shifts of 8 $\pm$ 0.5 and 6 $\pm$ 0.3 pixels for the A and B bands respectively (features in the GRACES spectrum appear at longer wavelengths than in the UVES spectrum), with the A band result having a larger uncertainty due to broader sky lines in that spectral region at our

resolution. The temperatures during the nights of our observations were not unusually high or low, so we rule out temperature effects as a significant source of systematic wavelength calibration error. Regardless of the origin of the wavelength calibration offset, we must account for it to determine any velocity shift in the J0300 outflow between our two epochs of observation.

A weighted average of the A and B band results yields a shift of 6.5 ± 0.5 pixels, but for simplicity we adopt the B band integer-pixel shift and acknowledge the different values measured in the two bands by adopting a systematic uncertainty of 1 pixel. We remove the offset of 0.6 ± 0.1 $\mathrm{km\,s^{-1}}$ from the GRACES spectrum and place both spectra on the UVES wavelength scale. This shift has the advantage of placing the associated Ca II H absorption at the same velocity in each spectrum (see Section 3.4.2 and Table 3.1). It is also within the expected accuracy of the GRACES wavelength solution of $1 - 2$ $\mathrm{km\,s^{-1}}$ (K. Chiboucas, personal communication to P. Hall).

3.4.2 Cross-Correlation

The velocity shift between the UVES and GRACES Ca II spectra were measured and uncertainties estimated in the exact same manner as for the wavelength calibration check. The resulting cross-correlation function can be seen in Figure 3.2, with autocorrelations of both spectra for comparison. Taking into account the wavelength calibration, we find the cross-correlation maximised at a shift of 0.3 ± 0.3 $\mathrm{km\,s^{-1}}$ (statistical) ±0.1 $\mathrm{km\,s^{-1}}$ (systematic) in the quasar reference frame, corresponding to a statistically insignificant bulk acceleration of the outflow. The maximum normalised cross-correlation coefficient is 0.988.

Using the same method, we performed separate cross-correlations on eight select subsections of the spectra. A description of these subsections, along with their wavelength ranges and measured shifts, can be found in Table 3.1.

We cross-correlated the Ca II H and K absorption regions separately, and also cross-correlated low-velocity (1899-3084 km s^{-1}) and high-velocity (3084-4540 km s^{-1}) partitions of these regions in order to check for differential shifts as a function of velocity (see Section 4.2). We find that in each case the shifts of the H and K cuts in a given velocity range agree to within the uncertainties, and that the full H and K profile shifts agree with the full spectrum shift. We also note a substantial but statistically insignificant ($< 3\sigma$) difference between the shifts of the low- and high-velocity cuts, with the low-velocity cuts decelerating and the high-velocity cuts accelerating. As expected, the bulk shift lies between the low- and high-velocity shifts, but closer to the low-velocity shifts due to their sharper features (which yield lower uncertainties).

The associated Ca II H absorption has zero shift by expectation and by design (Section 3.4.1). The low-velocity Ca II H wavelength region is contaminated by associated absorption from Ca II K. We tested whether this affected the cross-correlation shift in the region by interpolating over the contaminating absorption and recalculating the cross-correlation. We found that the shift was smaller by 1 pixel, well within the uncertainty of $\pm$ 2.6 pixels, so we conclude that the contamination does not significantly affect the cross-correlation signal in this region.

3.5 Closing Remarks

As a reminder, we work in a frame centered on the quasar such that along the line of sight from the quasar to us all outflow velocities from the quasar are positive, acceleration of an outflow away from a quasar has a positive sign, and deceleration of an outflow has a negative sign (as in Table 3.1).

Including our systematic uncertainty, we place a 3σ limit of $|\Delta v| < 1$ km s^{-1} on any bulk change of the velocity of the $v = 1700 - 4000$ km s^{-1} Ca II outflow in J0300 between our two observations. At a redshift of $z = 0.89185$, our observations are separated by 9.65

J0300 Cross-Correlation Table

Cross-Correlations		
Sky Lines		
Description of Spectrum	*Wavelength Range* (Å)	*Velocity Shift* ($\mathrm{km\,s^{-1}}$)
A Band	7590.000−7640.004	0.8±0.05
B Band	6868.000−6923.002	0.6±0.03
Ca II Absorption		
Description of Spectrum	*Wavelength Range* (Å)	*Velocity Shift* ($\mathrm{km\,s^{-1}}$)
Full Profile	7312.000−7520.026	+0.3±0.30±0.1
Associated Ca II H	7500.000−7520.026	+0.0±0.45±0.1
Ca II H & K	7332.127−7462.447	+0.3±0.28±0.1
Ca II H	7397.000−7462.447	+0.2±0.38±0.1
Ca II K	7332.127−7397.000	+0.5±0.46±0.1
Ca II H (low v)	7433.000−7462.447	−0.1±0.26±0.1
Ca II K (low v)	7367.811−7397.000	−0.4±0.44±0.1
Ca II H (high v)	7397.000−7433.000	+1.2±1.27±0.1
Ca II K (high v)	7332.127−7367.811	+1.9±0.72±0.1

Table 3.1: Velocity shifts of various spectra (GRACES with respect to UVES) as measured by cross-correlation maxima. The skyline velocity shifts are given in the geocentric frame as $v_{\mathrm{shift}} \pm \sigma_{\mathrm{statistical}}$, while the Ca II absorption shifts are adjusted for the calibration offset of Section 3.4.1 and given in the quasar rest frame as $v_{\mathrm{shift}} \pm \sigma_{\mathrm{statistical}} \pm \sigma_{\mathrm{systematic}}$. The low and high velocity ranges are respectively 1899-3084 $\mathrm{km\,s^{-1}}$ and 3084-4540 $\mathrm{km\,s^{-1}}$ for both the H and K lines.

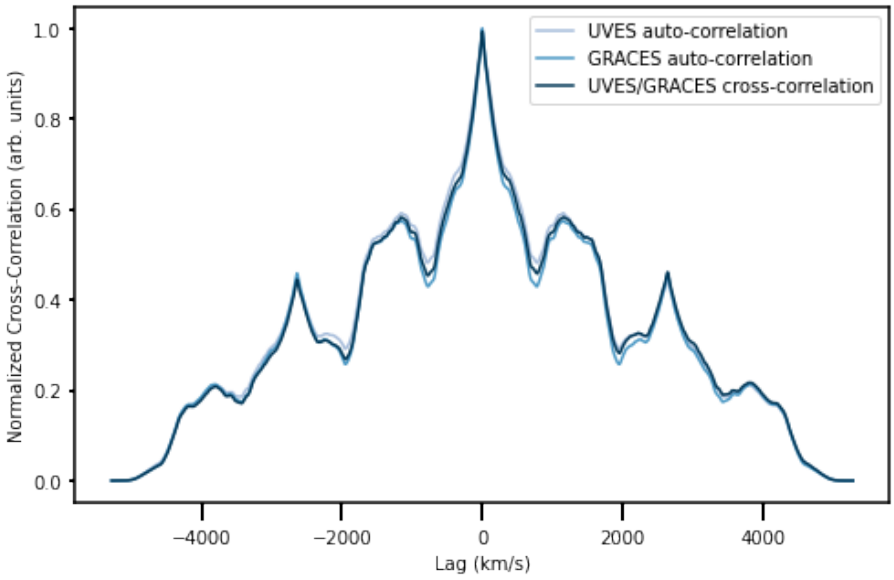

Figure 3.2: Normalised UVES/GRACES cross-correlation function for the full Ca II absorption profile (see Table 3.1), using the weighted masked average GRACES spectrum. The autocorrelations of both spectra are overlaid for comparison.

rest-frame years. Given that, our observations place a 3σ limit of $|a| < 0.1$ km s^{-1} yr^{-1} ($< 3 \times 10^{-4}$ cm s^{-2}) on the average magnitude of any bulk deceleration (or acceleration) of the Ca II outflow between our two observations.

4 Discussion

Here we discuss the properties of J0300 found in the literature, in relation to the combined blast wave model and our cross-correlation results. We remind the reader that that we assume the absorbing Ca II observed in J0300 arises in the shocked ambient region, and thus in the context of Section 2 our analysis concerns the local gas dynamics (Section 2.2) in the shocked ambient region of adiabatic outflows (Section 2.1.2.2), which may collapse into a thin shell for $\alpha < 1.4$ (Section 2.2.1).

4.1 Potentially Relevant Properties of J0300 and Other Ca II BAL Quasars

J0300 is part of the sample of Choi et al. (2022), who summarise past observations of this quasar in their Appendix C. We compare to their results further below.

Hall et al. (2003) note that the lack of absorption from low-energy excited states of Fe II accompanying the strong Ca II absorption at $2000 < v < 4000$ km s^{-1} in J0300 means that the gas at those velocities must have either a density or a temperature too low to significantly populate such states (e.g., via electron-ion collisions). In practice, this means $n_e < 10^3$ cm^{-3} or $T \lesssim 1100$ K or both.

Rogerson et al. (2011) compared X-ray and UV absorption properties of J0300 and found the absorbing column toward the X-ray emitting region along our line of sight is $N_H \geqslant 1.8 \times 10^{24}$ cm^{-2}. Although the X-ray and UV absorption in J0300 might not arise in the same gas, they found that many properties of the UV absorption in Mg II and Fe II* at $4000 < v < 10850$ km s^{-1} can be matched with a slab of gas of constant density $n_e = 10^6$ cm^{-3} with ionisation parameter $\log U = -0.5$ at its ionised face (implying a distance of ∼60 pc from the black hole) and a thickness of $\sim 3 \times 10^{18}$ cm (∼1 pc).

The only other quasar with outflowing Ca II absorption that has been studied in detail is Mrk 231, which has Ca II outflowing at $v \simeq 4000 - 5000$ km s^{-1} (Leighly et al., 2014). Leighly et al. (2014) find that a constant-pressure slab can explain the observed Ca II in Mrk 231 as arising in a region with density $n \gtrsim 10^6$ cm^{-3} and temperature $T \lesssim 10^3$ K. They find that a jump in density at the hydrogen ionisation front is needed to simultaneously explain the observed columns of higher-ionisation gas at higher velocities (traced by He I*) and lower-ionisation gas such as Ca II at lower velocities. They interpret this finding as evidence for a high-velocity wind impacting, compressing, and accelerating preexisting dusty gas in the host galaxy ISM. In their models, the absorption is produced

in a region of thickness ≃0.027 pc at a distance of 13-230 pc from the quasar.

4.2 Velocity Range of Shocked ISM Gas

Absent effects external to the model, the self-similarity assumption for the blast wave fundamentally limits the range of velocities found in the shocked ISM: because the velocity gradient is negative in the region, the boundary conditions $v_{gas}(R_c) = \lambda_c v_{R2}$ and $v_{gas}(R_2) = K_{v,sa} v_{R2}$ imply that the gas velocity there spans a factor $\lambda_c / K_{v,sa}$ (~ 1.1 for $\gamma_{sa} = 5/3$). However, the velocity range of the strong Ca II-absorbing gas in J0300 spans a factor ~ 2, from 2000 $\mathrm{km\,s^{-1}}$ to 4000 $\mathrm{km\,s^{-1}}$ (Hall et al., 2003), or a factor of 3.3, extending from 1700 $\mathrm{km\,s^{-1}}$ to 5660 $\mathrm{km\,s^{-1}}$, if considering all detected Ca II absorption. We find empirically that the KM92 hydrodynamic equations can only reproduce factors $\gtrsim 2$ for unrealistic values of $\gamma_{sa} \gtrsim 5$. While typical adiabatic index values are in the range $\gamma \in (1, 2)$, magnetic fields may alter this: in the presence of weak magnetic fields ($< 20\ \mu$G), quoting Falle (1975b), "the main effect of the field is to increase the effective ratio of specific heats [λ_{sa}]. This leads to a faster expansion and, in this case at least, is more important than the tension along the field lines which ought to retard the expansion." However, Chao & Wiskerchen (1974) show that even for strong fields, one finds a realistic maximum value of $\lambda_{sa} = 2$ (as opposed to $\gamma_{sa} = 5/3$; see their Figure 2).

A number of explanations, explored below, may offer a way around this limitation; however, absent an extension of TTP cooling to the shocked ambient region, all but the last two appear to be ruled out in J0300.

Cavaliere et al. (2002) state that a weak shock can produce $\lambda_c \sim 0.45$, which might lead to a velocity range factor $\lambda_c / K_{v,sa} \sim 1/0.45 = 2.2$. A weak shock in this case is defined as $\Delta E / E \simeq 0.3$, where ΔE is the injected energy and E is the preexisting thermal energy of the ISM. However, it seems unlikely that a weak shock could result from a quasar outflow with an initial velocity of 10,000 $\mathrm{km\,s^{-1}}$ or higher unless a new outflow is injected into an

old blast wave that has not yet cooled substantially.

Bautista & Dunn (2010) argue that turbulence from supersonic ionisation fronts caused by variations in a quasar's luminosity can produce velocity structure in BAL gas that scales roughly with the Alfven velocity in the gas. The observed Ca II velocity span of 2000 $\mathrm{km\,s^{-1}}$ in J0300 would require magnetic field strengths of up to order 40 mG. Strengths of up to 10 mG have been postulated in models of BAL outflows; see Section 4 of Bautista & Dunn (2010).

We investigated the possibility that J0300 is observed in the brief phase around the shell formation time t_{sf} when the shocked ISM is losing pressure support and collapsing: according to section 5 of Falle (1975a), during this phase "the [outer] shock decelerates and the contact discontinuity accelerates" (as seen between times 2 and 4 in their Figure 3d). Because the gas just behind the outer shock is initially moving more slowly than the gas near the contact discontinuity, the above deceleration and acceleration combine to yield a larger velocity spread in the shocked ISM than either before or after the collapse. Figure 3d of Falle (1975a) shows a maximum velocity range of ~ 2.4 during this collapse phase, sufficient to reproduce that of strong Ca II in J0300. If this explanation for the velocity range of the Ca II in J0300 is correct, then differential changes in velocity across the outflow are expected: first, a larger deceleration at the lowest velocities and a smaller deceleration or even acceleration at the highest velocities, followed by an acceleration at the lowest velocities and a deceleration at the highest velocities as the shocked ambient velocities converge to the range $0.75v_{R2} \leqslant v \leqslant v_{R2}$ (ignoring any effects on v or ionisation from shocks in the collapsing shell). Most of the gas will have cooled and accelerated to v_{R2}; only recently swept-up gas will have $0.75v_{R2} \leqslant v < v_{R2}$. Table 3.1 shows an intriguing but not statistically significant suggestion of deceleration at low velocities and acceleration at high velocities in the outflow, however, the values found are not consistent with the above hypothesis: the timescale of shell formation is found to be $t_{collapse} \simeq 0.2t_{sf}$

in the simulations of Richings & Faucher-Giguère (2018b, their Figure A2), consistent with Case A of Falle 1975 (their Figure 3). In this scenario gas should shift from a velocity range $v_{Rc}/v_{gas}(R_2) = 4\lambda_c/3$ to $v_{Rc}/v_{gas}(R_2) = 2.4$, and then to $v_{Rc}/v_{gas}(R_2) = 4/3$, each in less than $t_{collapse}/2 \simeq 0.1 t_{sf}$ (and possibly much less). We consider an example in which the gas shifts from a range of $v_{gas}(R_2) = 2600$ km s^{-1} and $v_{Rc} = 3000$ km s^{-1} prior to shell formation, to $v_{gas}(R_2) = 1900$ km s^{-1} and $v_{Rc} = 4540$ km s^{-1} during shell formation, to $v_{gas}(R_2) = 2200$ km s^{-1} and $v_{Rc} = 2900$ km s^{-1} after shell formation. For $t_{sf} = 10^4$ yr, the velocity adjustments should occur over $< 10^3$ yr. Initially, this means decelerations of < -0.7 km s^{-1} yr^{-1} at low velocities and accelerations of $> +1.5$ km s^{-1} yr^{-1} at high velocities. At the end of the shell formation phase, this means accelerations of $> +0.3$ km s^{-1} yr^{-1} at low velocities and decelerations of < -1.6 km s^{-1} yr^{-1} at high velocities. Those values are all above our 3σ observational upper limit of $|a| < 0.1$ km s^{-1} yr^{-1} and can be ruled out. The resulting accelerations may be within our constraints if the shell formation time is longer due to TTP cooling, but this would require $t_{sf}^{TTP} \gtrsim 1.6 \times 10^5$ yr in order to bring the decelerations down by a factor of 1.6. For a set of realistic density parameters for J0300 (see Section 4.3.1), it takes an extremely fast wind speed of $v_w \sim 0.6c$ (as seen in Lanzuisi et al. 2012) for the outer shock to still be travelling 2,600 km s^{-1} by this time, and thus for a more plausible speed of order $\sim 0.1c$ (where the outer shock speed will be lower by this time), it is still implausible that this scenario explains the observed velocity range.

Finally, two ways to explain the velocity range of the Ca II outflow in J0300 (in the context of the blast wave model) are as follows: first, the Ca II-absorbing gas may lie in the shocked wind region as well as the shocked ambient region. In this case, the gas would span a larger velocity range, albeit at lower column densities (e.g., Figures 2.13 and 2.18). Second, preexisting relatively dense clouds of gas in the ISM may been accelerated from rest to their observed velocities in J0300 by the ram pressure of the surrounding shocked

low-density ISM gas. We consider this further in Section 4.4.

4.3 Comparison to Choi et al.

J0300 has also been studied in Choi et al. (2022) as one of 50 FeLoBAL quasars modeled using the spectral-synthesis code *SimBAL* (Leighly et al., 2018) to solve for the physical conditions in the gas producing the observed absorbing columns in those quasars. Choi et al. (2022) find that the best fit for J0300 has the absorbing gas at $1800 < v < 10600$ km s^{-1} located at 12.0 ± 0.3 pc from J0300 with an ionisation parameter $\log U = -1.85$, a density of $\log(n/\mathrm{cm}^{-3}) = 7.96^{+0.01}_{-0.02}$, and a column density $\log(N_H/\mathrm{cm}^{-2}) = 22.31$ (implying a thickness $dr = 7.3 \times 10^{-5}$ pc). Notably, the UV-absorbing outflow in J0300 has the highest density, lowest ionisation parameter, and largest distance inferred among the 8 overlapping-trough FeLoBALs studied by Choi et al. (2022) and in their full sample of 50 objects it has the largest velocity width and ties for the highest density. J0300 is also an exception to the finding of Choi et al. (2022) that Ca II absorption is generally found in BAL outflows located at kpc scales. However, while the Choi et al. (2022) *SimBAL* model for J0300 does an excellent job of fitting Mg II and Fe II absorption, it overpredicts the level of Ca II absorption at $v > 4000$ km s^{-1} and does not predict the strong Ca II at $2000 < v < 4000$ km s^{-1}. The latter is likely due to the use of a *SimBAL* model with a single ionisation parameter and a single density.

As a fiducial bolometric luminosity for J0300, we adopt $L_{AGN} = 1.32 \times 10^{47}$ erg s^{-1} as estimated by Choi et al. (2022). We assume a black hole mass of 3×10^9 $M_\odot$, appropriate for luminous quasars at this redshift (Rafiee & Hall, 2011), which yields an Eddington ratio of $f_{Edd} = 0.3$, $\dot{M}_{Edd} = 45$ $M_\odot$ yr^{-1}, and $\dot{M}_{acc} = 13$ $M_\odot$ yr^{-1}. For an initial wind velocity $v_w = 20{,}000$ km s^{-1}, J0300 would have $\dot{M}_w = 35\tau_w$ $M_\odot$ yr^{-1}. This yields a larger mass outflow rate from the disk/torus than the accretion rate through them for $\tau_w > 0.37$.

Anticipating results later in this section, for comparison to Choi et al. (2022) we

further adopt $R_2 = 12$ pc, $R_0 = 10$ pc, $n_0 = 10^3$ cm^{-3} and $\alpha = 0.8$; under the thin shell approximation, Equation (2.56) yields a swept-up ISM mass of $M_{sa} = 2.6 \times 10^5$ $M_\odot$, as compared to $M_w = 5.1 \times 10^4$ $M_\odot$ in the 1450 yr needed for such an outflow to reach $R_2 = 12$ pc. The instantaneous kinetic luminosity of newly swept-up shocked ISM gas is

$$L_{gas,sa}(R_2) = \frac{1}{2}\dot{M}_{sa}v_{gas}^2(R_2) = \frac{9}{8}\pi\mu m_p n_0 R_0^\alpha R_2^{2-\alpha} v_{R2}^3, \tag{4.1}$$

where we have applied Equations (2.57), (2.59) and (2.80). For the above outflow, $v_{R2} = 5800$ km s^{-1}, $v_{gas}(R_2) = 4400$ km s^{-1}, $\dot{M}_{sa} = 320\tau_w^{(3-\alpha)/(5-\alpha)}$ $M_\odot$ yr^{-1} and $L_{gas,sa} = (1.9 \times 10^{45})\tau_w$ erg s^{-1}, which for $\tau_w = 1$ is 1.4% of the adopted bolometric luminosity of J0300. Of course, these quantities depend on more than just τ_w, but we quote the τ_w dependencies to compare them with $\dot{M}_w \propto \tau_w$ and $L_w \propto \tau_w$. The kinetic luminosity of the quasar wind in the above outflow is $L_w = 4.4 \times 10^{45}$ erg s^{-1} for $\tau_w = 1$, which is expected since approximately half the wind kinetic energy goes into the kinetic motion of the swept-up gas (W77, KM92, FGQ12; see also Section 2.1.4).

Choi et al. (2022) use their fitted N_H, R and v to infer an mass outflow rate in J0300 of $95(\Omega/0.2)$ $M_\odot$ yr^{-1} and a kinetic luminosity $L_{KE} = (1.7 \times 10^{45})(\Omega/0.2)$ erg s^{-1}, and a total outflowing mass of $M = 8.3 \times 10^4$ $(\Omega/0.2)$ $M_\odot$, where Ω is the fraction of 4π steradians covered by the outflow. Choi et al. (2022) assume a covering factor $\Omega = 0.2$; scaling to $\Omega = 1$ to match our comparison outflow, the Choi et al. (2022) parameters yield a 1.4× larger mass outflow rate, a 1.6× larger total mass, and a 3.6× larger kinetic luminosity than our values for $\tau_w = 1$, consistent with the larger value of v they use.

4.3.1 Searching for Matching Parameter Choices

We investigated whether the model could match the outflow properties inferred by Choi et al. (2022) for J0300; recall that we assume the gas absorbing in Ca II (primarily at $2000 < v < 4000$ km s^{-1}, but extending out to 6000 km s^{-1}) to share the velocity and

deceleration of the shocked ambient gas (in an adiabatic outflow) at $R_c < r < R_2$ due to having been condensed out of that gas (or, alternatively, having been accelerated to match its velocities).

To search for compatible parameters, we define the `J0300` filter (Table 2.2) using our acceleration constraint $-a_{post} < 0.1$ km s^{-1} yr^{-1} (Equation (2.87)), and the requirement that R_c, v_{Rc}, and L_{AGN} deviate from the values estimated by Choi et al. (2022) by no more than a factor of two:

$$d_{obs}^2 \equiv \left[\log\left(\frac{R_c}{12\text{pc}}\right)\right]^2 + \left[\log\left(\frac{v_{Rc}}{3000\ \text{km s}^{-1}}\right)\right]^2 + \left[\log\left(\frac{L_{AGN}}{10^{47.12}\ \text{erg s}^{-1}}\right)\right]^2 < [\log 2]^2. \tag{4.2}$$

We find that only $\sim 9\%$ of outflows that satisfy $d_{obs} < \log 2$ also satisfy $-a_{post} < 0.1$ km s^{-1} yr^{-1}, with a total of $\sim 0.14\%$ of all outflows meeting both requirements (though we remind the reader that this percentage reflects the assumed (log) uniform distribution of model parameters). Among the outflows in $\mathcal{X}$(`J0300`) we find a minimum $a_{post} = -0.013$ km s^{-1} yr^{-1} and a median $a_{post} = -0.081$ km s^{-1} yr^{-1}. Figure 4.1 below shows a cornerplot of model parameters and shell formation times derived from the filtered data. We do not show L_{AGN}, R_c or v_{Rc} in the cornerplot, since $a_{post} \propto a_{R2} \propto v_{R2}^2/R_2 \propto v_{Rc}^2/R_c$, and thus outflows which minimise the deceleration magnitude will tend to minimise v_{Rc} and maximise R_c. That being said, the comparison cases which most closely match $R_c = 12$ pc and $v_{Rc} = 3000$ km s^{-1} have $\log(t/\text{yr}) = 3.55 \pm 0.05$, $\tau_w < 0.1$ and $\alpha \simeq 0.8 \pm 0.1$, implying (e.g.) $n_0 \simeq 10^3$ cm^{-3} at $R_0 = 10$ pc. The free-free shell formation times are $t_{sf}^{FF} \sim 10^3$ yr in these cases (contrast this with the modal value of $\sim 10^{3.5}$ yr in the cornerplot).

Gas cooling is required to explain the fitted value of $n = 10^8$ cm^{-3} found by Choi et al. (2022) for the J0300 outflow. This density cannot be reached only through shock compression of preexisting ISM clouds, which have $n \sim 10^{2-3}$ cm^{-3} with rare cores reaching $n \sim 10^{4-6}$ cm^{-3} (Section III.B. of Ferrière 2001). Shock compression will only cause a

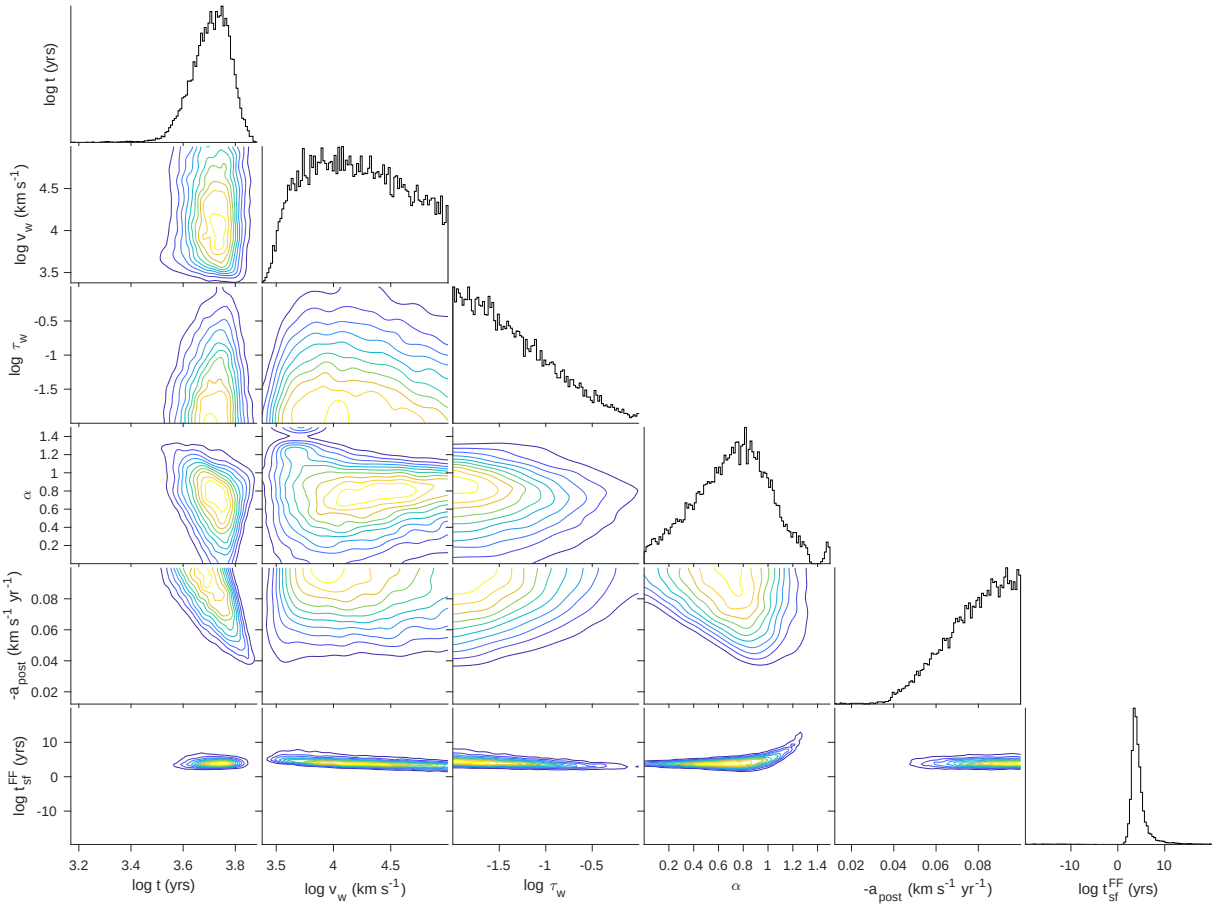

Figure 4.1: Cornerplot of the characteristics of J0300 candidates. The gap of data around $\alpha \sim 1.4$ is artificial, due to filtering out asymptotic values of t_{sf}^{FF} in order to show its distribution.

factor of four increase in gas density, and so any further significant density increase must come as a result of cooling and compression; noting that our comparison cases mostly satisfy $t \geqslant t_{sf}^{FF}$, density increases after shell collapse of up to a factor of 10^5 were found by Richings & Faucher-Giguère (2018a).

Overall, for our model in which the gas absorbing in Ca II is assumed to share the velocity and deceleration of the shocked ISM gas, we can find parameter choices that simultaneously match most of the observed and inferred properties of the J0300 outflow, with the exception of the density inferred by Choi et al. (2022). However, only a small subset of parameter choices matching some constraints match the rest. Given that and the fact discussed in Section 4.2 that the shocked ISM in our model lacks a sufficiently large velocity range to match the observations, we conclude that our initial model of Ca II absorption arising in the shocked ISM region of a self-similar outflow does not accurately represent the J0300 outflow. Nevertheless, outflow properties deduced from the model may prove informative and/or useful for comparative purposes.

4.3.2 Observed vs. Model Column Densities

In anticipation of the next section, we note that the time at which $R_2 = 12$ pc is $t = 1450$ yr for the parameters in the previous section (below Equation (4.2)), with the exception that we use $\tau_w = 1$ (and of course, $t = 10^{3.55}$ yr does not apply). The parameters can be used to calculate the swept-up ISM column density for this outflow at age 1450 yr from Equation (2.95); we find a total $\log(N_H/\mathrm{cm}^{-2}) = 22.21$, in good agreement with the Choi et al. (2022) fit value of $\log(N_H/\mathrm{cm}^{-2}) = 22.31$. For the column density through the shocked quasar wind, we find $\log(N_{sw}/\mathrm{cm}^{-2}) = 21.47$.

We can also check that our model predicts a total Ca II column density consistent with the values measured for this target in Hall et al. (2003): $N_{\mathrm{CaII}} = (7.1 \pm 1.1) \times 10^{14}$ cm^{-2} ($\log N = 14.85$) over $1697 < v < 5657$ km s^{-1}. The relative solar abundance of Ca is

$\log(\mathrm{Ca/H}) = -5.66$ (Asplund et al., 2009); we subtract that value from N_{CaII} to find the absolute lower limit of $\log N_H$ in the shocked ISM gas, $\log N_H = 20.51$. This is a lower limit mainly because only a small fraction of calcium will be in the Ca II ionisation stage even at high densities and column densities: for example, Rogerson et al. (2011) find a maximum Ca II ionisation fraction of $\sim 1\%$, suggesting $\log N_H \simeq 22.51$ as a more likely value – again in reasonable agreement with the estimate of Choi et al. (2022).

For the column density through the unshocked quasar wind N_w (Equation (2.93)), we find $\log(N_w/\mathrm{cm}^{-2}) = 22.78$ for $\tau_w = 1$. Note that the unshocked wind must be sufficiently ionised such that no absorption from it is seen at line-of-sight velocities it holds along our line of sight. The exact level of ionisation in the unshocked wind is not well constrained for J0300 because of the overlapping troughs shortward of rest-frame 2800 Å. The only transitions in which we might see absorption at high velocity are Ca II and Hβ. Ca II does not show evidence for any absorption at $v > 5700$ km s^{-1}, and the rest-frame optical spectrum shows strong Fe II emission but no sign of Hβ absorption (Figure 2 of Hall et al. 2003).

4.4 Acceleration of Preexisting ISM Clouds

It is possible that the velocity range of the low-ionisation BAL gas in J0300 is larger than our model predicts because our model does not account for the survival of sufficiently dense preexisting clouds of gas in the ISM. Such clouds will undergo a combination of acceleration and disruption (e.g., Faucher-Giguère et al. 2012, ZH+20). The gas in such clouds will require time to accelerate to the velocity of the surrounding shocked lower-density ISM, potentially resulting in some absorbing gas having lower velocities for a given outflow age than are predicted by our model.

Faucher-Giguère et al. (2012) show that FeLoBAL absorber properties can be explained by preexisting ISM clouds with the right physical properties shocked by a quasar

outflow. We define $n_{cl,i}$ and $n_0(r)$ as the initial cloud and surrounding ISM densities and we define their ratio as $\chi = n_{cl,i}/n_0(r)$. When a shock wave with velocity v_{R2} in the surrounding ISM overtakes a preexisting cloud at radius r, the shock speed inside the cloud, $v_{sh,cl}$, is lower by a factor $\chi^{1/2}$ and the post-shock temperature inside the cloud is lower by a factor χ: $T_{cl} = T_{gas}/\chi$, with $T_{gas} = 6 \times 10^8$ K $(v_{gas}/5000 \text{ km s}^{-1})^2$ (Faucher-Giguère et al. 2012 Equation 2).

The evolution of such clouds is governed by several timescales. Our discussion of these timescales below is based on that of Faucher-Giguère et al. (2012).

The cloud-crushing timescale t_{cc} for a cloud of radius r_{cl} is the time for the shock to travel r_{cl}:

$$\begin{aligned} t_{cc} &= \frac{r_{cl}}{v_{sh,cl}} = \frac{r_{cl}}{v_{R2}}\sqrt{\chi} = \frac{3r_{cl}}{4v_{gas}(r)}\sqrt{\chi} \\ &= 44 \text{ yr} \left[\frac{r_{cl}}{0.01 \text{ pc}}\right] \left[\frac{v_{gas}(r)}{5000 \text{ km s}^{-1}}\right]^{-1} \left[\frac{\chi}{900}\right]^{1/2} \end{aligned} \tag{4.3}$$

using $v_{gas} = 3v_{R2}/4$. Even neglecting ram pressure acceleration, after one cloud-crushing timescale we expect that the entire cloud has $n_{cl} = 4n_{cl,i}$ and is moving at least at velocity $v_{cl}(t_{cc}) = 0.75 v_{R2}\sqrt{\chi}$.

The cloud will be accelerated by ram pressure to roughly the speed of the hot gas on the timescale over which the (assumed spherical)[3] cloud intercepts a mass of hot gas equal to its initial mass:

$$\begin{aligned} t_{drag} &= \frac{\frac{4}{3}\pi r_{cl}^3 n_{cl,i}}{4n_0 \pi r_{cl}^2 v_{gas}(r)} = \frac{r_{cl}\chi}{3v_{gas}(r)} = \frac{4\sqrt{\chi}}{9} t_{cc} \\ &= 600 \text{ yr} \left[\frac{r_{cl}}{0.01 \text{ pc}}\right] \left[\frac{v_{gas}(r)}{5000 \text{ km s}^{-1}}\right]^{-1} \left[\frac{\chi}{900}\right]. \end{aligned} \tag{4.4}$$

[3]An oblate cloud will have a shorter t_{cc} and t_{drag} than a spherical cloud of equal mass and density. E.g., they are 3.2 and 3.5 times shorter, respectively, in the limit of a face-on disk-shaped cloud of diameter ten times its thickness.

A cloud which has not matched speeds with the hot gas is expected to be destroyed via the Kelvin-Helmholtz instability (due to velocity shear along the cloud-gas interface, e.g. D'Angelo 1965, Jones & Downes 2011) on a timescale

$$t_{\rm KH} = \frac{8}{3}\kappa_{\rm KH} t_{cc} \tag{4.5}$$

where $1 \lesssim \kappa_{\rm KH} \lesssim 10$. Greater post-shock cooling increases $\kappa_{\rm KH}$.

Finally, the post-shock cloud will cool on a timescale

$$t_{cool,cl} = 1.5 \times 10^4 \text{ yr } \left(\frac{T_{gas}/\chi}{10^6 \text{ K}}\right)^{1.6} \left(\frac{4n_{cl,i}}{10 \text{ cm}^{-3}}\right)^{-1} \tag{4.6}$$

(Equation 14 of Faucher-Giguère et al. 2012) where T_{gas} is the temperature of the surrounding shocked gas.

For preexisting clouds to end up visible as FeLoBAL absorbers containing relatively cool and low-ionisation gas, Faucher-Giguère et al. (2012) posit that they must match speeds with the hot gas before being disrupted ($t_{drag} < t_{\rm KH}$) and must cool by the time the shock passes through the cloud ($t_{cool,cl} < t_{cc}$), so that they leave cool material behind after their disruption.[4]

The requirement $t_{cool,cl} < t_{cc}$ yields a lower limit on the cloud hydrogen column density $N_{cl} = 2r_{cl}n_{cl,i}$ (Faucher-Giguère et al. 2012 Equation 15) for clouds to survive:

$$N_{cl} \gtrsim 1.4 \times 10^{20} \text{ cm}^{-2} \left(\frac{v_{gas}(r)}{5000 \text{ km s}^{-1}}\right)^{4.2} \left(\frac{\chi}{900}\right)^{-2.1}. \tag{4.7}$$

That is, a factor of two increase in wind velocity will result in clouds a factor of sixteen higher in column density not cooling before disruption, unless the clouds also have at least

[4]Note that Gronke & Oh (2018, 2020) find that sufficiently large clouds ($r_{cl} \gtrsim 2$ pc) can mix their cool gas with entrained hot gas which cools and enables the clouds to survive, accelerate, and grow as elongated structures with a range of densities (their Figure 2).

a factor of four higher relative density. The Choi et al. (2022) fit value of $\log N_H = 22.31$ and the observed values of $v_{gas} = 3000 \pm 1000$ km s^{-1} imply a range of $\chi > 30^{+24}_{-16}$ to satisfy the predicted column density lower limit for J0300.

Faucher-Giguère et al. (2012) assume that the original clouds will eventually fragment into cloudlets comoving and in pressure equilibrium with the hot gas at temperatures $T_{cl} \simeq 10^4$ K and densities

$$n \simeq 3000 \text{ cm}^{-3} \left(\frac{n_0(r)}{0.02 \text{ cm}^{-3}} \right) \left(\frac{v_{gas}}{5000 \text{ km s}^{-1}} \right)^2 . \tag{4.8}$$

Note that our comparison model of J0300 satisfies that prediction for $T_{cl} \simeq 10^4$ K with $n = 10^8$ cm^{-3}, $n_0 = 10^3$ cm^{-3}, and $v_{gas} = 4400$ km s^{-1}. Our comparison model has $n_0 = 10^3$ cm^{-3} and $T_{gas} = 4.6 \times 10^8$ K, so pressure equilibrium with a cloud of density $n = 10^8$ cm^{-3} would be achieved at $T_{cl} = 4600$ K.

The requirement $t_{drag} < t_{\rm KH}$ yields an upper limit on $\chi = \frac{n_{cl,i}}{n_0(r)}$, because clouds that are sufficiently denser than their surroundings will be disrupted before they reach the hot gas velocity. However, as pointed out by Hopkins & Elvis (2010), shocked clouds expand laterally and increase their effective area for ram pressure acceleration (their Figure 1). In the limit of a cloud that deforms its shape at constant density and increases its lateral radius by a factor of f_r in time $t_{\rm KH}$ and therefore decreases its t_{drag} by a factor of f_r^2, the values of χ that produce $t_{drag} < t_{\rm KH}$ are

$$\chi \lesssim 36 \kappa_{\rm KH}^2 f_r^2 \quad \text{or} \quad \chi \lesssim (36 - 3600) f_r^2 . \tag{4.9}$$

A cloud with any value of χ that maintains that χ while increasing its lateral radius by a factor of $f_r > \sqrt{\chi^{0.5}/6\kappa_{\rm KH}}$ in time $t_{\rm KH}$ will satisfy $t_{drag} < t_{\rm KH}$. A cloud expanding laterally at a fraction f_v of the shock speed inside the cloud will reach that value of f_r for $\chi < 1800 f_v \kappa_{\rm KH}^6$; i.e., $\chi < 1.8 f_v \times (10^3 - 10^9)$. That weak constraint suggests it is possible

that clouds will expand and match speeds with the hot gas before being disrupted.

More recently, ZH+20 have simulated in 2-D the interaction between a preexisting cloud of size $\sim$ 1 pc and $n_{cl,i} = 10^6$ cm^{-3} embedded in gas of density $n_0 = 2.5$ cm^{-3} (yielding $\chi = 4 \times 10^5$) with a quasar wind of kinetic luminosity 10^{47} erg s^{-1}, density $\simeq 10$ cm^{-3} (their Figure 2), and velocity 30,000 km s^{-1}. Although this is a larger velocity contrast between the cloud and the surrounding flow than assumed in our model, in their simulation a bow shock forms between the cloud from the wind and decelerates gas in the wind to $3000 \lesssim v \lesssim 9000$ km s^{-1} in the immediate environs of the cloud (M. Zeilig-Hess, personal communication).

The cloud studied in ZH+20's simulation fragments into cloudlets of size $\sim 0.01 - 0.10$ pc (0.03 pc on average, with a resolution limit of 0.01 pc; their Figure 6) by time $\sim 4t_{cc}$ (65,000 yr; their Figure 2). By that time the distribution of cloudlets has expanded laterally by a factor $\simeq 5 - 10$ beyond the initial size of the cloud, although this expansion has occurred simultaneous with the cloud's disruption instead of preventing it. They identify these cloudlets as producing BAL troughs with significant velocity structure in their Figure 8.

The cloudlets have lower densities than the original cloud, though this is partly due to an artificial limit on achieving high densities through cooling (the simulation has a floor temperature of 3×10^5 K). With smaller sizes and lower densities, t_{drag} for the cloudlets is less than or equal to $2t_{cc}$ for the cloud as given by Equation 4.3,[5] so the cloudlets can accelerate on the timescale on which they are produced. By a time $t = 4t_{cc}$ for $r_{cl} = 1$ pc in the simulation ($t = 65,000$ yr), most cloudlets have accelerated to velocities 1000 km s^{-1} to 3000 km s^{-1}, with "much slower" acceleration at later times (their Section 3.2 and Figure 4) and "somewhat smaller" velocities in a simulation with wind velocity 9,000 km s^{-1} instead of 30,000 km s^{-1}. Note that the cloudlets in ZH+20's simulations achieve essentially terminal velocities which are smaller than the flow in which they are

[5] ZH+20 define t_{cc} to be twice the value we use.

embedded by a factor of ∼3.

In summary, it is reasonable to expect that a combination of lateral expansion and acceleration of cloud fragments (cloudlets) can result in cool gas surviving acceleration to be seen at velocities of thousands of km s^{-1}. Fragmentation of clouds into cool cloudlets with a range of bulk velocities can explain the velocity structure of multiple narrow absorption features over a wide range of velocities seen in some BAL outflows such as the Ca II outflow of J0300.

4.4.1 Comparison to the J0300 Acceleration Upper Limit

We now explore further whether the acceleration of preexisting ISM clouds can explain our observations of J0300. We discuss parameter value combinations that would produce ram pressure acceleration below our observed acceleration upper limit. We estimate various timescales for the gas clouds and compare them to the age of the outflow inferred to exist in J0300. Finally, we estimate the velocities that swept-up gas could have when it exits the shocked-ambient-medium region of the shock bubble.

The parameters of our comparison model of J0300 are summarised in Table 4.1. Observationally inferred parameters are taken from Choi et al. (2022). Observational comparison parameters, assumed parameters, and resultant parameters are discussed in Section 4.3, Section 4.3.1, and in this section. As mentioned in Section 4.3.2, the age at which our comparison model of J0300 has reached $R_2 = 12$ pc is $t = 1450$ yr, noting that we assume $\tau_w = 1$ despite most comparison cases having $\tau_w < 0.1$.

First, we estimate a value of r_{cl} for cloudlets observed in J0300 (which may or may not be the same size as the original clouds). This value must be comparable to or smaller than the size of the continuum-emitting region at 3900 Å rest frame, since the Ca II absorption covers $\sim 30\%-90\%$ of that region (Figure 6 of Hall et al. 2003). For a radiative efficiency $\eta_r = 0.175$, the predicted half-light radius of the emission region at 3900 Å in J0300 is

J0300 Comparison Model Outflow Parameters

	Observationally Inferred Parameters	
L_{AGN}	bolometric luminosity	$10^{47.12}$ erg s^{-1}
R_2	outer shock radius	12.0 pc
n_{cl}	final cloud # density	10^8 cm^{-3}
	Observational Comparison Parameters	
α	ISM density power law exponent	0.8
R_0	ISM density reference radius	10 pc
n_0	ISM H nucleus # density at R_0	10^3 cm^{-3}
v_w	wind launch velocity	20,000 km s^{-1}
τ_w	wind optical depth	1
	Assumed Parameters	
M_{BH}	black hole mass	3×10^9 $M_\odot$
η_r	accretion disk radiative efficiency	0.175
r_{cl}	cloud radius	0.005 pc
χ	initial cloud overdensity	$10^4 - 10^5$
	Resultant Parameters	
λ_c	ratio R_c/R_2	0.854
R_f	outflow free expansion radius	0.52 pc
t_f	outflow free expansion time	25 yr
t	outflow age	1450 yr
R_1	wind shock radius	7.62 pc
R_c	contact discontinuity radius	10.3 pc
t_{csa}	shocked ambient medium crossing time	360 yr
$v_{gas}(R_2)$	gas velocity at R_2	4400 km s^{-1}
T_{gas}	shocked ISM temperature at R_2	4.6×10^8 K
t_{cc}	cloud crushing time	$80 - 270$ yr
$t_{\rm KH}$	cloud disruption time ($\tau_{\rm KH} = 10$)	$2200 - 7100$ yr
t_{drag}	cloud drag time	$3800 - 38,000$ yr

Table 4.1: Parameters for our model of the outflow in J0300. Note that in the text we also explore results for larger values of r_{cl} and smaller values of χ.

0.005 pc (Blackburne et al., 2015). We therefore adopt a cloudlet radius of 0.005 pc.

Microlensing studies indicate that quasars may have half-light radii a factor of ~ 4 larger than predicted by thin disk theory (Hall et al., 2014). That sets either an upper limit on the individual cloud size or a requirement that more than one cloudlet is present at most velocities. On the other hand, the cold outflowing gas could reside in a 'mist' of even smaller cloudlets: McCourt et al. (2017) find a minimum cold gas length scale $\ell_{\rm shatter} = c_{s,cl} t_{cool,cl}$, where $c_{s,cl}$ is the speed of sound in the cloud; cloudlets of this length scale or smaller do not shatter further. This length scale is only 500 km for gas with $n = 10^8$ cm^{-3} and $T = 10^4$ K.

For comparison with our results, the ram pressure acceleration expected for a stationary cloud (in the rest of this section we do not need to distinguish between clouds and cloudlets) of radius r_{cl} surrounded by shocked ambient gas moving at velocity $v_{gas}(r)$ is given by

$$\begin{aligned} a_{ram} &= \frac{v_{gas}(r)}{t_{drag}} \\ &= 8.3 \text{ km s}^{-1} \text{ yr}^{-1} \\ &\times \left[\frac{v_{gas}(r)}{5000 \text{ km s}^{-1}}\right]^2 \left[\frac{0.01 \text{ pc}}{r_{cl}}\right] \left[\frac{900}{\chi}\right]. \end{aligned} \tag{4.10}$$

For a cloud moving with velocity v_{cl}, the above becomes $a_{ram} \propto (\Delta v)^2$, where $\Delta v = v_{gas}(r) - v_{cl}$.

For ram pressure acceleration to lie below a given acceleration upper limit requires

$$\Delta v < 1740 \left[\frac{a_{ram}}{1 \text{ km s}^{-1} \text{ yr}^{-1}} \frac{r_{cl}}{0.01 \text{ pc}} \frac{\chi}{900}\right]^{1/2} \text{ km s}^{-1}. \tag{4.11}$$

In our case, assuming gas clouds that originated with $n = 10^8$ cm^{-3}, we have a most likely value in the range $10^4 \lesssim \chi \lesssim 10^5$ (Section 4.3.1). To match our observed limit of $|a| < 0.1$ km s^{-1} yr^{-1} requires $\Delta v < 4100$ km s^{-1} for $r_{cl} = 0.005$ pc and $\chi = 10^5$. This is

not a particularly useful constraint, but it does confirm that sufficiently dense gas clouds can be effectively coasting even when surrounded by fast-moving gas. The disruption timescale for such a cloud would be $t_{\rm KH} > (750 - 7500)$ yr. Such clouds are unlikely to have been fully disrupted yet in this young outflow, though that will likely happen eventually and partial disruption can occur in the meantime (e.g., ZH+20 Figure 2, top right and bottom left panels).

In our comparison model of J0300, assuming $r_{cl} = 0.005\,$pc and $\chi = 10^5$ yields $t_{cc} = 270$ yr, $t_{\rm KH} = 710-7100$ yr, and $t_{drag} = (3.8\times10^4) f_r^{-2}$ yr. If such a cloud undergoes lateral expansion by a factor of at least $f_r = 2-7$ in radius, then it will have $t_{drag} \leqslant t_{\rm KH}$. However, the drag time for $10^4 \lesssim \chi \lesssim 10^5$ is much greater than the age of the outflow, meaning that the clouds in J0300 could not have been accelerated to their observed speeds at their inferred densities and distance. Increasing v_w cannot alleviate this problem because in such cases the time needed for the outflow to reach 12 pc decreases by the same factor by which $v_{gas}(R_2)$ increases and the above timescales decrease, meaning that the drag time remains long relative to the age of the outflow.

For swept-up ISM clouds to have survived to cause Ca II absorption in J0300 at a distance of 12 pc from the central black hole, they must have begun accelerating as clouds with low χ before reaching their observed velocities, their low observed accelerations, and their inferred large χ_{cl}, where χ_{cl} is the instantaneous overdensity of the cloud. For the clouds considered above, $t_{cool,cl} < 1$ yr, so cooling and contraction can reasonably increase the clouds' overdensities relative to their surroundings. Note that gas clouds of constant mass which contract by a factor of g_r in radius will have larger $\chi_{cl} \propto g_r^{-3}$, longer $t_{\rm KH} \propto g_r^{-1/2}$, and longer $t_{drag} \propto g_r^{-2}$.

Note that it would be possible for preexisting clouds of density $n \sim 10^8$ cm^{-3} to reach the velocities observed in J0300 if the outflow is older than we infer, with age $t \simeq t_{drag} \simeq 3800 - 38,000$ yr. In that scenario the clouds are located at 12 pc but

the outer edge of the shock bubble is located much farther away. The only potential origin for such dense clouds would be the quasar accretion disk because the highest ISM density observed outside of AGN accretion disks is only $\simeq 10^5\,\mathrm{cm}^{-3}$ (Hopkins & Quataert, 2010) and even proto-stellar cores in molecular clouds only reach gas-phase densities of $\simeq 10^7\,\mathrm{cm}^{-3}$ (di Francesco et al., 2007).

4.4.2 Acceleration in the Shocked Ambient Medium Region

Following on the results above, we explore a few parameter combinations including smaller χ (by at least an order of magnitude) that might make it possible for the Ca II-absorbing gas to have been accelerated to its observed velocities during its passage through the shocked ambient medium region of our model outflow. After that time, the ram pressure acceleration will drop due to the lower density in the shocked-wind region.

We define the shocked-ambient-medium crossing time as the time required for the shocked-ambient-medium part of the outflow to cross a given fixed radius in space: $t_{csa} = t_2 - t_1$, where we find t_2 and t_1 by solving

$$R_2(t_1) = A_E t_1^{\beta_E} = \lambda_c A_E t_2^{\beta_E} = R_c(t_2) \tag{4.12}$$

which yields $t_2 = t_1 \lambda_c^{-1/\beta_E}$. For $\alpha = 0.8$, $\beta = 5/7$ and $\lambda_c = 0.854$ so $t_2 = 1.25 t_1$ and $t_{csa} = 0.25 t_1$. This is the length of time that preexisting gas which does not experience significant ram pressure acceleration will spend in the shocked ambient medium region of the outflow after entering the outflow at time t_1. For our model outflow at age $t_2 = 1450$ yr, $t_{csa} = 360$ yr.

We have estimated the terminal velocities of gas clouds after their passage through the shocked ambient medium region of our model for the J0300 outflow. We launch clouds at $r = R_2(t)$ and $v_{cl} = 0$ at several different times t and in each case recalculate a_{ram}, v_{cl}, and r in timesteps of one year until we reach a time t' when $r(t') = R_c(t')$. We thus

account for the motion of the clouds in radius due to their acceleration in that region but we neglect acceleration in the shocked wind region.[6] We find that gas clouds of fixed size and overdensity swept up at the smallest radii generally end up at smaller velocities. At earlier times, the ram pressure acceleration is larger but the time spent undergoing acceleration is much less, so the final cloud velocity is lower.

For $r_{cl} = 0.005$ pc and $\chi = 900$, we obtain a velocity range from 700 $\mathrm{km\,s^{-1}}$ for gas swept up at $t = t_f = 25$ yr to 2000 ± 400 $\mathrm{km\,s^{-1}}$ for gas swept up at $t \geqslant 200$ yr; note that $t_{\mathrm{KH}} = 670$ yr for such clouds. For even smaller clouds with $r_{cl} = 0.0015$ pc but still $\chi = 900$, we obtain a velocity range from 1700 $\mathrm{km\,s^{-1}}$ for gas swept up at $t = 25$ yr to 4000 ± 200 $\mathrm{km\,s^{-1}}$ for gas swept up at $t \geqslant 200$ yr; note that $t_{\mathrm{KH}} = 200$ yr for such clouds. For larger and less overdense clouds with $r_{cl} = 0.01$ pc and $\chi = 90$, we obtain a velocity range from 3000 $\mathrm{km\,s^{-1}}$ for gas swept up at $t = 25$ yr to $4900 - 4200$ $\mathrm{km\,s^{-1}}$ for gas swept up at $t \geqslant 200$ yr; note that $t_{\mathrm{KH}} = 320$ yr for such clouds. For those parameters, clouds swept up earlier have higher terminal velocities due to being accelerated by higher-velocity shocked ISM when the outflow was younger. Such clouds swept up at $t = 800$ yr only pass through the contact discontinuity at $t \simeq 1430$ yr, meaning that such gas clouds from $\sim$70% of the volume swept up by the outflow would be located between $R_c = 0.854 R_2$ and R_2 when the outflow is 1450 yr old. Such clouds will survive for a time t_{KH} before being disrupted, but cloudlets produced by the cloud's disruption can survive long after that if they are in pressure equilibrium with the surrounding gas.

In summary, the velocity range seen in Ca II in J0300 is potentially consistent with the velocities of cloudlets formed out of some swept-up clouds from the ISM. The terminal velocity, current velocity, and current radius of a cloudlet will depend on its initial size, initial overdensity, and the time when its parent cloud was swept up. Thus, a one-to-one

[6] Acceleration in the shocked wind region may be significant for clouds swept up at early times, when the density in that region is highest. The timescale for evaporation in that region is $t > 3000$ yr for $r_{cl} > 0.0015$ pc (Equation 6 of Faucher-Giguère et al. 2012).

relation between observed velocity and current radius is not expected. It is also worth emphasizing that not all clouds swept up by a quasar outflow will produce cool cloudlets moving at high velocity, nor will all the gas in clouds that do produce cloudlets end up in them.

4.5 Closing Remarks

Here we have shown that the observed velocity range of Ca II absorbing gas rules out our initial model that the Ca II is part of the bulk flow in the shocked ISM, but that otherwise the shocked ISM column densities are consistent with the results of Hall et al. (2003) and Choi et al. (2022).

We further investigated the possibility that ram pressure acceleration of clouds in the ambient ISM could explain the observed velocity range, and showed that for clouds at the absorber densities inferred by Choi et al. (2022) could only have accelerated to their observed speeds if they were less dense at the time of acceleration, before cooling and becoming more dense. Dense clouds can still be effectively coasting even when surrounded by gas moving at larger relative velocities though, and estimating the acceleration of clouds in the shocked ambient region (Section 4.4.2) led us to conclude that the velocity range seen in J0300's Ca II absorption is potentially consistent with a velocity profile arising from the disruption of ISM clouds by a blast wave.

5 Conclusions

In this thesis we have presented an expanded spherical blast wave model for quasar accretion disk winds, build on the methods of W77 and KM92, for the case of constant mass injection ($\eta_{in} = 1$, Equation (2.40)). We then explored the resultant model's ability to explain the absorption troughs of low-ionisation absorbers with sub-Rydberg ionisation

potentials (e.g. Ca II), as seen in some BAL quasars.

For the extended model, we have:

- Condensed KM92's methods of analysis for intermediate phase outflows to allow for easy adaptation of different cooling mechanisms to the model (Section 2.1.2.3). We then demonstrated the implications of free-free cooling and FGQ12's two-temperature plasma (TTP) cooling in terms of self-similarity parameters, stability, evolution, energy/momentum coupling and shocked ISM shell formation (Sections 2.1.2 through 2.1.4 and 2.2.1).

- Demonstrated a correspondence between the phase transition conditions in the intermediate phase, the steady phases of evolution, the hierarchy of late-time self-similarity exponents β and the increasing or decreasing (or stationary) nature of the intermediate-phase energy and momentum coupling factors $\mathcal{E}_I$ and $\mathcal{B}_I$.

- Produced plots showing the parameter space distribution, under a uniform and log-uniform random prior, of initial phases (Sections 2.1.3.1 and 2.1.3.6) and phase transition times for the TTP cooling regime, as well as the distribution of shell formation times (Section 2.2.1) for free-free cooling;

- Provided general expressions for the energy and momentum coupling between the wind and the swept-up ISM (Section 2.1.4), the trajectories of the blast wave shock features (Section 2.2.2) and, for the case of adiabatic outflows, profiles of potentially observable properties (velocity, acceleration, density, column density) for the gas bounded by the shocks (Section 2.2.3);

- Provided plots of the above trajectories and profiles for a fiducial case.

We measured the bulk velocity shift (and in turn acceleration) of the strong Ca II absorber system in the iron low-ionisation (FeLoBAL) quasar SDSS J030000.56+004828.0

(J0300) by cross-correlating the broad absorption troughs of the H and K lines from new and previous high-resolution spectra (Section 3), then compared the measured acceleration to the deceleration predicted by the model (Section 4.3). We placed a strong 3σ upper limit of $|a| < 0.1$ km s^{-1} yr^{-1} (3×10^{-4} cm s^{-2}) on the average (quasar rest-frame) bulk deceleration or acceleration of the system, over a period of 9.65 rest-frame years. In conjunction with the results of Choi et al. (2022), this upper limit allowed us to place plausible constraints on the outflow properties, however the model is excluded by the observed Ca II velocity range (a factor of ~ 2 to 3.3) due to fundamental model limitations, which restrict us to a factor of ~ 1.13 to 1.15 (Section 4.2). Despite this limitation, the other plausible parameters obtained make the model useful for exploring the origin of the Ca II absorption, and may prove useful if similarly analysing other FeLoBAL quasars with narrow absorption features.

We then investigated whether the ram pressure acceleration and potential disruption of preexisting ISM clouds could explain our observations of J0300, noting the similar absorption profiles obtained from the simulations of Zeilig-Hess et al. (2020), and found that based on the densities obtained by Choi et al. (2022), clouds at those densities could only have accelerated to their observed speeds if they were less dense at the time of acceleration, before cooling and becoming more dense; however, dense clouds can still be effectively coasting even when surrounded by gas moving at larger relative velocities (Section 4.4.1). Estimating the acceleration of clouds in the shocked ambient region (Section 4.4.2), we concluded that the velocity range seen in J0300's Ca II absorption is potentially consistent with a velocity profile arising from the disruption of ISM clouds by a blast wave. The terminal and current velocity/radius of these cloudlets will depend on the time the parent cloud was impacted, along with its initial size and overdensity.

5.1 Future Directions

With regards to our combined model, we demonstrated that the KM92's analysis of the shocked wind region breaks down in the case of intermediate-phase outflows, due to the approximation that the pressure at the contact discontinuity is roughly constant and equal to the mean pressure of the nearby gas in the region. This approximation is also used in KM92's derivation of the intermediate-phase equations, and thus a more self-consistent model of the shocked wind for this phase may alter the phase equations (i.e. the self-similarity parameters β and A) altogether. Furthermore, an extension of TTP cooling to the shocked ISM may delay the collapse of the region (i.e. increase t_{sf}) in adiabatic outflows at low α, in the same way TTP cooling in the shocked wind allows for outflows to be initially adiabatic for many parameter combinations. Our model of the low-ionisation absorbing gas in BAL outflows sharing the velocity and deceleration of shocked ISM gas, with higher-velocity gas located closer to the quasar, cannot match all parameters of the J0300 outflow but it may still match other BAL quasar outflows.

In addition to considering clouds forming at the velocities of swept-up gas, explaining the range of velocities of low-ionisation absorption in BAL quasars requires considering the possible acceleration of preexisting gas clouds; more detailed simulations similar to those of Zeilig-Hess et al. (2020) would be helpful in this regard. For J0300 specifically, a more refined picture of the outflow may result from refining the *SimBAL* modeling of Choi et al. (2022) to better match the distinct inferred physical conditions and observed velocities for Fe II* and Ca II and other ions in its high-resolution spectrum, including allowing a density jump at the hydrogen ionisation front (Leighly et al., 2014). Finally, note that if acceleration of preexisting clouds is significant in low-ionisation quasar outflows, then we expect observable accelerations only at times $t \lesssim t_{drag}$ after the clouds enter the shock bubble, after which the clouds will be coasting. Thus, if clouds survive for a long time in their coasting phase, then the fraction of low-ionisation outflows with observable

acceleration might be small even if such acceleration happens in all of them.

Bibliography

Allen J. T., Hewett P. C., Maddox N., Richards G. T., Belokurov V., 2011, MNRAS, 410, 860

Arav N., Korista K. T., de Kool M., Junkkarinen V. T., Begelman M. C., 1999, ApJ, 516, 27

Arav N., Liu G., Xu X., Stidham J., Benn C., Chamberlain C., 2018, Astrophys. J., 857, 60

Asplund M., Grevesse N., Sauval A. J., Scott P., 2009, Annu. Rev. Astron. Astrophys., 47, 481

Barenblatt G. I., Zel'dovich Y. B., 1972, Annual Review of Fluid Mechanics, 4, 285

Bautista M. A., Dunn J. P., 2010, Astrophys. J. Lett., 717, L98

Blackburne J. A., Kochanek C. S., Chen B., Dai X., Chartas G., 2015, Astrophys. J., 798, 95

Cavaliere A., Lapi A., Menci N., 2002, Astrophys. J. Lett., 581, L1

Chao J. K., Wiskerchen M. J., 1974, Journal of Geophysical Research (1896-1977), 79, 4769

Chene A.-N., et al., 2014, SPIE Conference Series. SPIE, p. 915147, doi:10.1117/12.2057417

Choi H., Leighly K. M., Terndrup D. M., Dabbieri C., Gallagher S. C., Richards G. T., 2022, Astrophys. J., 937, 74

D'Angelo N., 1965, Physics of Fluids, 8, 1748

Di Matteo T., Springel V., Hernquist L., 2005, Nature, 433, 604

Donati J. F., Semel M., Carter B. D., Rees D. E., Collier Cameron A., 1997, MNRAS, 291, 658

Donati J. F., Catala C., Landstreet J. D., Petit P., 2006, ESPaDOnS: The New Generation Stellar Spectro-Polarimeter. Performances and First Results. San Francisco: ASP, p. 362

Falle S. A. E. G., 1975a, Astron. Astrophys., 43, 323

Falle S. A. E. G., 1975b, MNRAS, 172, 55

Faucher-Giguère C.-A., Quataert E., 2012, MNRAS, 425, 605

Faucher-Giguère C.-A., Quataert E., Murray N., 2012, MNRAS, 420, 1347

Ferrarese L., Merritt D., 2000, Astrophys. J. Lett., 539, L9

Ferreira L. C. F., Furtado M. F., Medeiros E. S., 2015, Calculus of Variations and Partial Differential Equations, 54, 4065

Ferrière K. M., 2001, Reviews of Modern Physics, 73, 1031

Gebhardt K., et al., 2000, Astrophys. J. Lett., 539, L13

Giustini M., Proga D., 2019, Astron. Astrophys., 630, A94

Gronke M., Oh S. P., 2018, MNRAS, 480, L111

Gronke M., Oh S. P., 2020, MNRAS, 492, 1970

Hall P. B., et al., 2002, ApJS, 141, 267

Hall P. B., Hutsemékers D., Anderson S. F., Brinkmann J., Fan X., Schneider D. P., York D. G., 2003, ApJ, 593, 189

Hall P. B., Noordeh E. S., Chajet L. S., Weiss E., Nixon C. J., 2014, MNRAS, 442, 1090

Hamann F., Herbst H., Paris I., Capellupo D., 2019, MNRAS, 483, 1808

Hopkins P. F., Elvis M., 2010, MNRAS, 401, 7

Hopkins P. F., Quataert E., 2010, MNRAS, 407, 1529

Hopkins P. F., Torrey P., Faucher-Giguère C.-A., Quataert E., Murray N., 2016, MNRAS, 458, 816

Ikeuchi S., 1981, Publ. Astron. Soc. Jpn., 33, 211

Jones A. C., Downes T. P., 2011, MNRAS, 418, 390

Kahn F. D., 1976, Astron. Astrophys., 50, 145

King A., 2003, Astrophys. J. Lett., 596, L27

King A., Pounds K., 2015, Annu. Rev. Astron. Astrophys., 53, 115

King A. R., Zubovas K., Power C., 2011, MNRAS, 415, L6

Koo B.-C., McKee C. F., 1992, Astrophys. J., 388, 103 (KM92)

Lanzuisi G., Giustini M., Cappi M., Dadina M., Malaguti G., Vignali C., Chartas G., 2012, Astron. Astrophys., 544, A2

Larson R. B., 1969, MNRAS, 145, 271

Leighly K. M., Terndrup D. M., Baron E., Lucy A. B., Dietrich M., Gallagher S. C., 2014, Astrophys. J., 788, 123

Leighly K. M., Terndrup D. M., Gallagher S. C., Richards G. T., Dietrich M., 2018, Astrophys. J., 866, 7

Livescu D., 2004, Physics of Fluids, 16, 118

Martioli E., Teeple D., Manset N., Devost D., Withington K., Venne A., Tannock M., 2012, SPIE Conference Series. SPIE, p. 84512B, doi:10.1117/12.926627

Mayer M., 2007, Astron. Astrophys., 461, 381

McCourt M., Oh S. P., O'Leary R., Madigan A.-M., 2017, MNRAS, 473, 5407

Morton D. C., 1991, ApJS, 77, 119

Murphy M. T., Kacprzak G. G., Savorgnan G. A. D., Carswell R. F., 2019, MNRAS, 482, 3458

Murray N., Chiang J., Grossman S. A., Voit G. M., 1995, ApJ, 451, 498

Navarro J. F., Frenk C. S., White S. D. M., 1996, Astrophys. J., 462, 563

Proga D., Stone J. M., Kallman T. R., 2000, Astrophys. J., 543, 686

Rafiee A., Hall P. B., 2011, ApJS, 194, 42

Ribeyre X., Tikhonchuk V. T., Bouquet S., 2004, Physics of Fluids, 16, 4661

Richings A. J., Faucher-Giguère C.-A., 2018a, MNRAS, 474, 3673

Richings A. J., Faucher-Giguère C.-A., 2018b, MNRAS, 478, 3100

Rogerson J. A., Hall P. B., Snedden S. A., Brotherton M. S., Anderson S. F., 2011, New Astronomy, 16, 128

Sazonov S. Y., Ostriker J. P., Sunyaev R. A., 2004, MNRAS, 347, 144

Sedov L. I., 1946, Journal of Applied Mathematics and Mechanics, 10, 241

Shu F. H., 1977, Astrophys. J., 214, 488

Silk J., Rees M. J., 1998, Astron. Astrophys., 331, L1

Spitzer L., 1962, Physics of Fully Ionized Gases. Interscience Publishers

Taylor G. I., 1950a, Proceedings of the Royal Society of London. Series A. Mathematical and Physical Sciences, 201, 159

Taylor G., 1950b, Proceedings of the Royal Society of London. Series A, Mathematical and Physical Sciences, 201, 192

Tonry J., Davis M., 1979, Astron. J., 84, 1511

Vayner A., et al., 2021, Astrophys. J., 919, 122

Weaver R., McCray R., Castor J., Shapiro P., Moore R., 1977, Astrophys. J., 218, 377 (W77)

Weymann R. J., Morris S. L., Foltz C. B., Hewett P. C., 1991, ApJ, 373, 23

Yao Z., Gan Z., 2020, MNRAS, 492, 444

Zeilig-Hess M., Levinson A., Nakar E., 2019, Monthly Notices of the Royal Astronomical Society, 482, 4642

Zeilig-Hess M., Levinson A., Xu X., Arav N., 2020, MNRAS, 491, 4325

Zubovas K., King A., 2012, Astrophys. J. Lett., 745, L34

di Francesco J., Evans II N. J., Caselli P., Myers P. C., Shirley Y., Aikawa Y., Tafalla M., 2007, Protostars and Planets V, pp 17–32

A Appendix A: Data Visualisation and Analysis with D&R Mapping

This section outlines a simple data visualisation/analysis method developed over the course of this work and used throughout, dubbed *D&R mapping* (or more casually, *D&R maps*). It involves the use of two kinds of heatmap plots, respectively dubbed *density maps (D-maps)* and *representation maps (R-maps)*. A D-map is often presented with a set of R-maps, and so the terms *D&R map set* and *D&R mapping* are frequently used to describe such a combination. To qualitatively summarise the method: given some data, we make a D-map, a heatmap-histogram of the data with respect to two of its features (the *main features)*. We then bin the data into "bands" with respect to some third feature (the *band feature* – named in analogy to bandpass filtering) and make an R-map for each band, a heatmap showing how the data in the band is represented in the D-map (by comparing the histogram of the band-filtered data to the D-map histogram). The resulting set of R-maps show the qualitative trend in the D-map with respect to the band feature, and can be used for other purposes as well, such as looking for regions of feature space where data is or isn't represented. However, it is important to note that D&R mapping is first and foremost a tool for *qualitative* analysis. Quantitative trend analysis is possible, but care must be taken when doing so; this is discussed in more detail in Section A.5.

A.1 Notation

Here we introduce notation to help condense the various aspects of D&R mapping for easier navigation; throughout this appendix we use $\mathbb{D}$ to refer to a D-map and $\mathbb{R}$ to refer to an R-map. As mentioned in the introductory paragraph above, D-maps are in essence histograms of a dataset with respect to two features (θ_x, θ_y), the main features. R-maps then show the representation of the data, restricted to some range of the domain of another

feature θ_z, the band feature. D-maps and R-maps are formally defined in Sections A.2 and A.3, and a toy example is presented in Section.

As described in Section 2.0.2, we generate a master dataset $\mathcal{X}$ in order to analyse quasar outflow shock structure models using D&R maps. Notationally, the general D&R mapping procedure with respect to $\mathcal{X}$ is as follows: first, a D-map $\mathbb{D}_0$ is made for some pre-filtered subset $\mathcal{X}_0 \subseteq \mathcal{X}$ (possibly $\mathcal{X}$ itself). A set of R-maps are then made for this D-map by further filtering $\mathcal{X}_0$ into multiple band subsets $\mathcal{X}_b \subseteq \mathcal{X}_0$, each of which yields a corresponding R-map $\mathbb{R}_b$. To be able to easily reference D&R maps throughout this work, we refer to a D&R map set of $\mathcal{X}_0$ with x-axis main feature θ_x, y-axis main feature θ_y and band feature θ_z as *"a D&R mapping of* $(\mathcal{X}_0 : \theta_x, \theta_y, \theta_z)$*"*, which reads as "*a D&R mapping of* $\mathcal{X}_0$ *with respect to main features* (θ_x, θ_y) *and band feature* θ_z". We emphasise that this is *a* D&R map set and not *the* D&R map set of $\mathcal{X}_0$, as different map sets can be produced using the same main/band features, but with different binning schemes.

In this work, we use uniform binning across the domains of the main features, and include a set of explanatory values (Σ, M, P, x, y) in the D&R map subplot titles. Here, x and y simply refer to the number of θ_x and θ_y bins and give the dimensions of the count matrix N for the histogram used to generate $\mathbb{D}_0$ or $\mathbb{R}_b$ – that is, the matrix of counts N_0^{ij} of $\mathcal{X}_0$ entries (for D-maps) or N_b^{ij} of $\mathcal{X}_b$ entries (for R-maps) in each (θ_x, θ_y) bin. We then define $\Sigma \equiv \text{sum}(N)$ and $M \equiv \max(N)$ to be the total number and maximum number of counts observed amongst the bins. P refers to the proportion of data used in a map, compared to some reference dataset; using the function $|\cdot|$ on a dataset to refer to the number of data points (e.g., $|\mathcal{X}| = 10^7$ in this work), we define $P_0 \equiv |\mathcal{X}_0|/|\mathcal{X}|$ for D-maps and $P_b \equiv |\mathcal{X}_b|/|\mathcal{X}_0|$ for R-maps.

A.2 D-maps

A D-map is just a normalised two-dimensional histograms expressed as a heatmap, and can represent data by itself or in conjunction with a set of R-maps. Given some dataset $\mathcal{X}_0$ with features $(\theta_1, \theta_2, ..., \theta_F)$, we take a two-dimensional histogram of the data with respect to two chosen features θ_x and θ_y (the main features). We normalise the count matrix N_0 by the maximum number of counts $M_0 \equiv \max(N_0)$, both as described in Section A.1, giving us the normalised count matrix (or *density matrix*) $\mathcal{D}_0 \equiv N_0/M_0$. The D-map is then the heatmap (in the main feature plane) of $\mathcal{D}_0$, or alternatively $\log \mathcal{D}_0$ (taking the log element-wise); this work uses $\log \mathcal{D}_0$.

A.3 R-maps

R-maps show the representation of a subset of some dataset with respect the original dataset. They are not standalone plots; every R-map is defined with respect to some D-map. The motivation for R-maps comes from the following question: given some D-map (with main features θ_x and θ_y), if we consider some third feature of interest θ_z (the band feature) and partition its domain into bands – i.e., into disjoint connected intervals that cover the domain – how are the data in the different bands represented in the D-map? In other words, what are the trends in the D-map with respect to θ_z, from a representation perspective? One might plot a contour map of θ_z in the (θ_x, θ_y) plane to address the question of trends, however contour maps can be messy and difficult to analyse due to any number of reasons, including noise (e.g., if analysing real world data) or degenerate combinations of model parameters affecting the distribution of data features (e.g., if analysing random simulated data). R-maps help to alleviate this by replacing contours with colour maps that give a better qualitative picture of data trends, at the cost of reduced quantitative precision and a need for more plots (each band of θ_z yields a

separate R-map). Below we outline the process of generating an R-map, which will give us the foundation for an explicit definition.

Consider a D-map $\mathbb{D}_0$ of $\mathcal{X}_0$, with main features (θ_x, θ_y). We want to generate a set of R-maps for a band feature θ_z, whose values lie in the interval $\mathcal{I}_{\theta_z}$. An R-map $\mathbb{R}_b$ of $\mathbb{D}_0$ (with respect to θ_z) is generated as follows:

1. Isolate a subset $\mathcal{X}_b \subseteq \mathcal{X}_0$ of the data by restricting the θ_z values to lie in some subinterval $\mathcal{I}_b \subseteq \mathcal{I}_{\theta_z}$ ("band b").

2. Using the same binning scheme as $\mathbb{D}_0$, generate a (θ_x, θ_y)-histogram of $\mathcal{X}_b$ to get the count matrix N_b (the matrix of counts N_b^{ij} of $\mathcal{X}_b$ entries in each (θ_x, θ_y) bin)

3. Calculate the proportion of data in band b, $P_b \equiv |\mathcal{X}_b|/|\mathcal{X}_0|$ (recall, here we take $|\cdot|$ to mean the number of data points when applied to a dataset).

4. Using the count matrices N_b and N_0, calculate the *representation matrix* for band b, defined by:

$$\mathcal{R}_b \equiv \frac{N_b - P_b N_0}{N_b + P_b N_0}, \tag{A.1}$$

where the above division is element-wise division. The R-map of band b, $\mathbb{R}_b$, is the heatmap of $\mathcal{R}_b$ in the main feature plane. The elements $\mathcal{R}_b^{ij}$ range from -1 (no representation, when $N_b^{ij} = 0$) to $+1$ (infinite over-representation, in the limit $N_b^{ij}/P_b N_0^{ij} \to \infty$), except where $N_b^{ij} = N_0^{ij} = 0$, in which case $\mathcal{R}_b^{ij}$ is undefined and will need to be dealt with accordingly when coding (for example, by adding a very small $\epsilon > 0$ to the denominator). The basic qualitative implication of Equation (A.1) is that band b (i.e. the data in $\mathcal{X}_b$) is either under-represented ($\mathcal{R}_b^{ij} < 0$), equally represented ($\mathcal{R}_b^{ij} = 0$) or over-represented ($\mathcal{R}_b^{ij} > 0$) in a given (θ_x, θ_y) bin of the D-map.

In this work, R-map sets are produced by partitioning the θ_z domain $\mathcal{I}_{\theta_z}$ into connected bands of equal width (which we then use to create the band-filtered datasets $\mathcal{X}_b$ and their

R-maps). This is an easy, consistent method of generating R-maps and is good for first-pass analysis; in principle though, the subintervals $\mathcal{I}_b$ of step 1 above can be any subset of $\mathcal{I}_{\theta_z}$, whether disconnected or overlapping, and it is not necessary that the subsets partition or cover $\mathcal{I}_{\theta_z}$.

A.4 Toy Example

Here we consider a toy example where we have a model with three real-valued parameters a, b and c. We generate a dataset $\mathcal{X}$ containing 10^7 samples of (a, b, c) triplets, with a, b and c sampled uniformly on the intervals (3,4.5), (1,4) and (2,5) respectively.

Suppose we are interested in the relationship between one of the basic parameters, a, and a more complex quantity of interest derived from the parameters, $b^{c/b}c^{a/c}$. These will constitute our main features θ_x and θ_y respectively, for the purposes of generating a D-map. We give three examples of D&R map sets, each using the same binning scheme of 100 $\times$ 100 bins along the x- and y- axes. The D&R maps are shown in Figures A.1, A.2 and A.3, with the D-maps given in the top left panel and the R-maps in the others.

For the first two examples, Figures A.1 and A.2 show the D&R mappings of $\mathcal{X}_0 = \mathcal{X}$ with respect to main features $(a, b^{c/b}c^{a/c})$ and respective band features a and $b^{c/b}c^{a/c}$ (i.e. the band features are respectively the same as the x-axis and y-axis main features). In the first case the data is partitioned ($N_b = N_0$) into five bands of equal width along the x-axis, with the same degree of over-representation in each band of a due to a's uniformity: each band contains 20% of the data and occupies 100% of the bins in its band, i.e. $P_b = 0.2$ and giving the same value of $R_b = (1 - 0.2)/(1 + 0.2) = 2/3$ in each bin. In the second case the data is partitioned ($N_b = N_0$) into five bands of equal width along the y-axis, but the bands are now over-represented to different degrees because the distribution of the band parameter $b^{c/b}c^{a/c}$ is no longer uniform: we see different values for $P = P_b$ in the headers of the R-maps, but because the (θ_x, θ_y) main feature space is partitioned we

have $N_b = N_0$ like the first example, and thus bands which represent smaller subsets of $\mathcal{X}$ (lower P_b) accordingly have higher R_b values (are more over-represented).

In the third example we now apply a filter $\mathcal{X}_0 = \mathcal{X}(\texttt{a < 2b})$ to get rid of data points where $a \geqslant 2b$, and use a more complicated band parameter, $\ln(a^{abc}b^{3/a}c^{a/3})$. Figure A.3 shows the corresponding D&R mapping of $(\mathcal{X}(\texttt{a < 2b}) : a, b^{c/b}c^{a/c}, \ln(a^{abc}b^{3/a}c^{a/3}))$; we see that the filter has removed about 30% of the data ($P = 70.8\%$ in the D-map on the top left), and the bands $\mathcal{X}_b$ no longer partition the data in the main feature space (i.e. different bands overlap in the space).

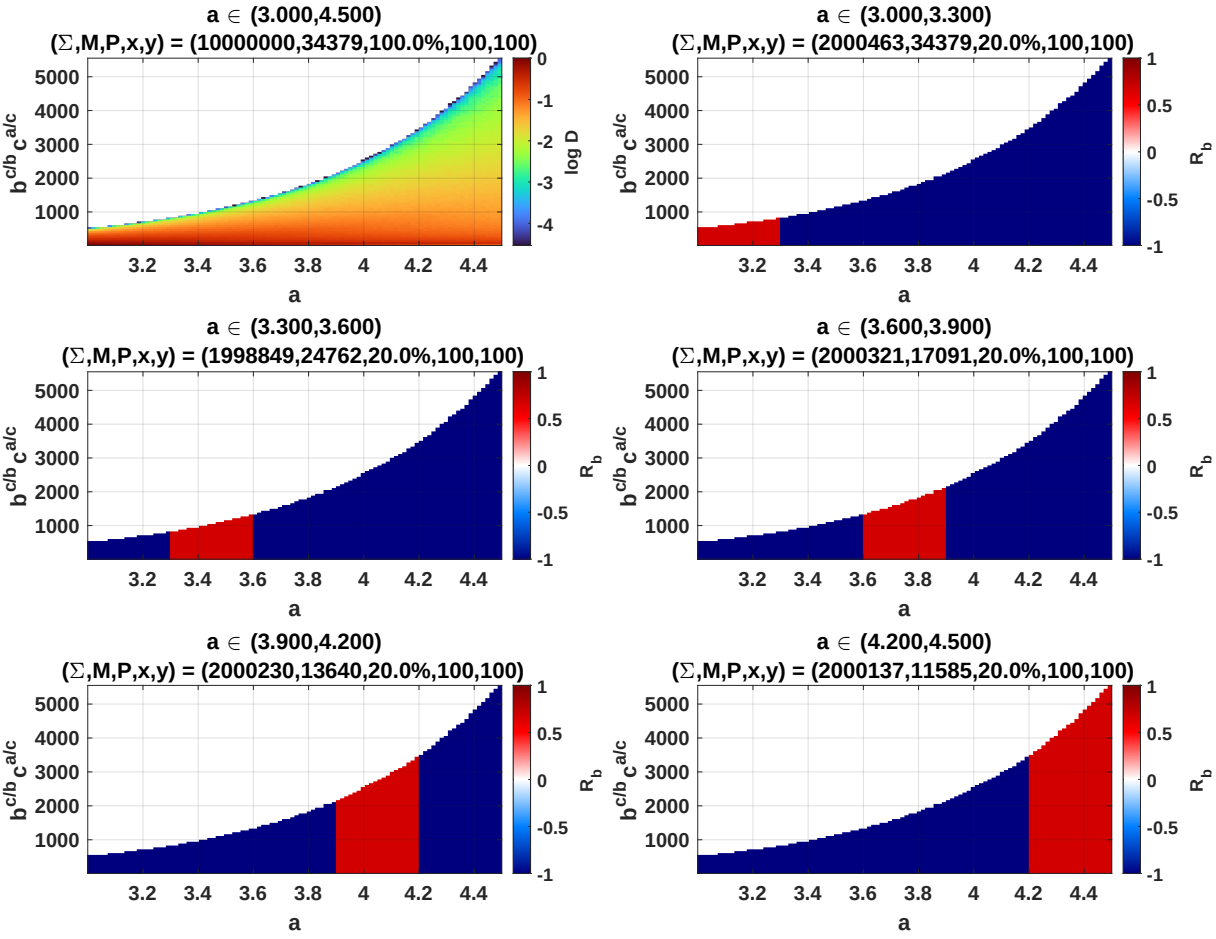

Figure A.1: A toy example showing a D&R Mapping of $(\mathcal{X} : a, b^{c/b}c^{a/c}, a)$; the band parameter is the same as the x-axis main feature (i.e., a), and thus we see the data being partitioned into five bands of equal width along the x-axis, with the representation shown for each band. Because a is uniformly sampled, each band contains 20% of the data (i.e., $P_b = 0.2$, shown as $P = 20\%$ in the headers of the R-maps) and is thus over-represented to the same degree in each bin (i.e., each bin is the same colour/has the same value of R_b).

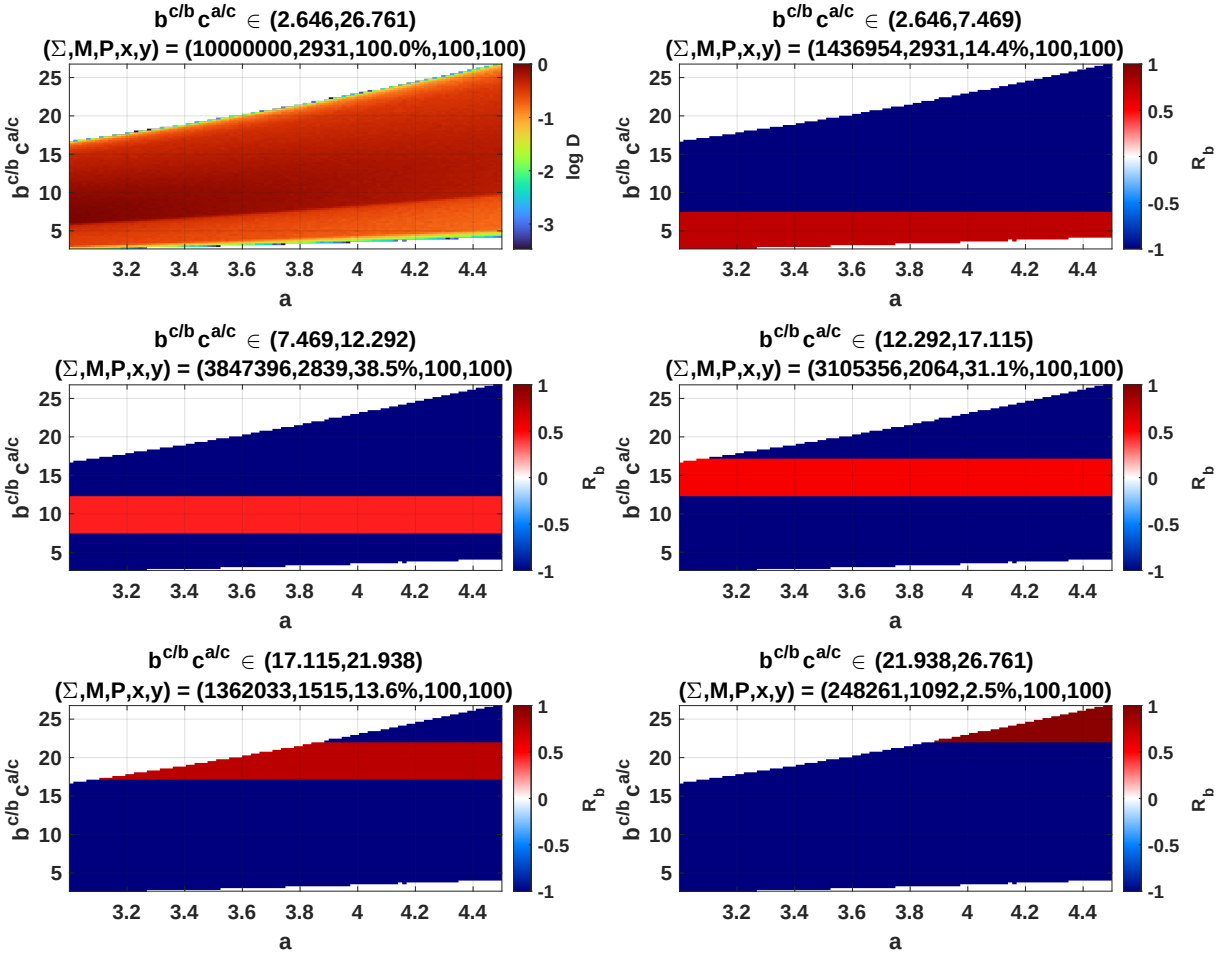

Figure A.2: A toy example showing a D&R Mapping of $(\mathcal{X} : a, b^{c/b}c^{a/c}, b^{c/b}c^{a/c})$; the band parameter is the same as the y-axis main feature (i.e., $b^{c/b}c^{a/c}$), and thus we see the data being partitioned into five bands of equal width along the y-axis, with the representation shown for each band. The band parameter $b^{c/b}c^{a/c}$ is not uniformly distributed across its bins and thus each band is over-represented to varying degrees, with bands containing lower proportions of the data of the data showing higher representation (i.e., lower P_b implies higher R_b).

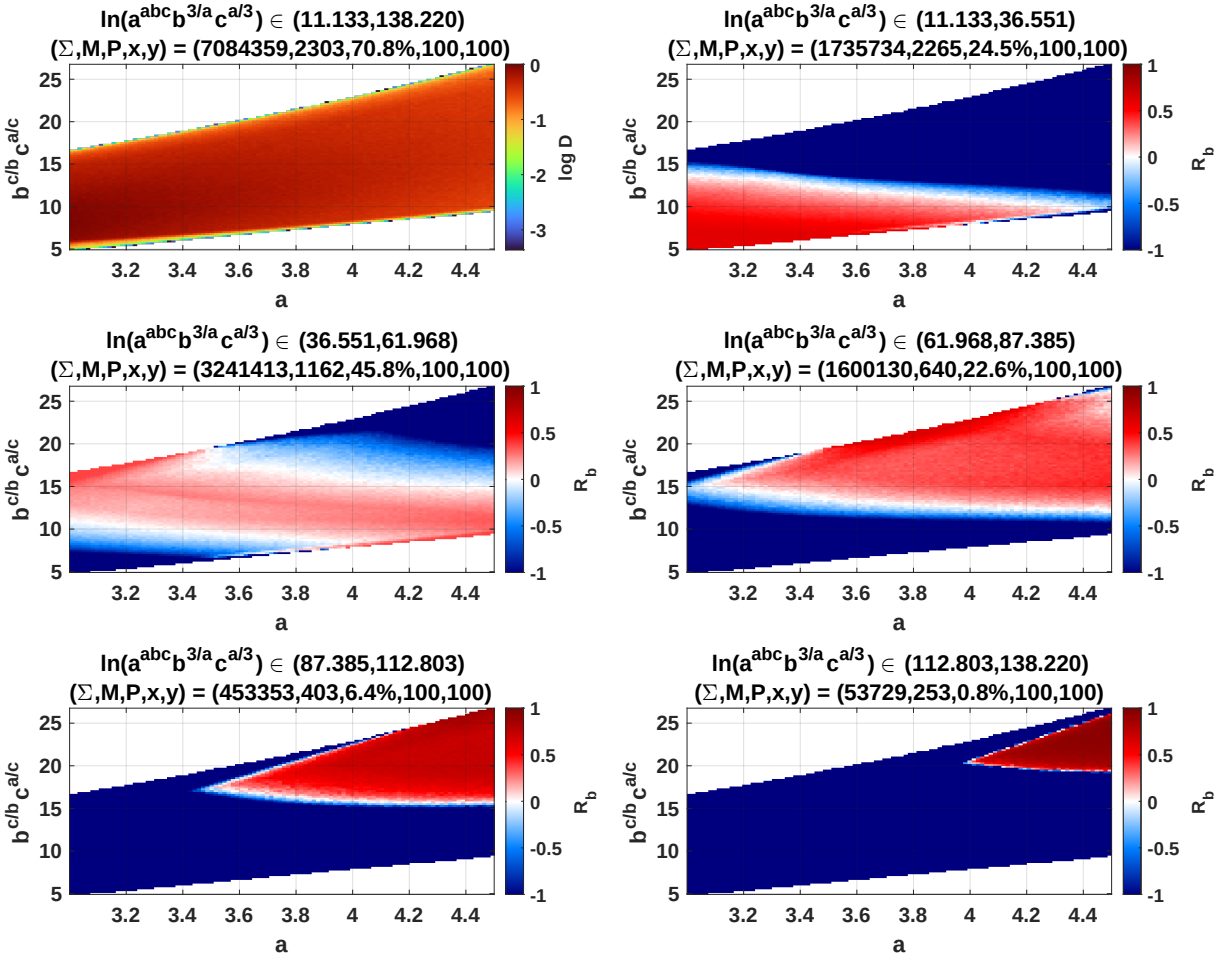

Figure A.3: A toy example showing a D&R mapping of $(\mathcal{X}(\texttt{a < 2b}) : a, b^{c/b}c^{a/c}, \ln(a^{abc}b^{3/a}c^{a/3}))$; unlike Figures A.1 and A.2, the bands of the band parameter $\ln(a^{abc}b^{3/a}c^{a/3})$ do not partition the data in the main feature space (i.e. there are overlapping bands), and we see areas where the bands are equally represented (white colour, corresponding to $R_b = 0$) and under-represented (blue colour with $-1 < R_b < 0$) with respect to the data in the D-map. The representation is calibrated to the filtered data, meaning that the P_b values shown in the R-maps represent the proportion of data compared to the $\Sigma = 7084359$ data points in $\mathcal{X}_0 = \mathcal{X}(\texttt{a < 2b})$, as opposed to the 10^7 data points in $\mathcal{X}$.

A.5 Summary and Remarks

In summary, D&R maps provide a way to visualise the trends in a dataset (represented as the D-map $\mathbb{D}_0$) with respect to some feature θ_z (the band feature), via the R-maps $\mathbb{R}_b$ of $\mathbb{D}_0$. An example of a D&R map set can be seen in Figure 2.2, which visualises Equation

(2.12).

Regarding the motivation for how the representation in Equation (A.1) is defined: if we assume proportional representation for a band $\mathcal{X}_b \subseteq \mathcal{X}_0$, then $P_b N_0$ is the expected value for the observed N_b. Thus the representation can be thought of as:

$$\mathcal{R}_b \equiv \frac{\text{observed counts} - \text{expected counts}}{\text{observed counts} + \text{expected counts}}. \tag{A.2}$$

This is similar to the relative deviation from the expected value, which would have only the expected value in the denominator and thus no upper limit. However, since $0 \leqslant N_b \leqslant N_0$, adding the observed value to the denominator constrains $\mathcal{R}_b \in [-1, +1)$, putting all R-maps on the same scale. This is well-suited to the qualitative model analysis in this work, as $\mathcal{R}_b$ behaves similarly to the relative deviation when $N_b \lesssim P_b N_0$ but is confined to a small range of values near $+1$ when $N_b \gg P_b N_0$.

Finally, we reiterate the care that must be taken when doing quantitative analysis with D&R mapping. The appearance of quantitative results can be misleading if one does not consider contextual factors when analysing R-maps, namely among them:

- The choice of band parameter θ_z and bands $\mathcal{I}_b \subseteq \mathcal{I}_{\theta_z}$ in relation to the distribution of the data with respect to θ_z; qualitatively speaking, how the data is binned matters, and in principle different binning schemes may yield very different sets of R-maps (i.e. count matrices N_b and data proportions P_b), based on the width and location of the bins.

- How disjoint the band-filtered datasets $\mathcal{X}_b$ are with respect to the D-map, i.e. how much the different $\mathcal{X}_b$ tend to share a common set of bins in the D-map; if the datasets are fully pairwise-disjoint, then $N_b = N_0$ where the data are represented (i.e. where $\mathcal{R}_b > -1$), meaning low $P_b \rightarrow$ high $\mathcal{R}_b$.

- How "concentrated" the $\mathcal{X}_b$ are in the D-map in relation to their proportion of data

P_b; that is, considering P_b, what percentage of the (non-empty) D-map bins are populated by $\mathcal{X}_b$? A highly-concentrated $\mathcal{X}_b$ with low P_b may have higher representation values and appear more significant than a less-concentrated $\mathcal{X}$ with high P_b.